Investigations of Polyethylene Materials by Means of X-ray Diffraction

Artificial Ageing of Polyethylene Gas Pipes

Dissertation

zur Erlangung des Doktorgrades der Naturwissenschaften
der Fakultät Physik der Technischen Universität Dortmund

vorgelegt von

Saskia Schmacke

November 2010

Contents

1. Introduction **1**

2. Polyethylene **3**

2.1. Polymers 5

2.1.1. Polymers in daily life 5

2.1.2. Architecture of Polymers 6

2.2. Polyethylene 9

2.2.1. Low density polyethylene 13

2.2.2. High density polyethylene 14

2.2.3. Molecular structure of polyethylene 15

2.2.4. Superstructure of polyethylene 17

2.3. Production of gas pipes 19

2.3.1. Extrusion – Basic principles 19

2.3.2. Plastics extrusion 20

2.4. Natural ageing of polyethylene materials 21

3. Theory **23**

3.1. Solid state order 24

3.1.1. Crystalline Solids 24

3.1.2. Polycrystalline structures 27

3.1.3. The amorphous state 28

3.1.4. Two-phase layer system 28

3.2. Theory of x-ray scattering 29

3.2.1. Scattering from a single scattering centre 29

3.2.2. Differential cross-section 30

3.2.3. The scattering function of a crystal lattice 31
3.2.4. Powder diffraction 34
3.2.5. Scattering from amorphous material 35
3.3. The diffraction signal of semicrystalline polyethylene 36
3.4. Small angle x-ray scattering at mesoscopic structures 38
3.4.1. Theory of Small Angle X-Ray Scattering 39
3.4.2. Application for semicrystalline two-phase layer systems 42

4. Experimental section **47**
4.1. Samples 47
4.1.1. Polyethylene gas pipes 47
4.1.2. Simulation of long term stability of polyethylene gas pipes . . . 48
4.1.3. Pipe samples provided by RWE 50
4.1.4. Sample preparation 52
4.2. Experimental setup 53
4.2.1. Beamline BL9 at DELTA: Small and wide angle x-ray scattering 53
4.2.2. The experimental station BW5 at Hasylab/DESY: Diffraction experiments 57
4.2.3. Sample cell for in-situ temperature dependent experiments . . . 57
4.2.4. Temperature calibration 59
4.2.5. Laboratory x-ray source at the University of Helsinki, Finland: space dependent SAXS experiments 60

5. Results **63**
5.1. X-ray diffraction measurements 63
5.1.1. Qualitative analysis of diffraction data 63
5.1.2. Quantitative analysis of diffraction data 68
5.1.3. Results of position dependent XRD experiments 72
5.1.4. Conclusions 80
5.2. X-ray diffraction studies of annealed polyethylenes 85
5.2.1. In-situ annealing experiments 85
5.2.2. Ex-situ annealing experiments 97

5.2.3. Summary and comparison between ex-situ and in-situ annealing experiments . . . 98
5.3. Analysis of small angle scattering data . . . 100
5.3.1. Summary of the results obtained in SAXS experiments . . . 104
5.4. Comparison of complementary scattering data . . . 106

6. Summary and outlook **109**

A. Appendix A **113**
A.1. Three-dimensional imaging of PE samples – Tomography experiments . 113
A.1.1. Introduction . . . 113
A.1.2. Basic principles . . . 114
A.1.3. Experimental setup at the computer tomograph at Helsinki . . . 115
A.1.4. Sample preparation and data acquisition . . . 116
A.1.5. Results . . . 117
A.1.6. Conclusion . . . 119

Bibliography **121**

Danksagung **I**

Eidesstattliche Erklärung **V**

List of Figures

2.1. Simplified representation of different polymer architectures. 7
2.2. (a) Steric image of a polyethylene monomer. (b) Polyethylene backbone chain. 9
2.3. Simplified representation of polyethylene architectures 14
2.4. (Non-primitive)PE unit cells from different point of views. 16
2.5. Development from an individual lamellar crystallite [13] to a fibre with alternating crystalline and amorphous layers and to a fibril (fibre bundle) [66]. 17
2.6. (a) Schematic representation of a spherulite structure [79]. (b) Spherulite structure of PE, optical micrograph [89].. 18
2.7. (a) Schematic image of a shish-kebab structure as proposed by Hosemann, i.e. fibril encapsulated with spherulites [67]. (b) TEM image of a shish-kebab superstructure of PE [45]. 18
2.8. Schematic image of an extrusion apparatus. 19

3.1. Deduction of the crystal structure. 25
3.2. Bravais lattices [1]. 26
3.3. Crystalline structures. 27
3.4. Schematic image of a two-phase layer system. 28
3.5. Transmission scattering geometry. A monochromatic x-ray beam with wavelength λ and wavevector $\vec{k}_i$ hits the sample. 29
3.6. Replacement of the position vector $\vec{r}_j\,'$ by the sum of the lattice vector $\vec{R}_n$ and the unit cell position vector $\vec{r}_j$, as defined in sec. 3.1.1. 31
3.7. Bragg scattering at a set of parallel lattice planes. 32

3.8. Two-dimensional scattering patterns of different structures. 35
3.9. Exemplary isotropic powder pattern of semicrystalline PE. 37
3.10. Schematic representation of two-phase layer systems in a lamellar arrangement. 43
3.11. Density distribution of an ideal two-phase layer system and the corresponding correlation function $K(z)$. Burrowed from [82]. 45
3.12. Density distribution of a two-phase layer system with fluctuating intercrystalline spacings and the corresponding correlation function $K(z)$. Burrowed from [82]. 46
3.13. Density distribution of a two-phase layer system with fluctuating intercrystalline spacings and varying crystalline thicknesses and the corresponding correlation function $K(z)$. Burrowed from [82]. 46

4.1. Schematic image of the creeping test apparatus. 49
4.2. Sample preparation. 52
4.3. Schematic overview of beamline BL9 of DELTA. 54
4.4. Pictures of the SAXS cell. 55
4.5. Picture of the heating cell. 58
4.6. Relationship between heater and sample temperature. 59
4.7. SAXS sample holder and setup at the laboratory x-ray source in Helsinki. 60

5.1. (a) Exemplary two-dimensional diffraction pattern for a surface slice of PE. Some diffraction rings show arcs of higher intensity and areas with lower intensity. This phenomenon is called texture. (b) Schematic representation of partially oriented PE crystallites in a polycrystalline sample. 63
5.3. Integration masks for the pie integrations and texture comparison for a native surface slice. 65
5.4. 2D and 1D diffraction patterns for a native pipe sample. 66
5.5. 2D and 1D diffraction patterns for an aged pipe sample. 67

5.6. One-dimensional diffraction pattern of a polyethylene sample with decomposition in amorphous and crystalline contributions as discussed in [72]. 69
5.7. Background correction and profile fit for XRD data. 70
5.8. Individual and averaged crystallinities χ and crystallite sizes L_{hkl} determined by x-ray diffraction for the native pipe R3. 72
5.9. Individual and averaged crystallinities χ and crystallite sizes L_{hkl} determined by x-ray diffraction for the aged pipe R2. 73
5.10. Comparison between crystallinities obtained for the native sample R3 and the aged sample R2. 74
5.11. Averaged crystallinity and crystallite size of sample r2. 75
5.12. Averaged crystallinity and crystallite size of sample r4. 76
5.13. Averaged crystallinity and crystallite size of sample r7. 77
5.14. Averaged and individual crystallinities χ and crystallite sizes L_{hkl} for the pipe samples r3, r5, r6, r8, r9, and r11. 78
5.15. Crystallinities χ and crystallite sizes L_{hkl} for the pipe sample r10 . . . 79
5.16. Comparison of individual and averaged crystallinities χ for street and pavement pipes. 80
5.17. Schematic representation of lamellar crystal growth in a cooling melt. From [64]. 81
5.18. Interpolated relation between tensile modulus E_t and crystallinity α. From [22]. 83
5.19. Views from inside and outside of a cracked pipe sample after internal pressure test. By courtesy of RWE. 84
5.20. Temperature progression of one-dimensional scattering patterns of an inner surface slice (sample R3E4). 85
5.21. Temperature dependent (a) peak positions q_{110}, (b) q_{200}, (c) lattice constant a and (c) lattice constant b for the sample cuboid R3D. 87
5.22. Temperature dependence of the lattice constants a and b as found by Swan [83]. 88
5.23. Temperature dependent crystallinities for the sample cuboid R3D. . . . 89

5.24. Temperature dependent crystallinities for the sample cuboid R3E. . . . 90
5.25. Temperature dependent crystallinity as found by Ueno *et al.* [88]. . . . 91
5.26. Temperature dependent crystallite size L_{200} for the sample cuboid R3D. 92
5.27. Temperature dependent crystallite size L_{200} for the sample cuboid R3E. The dotted lines are guide lines for the eye. (a) Outer surface, (b) first and (c) second bulk and (d) inner surface slice. 93
5.28. Temperature dependent lattice constant differences for the calculation of linear thermal expansion coefficients. 94
5.29. Temperature dependent ratio of peak heights deduced from 0- and 3-9-o'clock-direction for the sample cuboid R3E for the [110] and [200] reflection. The dotted lines are guide lines for the eye. 96
5.30. Temperature dependent crystallinities χ for the native pipe R3. Ex situ annealing. 97
5.31. Temperature behaviour of some polymers. Burrowed from [37]. 98
5.32. 2D SAXS pattern of native sample slices. 100
5.33. (a) Integrations in the horizontal and vertical plane of the scattering pattern in an I vs. q and Iq^2 vs. q representation. (b) Representation of the 2D pattern for low q values. 101
5.34. (a) Exemplary background corrected one-dimensional SAXS pattern for a native sample slice, measured at DELTA. (b) Same data as in (a), but as $I \cdot q^2$-plot for better visualisation. 102
5.35. Exemplary background corrected data set and corresponding correlation function. 103
5.36. Comparison of crystallinities and crystallite sizes determined by x-ray diffraction, SAXS at DELTA and in Helsinki for the native pipe R3 and the aged pipe R2. 106

A.1. Three component system for x-ray computer tomography. 114
A.2. Tomography setup. 116
A.3. Reconstructed tomography images of a PE sample with macroscopic crack. 117
A.4. Three component system for x-ray computer tomography. 118

List of Tables

2.1. Properties of the LDPE and HDPE [37]. 13
2.2. Fractional coordinates of the atoms in the asymmetric unit of PE in terms of the lattice constants a, b, and c. 15

3.1. List of possible diffraction peaks ($E = 27\,\mathrm{keV}$), calculated from the lattice positions presented in tab. 2.2 and applying space group $Pnam$ in the scattering angle range between 0 and 16 °. 37

4.1. Examined samples with information about dimensions, ageing conditions (pressure, temperature and time to withstand), working place and manufacturing date. Information was provided by *RWE Westfalen-Weser-Ems Netzservice GmbH*. 51

5.1. Exemplary parameters for the integration of two-dimensional scattering data of sample R3D1. 69
5.2. Averaged values for crystallinity, full width half maxima and corresponding crystallite sizes of sample R3D1. 71
5.3. Crystallite melting temperatures T_{CMT}. 90
5.4. Linear thermal expansion coefficients α_a for the sample cuboids R3D and R3E. 95
5.5. Estimated values for correlation peaks and corresponding layer thicknesses. 102
5.6. Layer thicknesses and crystallinity deduced from correlation function calculation for sample slice R3D1. 104

1. Introduction

Gas pipes made of high density polyethylene (HDPE) have been in use by gas suppliers for more than 35 years [38]. The material offers many favourable properties, like high rigidity and resistance against chemicals, pressure and radiation, making it ideal for industrial applications. However, as the material ages, it becomes brittle and prone to breakage, making it necessary to replace pipes after a certain amount of time.

To slow the ageing process, a broad selection of additives like plasticisers, UV stabilisers and anti-oxidants is introduced into the material. The application of these techniques leads to a predicted lifetime of HDPE pipes currently in use of about 50 years [78]. The premature repair or substitution of a pipe is costly, that is why several techniques are used to estimate the remaining lifetime of gas pipes. Furthermore it is crucial to understand the ageing process of the material in order to minimise the probability of material failure during the time a pipe is in use. This is especially important since contact with different chemicals, temperature fluctuations and pressure causes faster ageing processes.

Up to now, the usual way to examine the condition of the material has been by measurement of material constants like Young's modulus or oxidative-induction times. While these do yield information on the probability of future material failure, this information is restricted to macroscopic length scales. Furthermore, the tests are time-consuming and costly. However, most of the key macroscopic properties of the HDPE material can be linked to one microscopic property: its crystallinity.

A new pipe of HDPE shows a certain degree of crystallinity. As the material ages, the crystallinity increases, making it a convenient indicator for the ageing process. Since the fraction of crystalline domains in the material is accessible by means of x-ray scattering

measurements, this opens up a whole new way of observing the different processes that comprise the macroscopic ageing of HDPE pipes.

X-ray diffraction and small angle x-ray scattering are suitable tools to examine the sample structure on nanometre scales. This thesis presents results on how both techniques have been successfully applied in order to determine the crystallinity of slices cut out of the pipe walls. The results of natively and artificially aged pipe samples are compared. Ageing is induced by internal pressure creeping tests, that are conducted in order to simulate the ageing behaviour of gas pipes (see section 4.1.2). Additionally, the relative orientation of PE chains within the material and thus the texture of the crystalline domains with respect to each other have been investigated.

The thesis is structured as follows: After a short introduction of polymers regarding architecture and applications, the polymer polyethylene concerning structure and properties will be discussed in detail in chapter 2, including also the manufacturing of PE gas pipes and natural ageing processes. The following theory chapter 3 deals after a short introduction with the semicrystalline structure of solid bodies and is focused on the crystalline state and its mathematical description. Afterwards, a brief introduction into the theory of x-ray scattering is given, followed by a detailed theoretical consideration of the scattering techniques used in this work.

In the experimental section 4 a detailed description of the investigated samples and the artificial ageing induced by internal pressure creeping tests is given. This section is completed by an overview of the experimental setups used for the experiments.

In chapter 5 the results of position and temperature dependent XRD experiments will be presented and discussed. After a short presentation of results gained in SAXS experiments, the thesis is closed by a summary and an outlook in chapter 6.

2. Polyethylene

Polyethylene (PE) materials can be applied in many fields of life. Which type of PE has to be used depends on the demands to the material grade and thus on the particular properties of the PE type. PE materials are utilised in many different configurations, resulting in varying degrees of crystallinity and the related macroscopic properties like elasticity, brittleness and melting points.

Two important classes of PE materials are high density polyethylene (HDPE) and PE with low density (LDPE). LDPE is characterised by a relatively low rigidity. Therefore it can be used as packaging material, e.g. foil, and as cover sheeting in many fields of daily and industrial life. Used in multilayer foils, LDPE serves as steam barrier. Another application is the utilisation as cable insulation and as coating for pipes.

HDPE is marked by a higher crystallinity and therefore rigidity. It is utilised as building material and for components in the automobile industry. Different kinds of household articles like cups, colanders, buckets, etc. are made of HDPE. Polyethylene can be also found in beverage bottles, as container for chemicals and as constituent of adornment.

A very important utilisation of PE of high density is the application as material for gas pipes. This is the reason for the cooperation between industry and university that caused this work.

40 years ago the main material grades utilised in gas supply were so-called PE63 pipes. The name results from the technical requirement to withstand a 6.3 N/m^2 pressure over a certain amount of time in creeping tests after a lifetime of 50 years[1]. Younger materials, and especially pipes produced nowadays, have to bear substantially higher

[1]The specifications refer to values for water. In so-called creeping tests (see section 4.1.2) a pipe is exposed to a water bath with a temperature of 80 °C. After capping of both open ends the requested pressure is applied. The time until burst is then determined.

pressures. Current and further developed material grades used for gas supply are PE80 and PE100. For these materials the creeping tests demand a resistance against pressures of 8.0 and 10.0 N/m^2, respectively.

PE materials possess a wide range of advantageous properties, which are described in section 2.2. The scope of this work deals with the examination of gas pipes, utilised by *RWE*, at many different spots with varying environmental parameters that will be discussed later in section 4.1. Hundreds of kilometres of gas pipes have been installed in the late 70ies. With a predicted lifetime of 50 years these pipes reach a critical age concerning their expected lifetime, so that the risk of material failure increases.

Polyethylene is a polymeric macromolecule. The following section deals with polymers, their application in daily life and their architecture in general. Afterwards, the general structure of PE, material properties, the two classes PE of low and high density and structural hierarchies will be discussed. This section is followed by a description of the manufacturing process of PE pipes and ageing processes, from which the pipes suffer.

2.1. Polymers

2.1.1. Polymers in daily life

Polymers are omnipresent in daily life. Essential biological processes are determined by polymers like DNA (Desoxyribo Nucleic Acid), RNA (Ribo Nucleic Acid) and proteins, which catalyse certain chemical reactions. Cellulose is a polymer and starch as well.

But polymers can also be found in other materials. They can be used for packaging materials and beverage bottles. Propylene glycol, glycerol and others are polymers which are found in cosmetics and drugs. They are versatilely used in everyday life and find use as commodity polymers for widespread applications or as speciality polymers for specific utilisations:

- Thermoplast: High temperatures during the fabrication enable almost free choice in the shape of the products, but they possess the following disadvantage: thermoplasts offer a limited temperature range in which these materials can be used. Other materials like ceramics and metals, which are fabricated in a more complicated production process, are much more resistant against elevated temperatures.

- Polymer fibres: They are the main component of textiles and woven products. Fibres are fabricated in spinning processes from the polymer melt or concentrated solutions at high temperatures [61]. High temperature causes the shrinkage of the material. Thus, fibres can only be used in a limited temperature range.

- Elastomers: Synthetic and natural rubbers belong to this class of polymers. The main step in the production of elastomers consists in a cross-linking process briefly described in subsection 2.1.2. In natural rubbers the cross-linking is initialised by the so-called vulcanisation process [14], which involves the heating of cis-polyisoprene in the presence of sulfur, leading to cross-links between the polyisoprene chains.

- Duromers or thermosets, respectively: Duromers are also called resins and are elastomers with a high cross-linking density which leads to a loss of deformability. Adhesives are representatives of this class of polymers, which are in general rather stable.

The large variability in the composition and architecture of polymeric macromolecules offers the opportunity for the production of material grades with a vast number of dedicated features. In particular, thermomechanical processes during the polymerisation of macromolecules have a vital influence on the final formation of the polymer structure, as will be discussed in sec. 5.1.4.

The focus of this work lies in the investigation of a certain polymer: polyethylene. Thus, after the introduction of polymer architectures in general, the subsequent sections will focus on the structure of polyethylene, different types of polyethylene, the production of gas pipes and ageing processes.

2.1.2. Architecture of Polymers

Polymers are macromolecules, consisting of many molecular units called monomers, linked by covalent bonds. The number N of molecular units determines the degree of polymerisation.

Polymers are produced in a polymerisation process starting from reactive low-mass compounds, resulting in macromolecules with a C–C backbone chain. Some polymers like polyethylene (PE) and polycarbonate offer a flexible backbone chain, while polyimide is an example for a polymer with a stiff backbone. Another type of polymer consists of a backbone chain based on silicon atoms instead of carbon atoms. A representative of this class of polymers is poly(dimethylsiloxan) [82]. If the macromolecule consists of monomers with ionisable groups, the resulting polymer chain is called polyelectrolyte. Cellulose and starch, two important natural polymers, belong to this class of macromolecules.

But polymers can not only exist as large chains. Different types of architecture are possible, which are shown in fig. 2.1 in a simplified representation and are discussed in the following:

- Some polymers show a certain degree of branching: short- and long-chain branches are statistically distributed over the length of the backbone chain. The so-called branching ratio (fraction of the branched units) is in the order of several percent. The branching ratio strongly influences the density of the material and thus the properties of the solid body. LDPE consists of branched polymer chains.

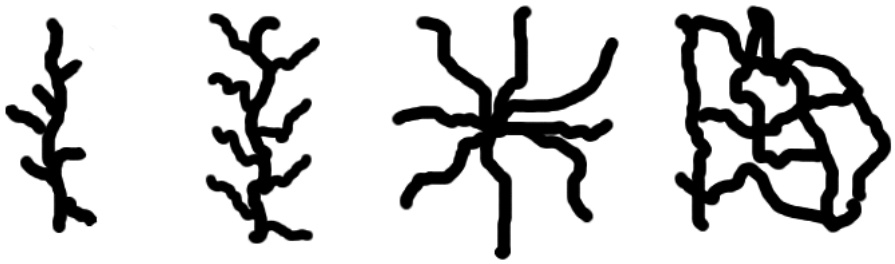

Fig. 2.1.: Simplified representation of polymer different architectures. (a) Polymer chain with a certain degree of branching. (b) Grafted-chain polymers. Considerably longer branching chains than in case (a). (c) Star polymer. Several polymer chains are linked in one multi-functional centre. (d) Network of cross-linked polymer chains.

- Longer branching units consisting of deviating oligomer chains belong to so-called grafted-chain polymers. Starch is a prominent example for a grafted-chain polymer [85].

- If several polymer chains are linked in one common multifunctional centre, a star polymer is built. Poly(ethylene oxide) is an example for the class of star polymers [68].

- The coupling of the polymer chains leads to a three-dimensional network, which is the basic structure of rubbers [14]. The cross-linkage leads to a qualitative change in the properties which are strongly influenced by the degree of networking – the so-called cross-link density [14].

.

In general a polymerisation process yields not only one species of macromolecules, but a molar mass distribution with a certain average mass is present. The average molar mass $\overline{M}_n$ of a polymer consisting of n monomers is defined as

$$\overline{M}_n = \int_0^\infty p(M) M dM$$

whereas the distribution function $p(M)$ is the number density of masses M. There are strong differences in the molar mass distributions between different polymeric compounds. Two different classes of polymerisation processes exist:

- Step polymerisation: In this polymerisation process groups of already linked monomers can react with other groups. This results in broad distribution functions, often represented by a so-called Schulz-Zimm distribution [82]. Polymers like polyesters and polyamides result from step polymerisation processes.

- Chain polymerisation: There are reactive centres, coupling only with single monomers. After the reaction, these reactive centres are transferred to the end of the chain. This kind of polymerisation process leads to an extremely narrow mass distribution, which can be described by a Poisson distribution. Polyethylene originates from a chain polymerisation process.

The shape of the distribution function $p(M)$ strongly influences the properties of the polymer. Variations of the polymers mass distribution can improve the materials properties and are therefore of considerable technical importance.

2.2. Polyethylene

Polyethylene (PE) belongs to the group of polyolefins. These kinds of polymers are built-on olefines (C_nH_{2n}), for example not-saturated acyclic or cyclic aliphatic hydrocarbones [37]. Examples for monomeric constituents of polyolefines are propylene, buten-1 and isobutene.

As all polyolefines, PE is a semicrystalline thermoplastic and often used as main component of gas pipes. It is produced by the polymerisation of ethene ($CH_2 = CH_2$) to a long chain molecule (see fig. 2.2(b)). The monomeric unit is depicted in fig. 2.2(a).

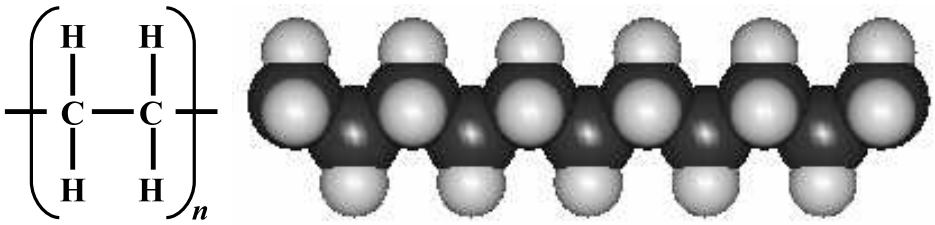

(a) (b)

Fig. 2.2.: (a) Steric image of a polyethylene monomer. (b) Polyethylene backbone chain.

The mechanical and physical properties of such a semicrystalline material are strongly influenced by e.g. the degree of molecular chain branching or the averaged molecular mass. The degree of crystallinity and thus also the density are influenced by the branching ratio. The latter is effected by the synthesis conditions during the production process. In the case of a large crystallinity, there are few branched, densely packed chains and thus the material exhibits a large density. A higher branching ratio consequently results in lower crystallinity and density.

Mechanical properties like rigidity, tensile strength and hardness are directly influenced by the material's crystallinity. A higher crystallinity causes a higher stiffness, tensile strength and hardness. The chemical resistance e.g. against acids and alkaline solutions, an outstanding property of PE materials, is also increased by a higher crystallinity. But a high crystallinity is not only advantageous, but can also have negative effects on these materials. They are characterised by a lower impact strength [2], a smaller transparency and a decreased tensile crack resistance. However, a relatively low permeability for

[2] corresponding experiments have been performed and presented in [22]

water vapour and gases is of course desired for gas pipes, since only small losses due to leaking pipes can be accepted. Due to the reduced resistance of highly crystalline PE materials against impact, the ratio of amorphous and crystalline fractions in the material has to be optimised to guarantee an outstanding materials grade.

PE is often used as electrical insulator. It is characterised by its good resistance against almost all polar solvents (at temperatures below 60 °C), acids, alkaline solutions, water and alcohols. A low resistance against oxygen, heat and UV radiation are disadvantages of the material. Due to softening at temperatures above 80 °C [37] it can only be used in a limited temperature range. The temperature resistance strongly depends on the crystallinity. The lower the crystallinity, the lower the heat resistance. PE embrittles when it is exposed to strong solar radiation. Carbon black can provide protection in this case. Also cross-linking of PE macromolecules causes a higher thermal resistance. In that case the material is denominated as PE-X. For industrial applications the following properties offer advantages: PE solids exhibit a large deformability and therefore it is possible to bring PE to almost every desired shape. In addition, PE burns without residues to CO_2 and H_2. It shows a good sliding behaviour, little abrasion at normal working conditions and has an unpolar and hydrophobic surface.

Another important property is its elasticity. It is basically determined by the amount of amorphous domains, since the elasticity of these domains is many times higher than the elasticity of crystalline areas. A material grade is characterised by several macroscopic properties. In the following, a brief overview over some properties should be given.

Crystallinity

The samples crystallinity χ can be defined in many different ways. In general, the crystalline fraction of a semicrystalline material is meant. This fraction can be determined by different experimental techniques. Two commonly used definitions are the volume and mass crystallinity of a semicrystalline sample. The crystallinity can be deduced for example from the crystalline contribution to the scattering signal in an x-ray diffraction or small angle x-ray scattering experiment. Thus, for the crystallinity χ of a semicrystalline material follows with generalised quantities am und cr:

$$\chi = \frac{cr}{am + cr}. \tag{2.1}$$

cr and am can be replaced by any crystalline and amorphous fraction, *eg.* volume or mass.

Linear thermal expansion coefficient

The extension of a material is a function of the surrounding temperature. With rising temperature, each direction usually suffers a length variation $\frac{\Delta L}{L_0}$. In general, $\frac{\Delta L}{L_0}$ can be defined as

$$\frac{\Delta L}{L_0} = \alpha(T - T_0) + \beta(T - T_0)^2 + \dots. \tag{2.2}$$

T_0 and L_0 are the reference temperature and corresponding reference extension. α and β are the materials linear coefficients of thermal expansion. β can often be set to zero in practical circumstances, since $\frac{\Delta L}{L_0}$ often shows an almost linear behaviour in easily accessible temperature ranges. Regarding to thermal ageing, amorphous and crystalline materials differ in their expansion coefficients. Amorphous materials show up to 100 times larger expansion coefficients than crystalline materials. That is the reason for strain between both domains in the case of elevated temperatures in polycrystalline materials, resulting in damage and material failure by thermal fatigue.

Elasticity and Young's modulus

The elasticity of a solid body is a basic mechanical property. The deformation of a material depends on the elasticity and is up to a certain degree reversible. The tension σ of the deformation is a function of the elongation ε, as described by Hooke's law

$$\sigma = E \cdot \varepsilon, \tag{2.3}$$

with the constant of proportionality Young's modulus E (unit $\mathrm{N/m^2}$), also called tensile modulus, which is anisotropic [55]. A higher elasticity manifests itself in a lower Young's modulus. Consequently, as highly crystalline materials are characterised by a high Young's modulus, they are thus more rigid.

Not only the linear expansion coefficient, but also the tensile moduli differ considerably between amorphous and crystalline fractions. Different values for the elongation at which the material fails can be observed for both fractions [37]. Concerning amorphous plastics and especially rubbers this maximum elongation can amount to 1000 % of its original length. Increasing temperatures result in deviating extensions and thus strains between both regions. Amorphous domains with large maximum elongation and high elasticity neighbour crystalline areas with only low resistance against external forces due to their low elasticity. When loads are applied in directions of lower elasticity, the material can fail due to the anisotropic tensile modulus. Since PE is a polycrystalline material, the elasticity is also relevant in the scope of this work.

Property	LDPE	HDPE
density [g/cm^3]	0.915 – 0.935	0.942 – 0.965
degree of crystallinity [%]	40 – 50	60 – 80
Young's modulus (23 °C) [N/mm^2]	200	1000
tensile strength [MPa]	8 – 15	20 – 30
ultimate elongation [%]	600	400 – 800
modulus of shear [GPa]	0.1 – 0.2	0.7 – 1.0
bending strength [MPa]	10	35
thermal expansion coefficient [1/K]	$1.7 \cdot 10^{-4}$	$2.0 \cdot 10^{-4}$
melting temperature [°C]	105 – 110	130 – 135

Tab. 2.1.: Properties of the LDPE and HDPE [37].

Two important classes of PE materials are high density polyethylene (HDPE) and PE with low density (LDPE). The two types are characterised in the next sections, whereas important material properties are summarised in tabular 2.1.

2.2.1. Low density polyethylene

The first successful production of a PE of low density took place in 1933 by ICI [37]. In 1939 and 1941 the industrial fabrication started in England by DuPont and Union Carbide [37]. The synthesis of LDPE is either performed in a high pressure or in a high temperature process at pressures between 1000 and 2000 bar or at elevated temperatures between 100 and 300 °C, respectively.

Some material properties are summarised in table 2.1 and the general structure of a LDPE chain is depicted in figure 2.3(a).

LDPE exhibits a density between 0.915 and 0.933 g/cm^3 due to a high branching ratio. Only 40–50 % of the solid body of LDPE are crystalline, the remaining fraction is amorphous or located in transient areas. LDPE is component of foils for wrapping, shrink foils or agricultural foils. It is also used as cable insulator, for the coating of pipes or as container for chemicals.

LDPE materials are characterised by a relatively low tensile strength of 8–15 MPa, but exhibit a high maximum elongation of ∼600 %. Due to its low crystallinity, the melting temperature is rather small with 105 − 110 °C. The thermal expansion coefficient of

LDPE amounts to $1.7 \cdot 10^{-4}\,1/\mathrm{K}$. The material is rather elastic due to its low Young's modulus of $200\,\mathrm{N/mm^2}$.

(a) (b)

Fig. 2.3.: Simplified representation of polyethylene architectures: (a) LDPE chain with a certain degree of branching. (b) HDPE chain with an almost unbranched polymer chain.

2.2.2. High density polyethylene

A low pressure fabrication process results in polyethylene of high density. Here temperatures between 20 and 150 °C and pressures of 1–50 bar are used with special catalysts. There are two main manufacturing paths: the Ziegler-Natter process is based on the application of titan and aluminiumalcyl catalysts [94], while in the Philipps process chromoxide catalysts are used. Due to the synthesis conditions, PE chains with low branching degree and mostly linear shape arise. Only three to five branches occur in a chain of 1000 carbons. This results in a high density of $0.942 - 0.965\,\mathrm{g/cm^3}$ and a crystallinity of $60 - 80\,\%$.

The tensile strength of HDPE amounts to 20 – 30 MPa. It is thus significantly higher than the one of LDPE, while the maximum elongation is of the same order of magnitude ($400 - 800\,\%$). The high crystallinity causes a high melting temperature of $130 - 135$ °C, which results in a considerably high thermal resistance.

Injection moulding is the main manipulation process for HDPE and products manufactured using this technique are household articles like plastic mugs and bins as well as

stock and transportation containers like bottle crates or fuel tanks. Pipes for drinkable water and sewage as well as gas pipes are also made of HDPE. Its low permeability for water and gas makes HDPE eminently suitable for the application as pipe material.

The main properties of the material grade are listed in table 2.1. A schematic image of a nearly unbranched HDPE chain is shown in figure 2.3(b).

2.2.3. Molecular structure of polyethylene

PE is as semicrystalline material composed of amorphous and crystalline fractions with varying compositions. The crystalline areas are characterised by a regular arrangement of densely packed PE chains. The chains order in an orthorhombic unit cell. The asymmetric unit (primitive basis) of the PE unit cell consists of 3 atoms: a single carbon atom and two hydrogen atoms at the following fractional coordinates [92]:

atom	x/a	y/b	z/c
C	0.047	-0.047	0.25
H	0.190	-0.027	0.25
H	0.017	-0.257	0.25

Tab. 2.2.: Fractional coordinates of the atoms in the asymmetric unit of PE in terms of the lattice constants a, b, and c.

The crystal structure is shown in figure 2.4. The lattice parameters of the PE unit cell are $a = 7.4241\,\text{Å}$, $b = 4.9491\,\text{Å}$ and $c = 2.5534\,\text{Å}$ [28]. The space group is $Pnam$ [84, 28]. The macromolecular chains of PE pass through the cell in the direction of the c-axis of the unit cell and every unit cell is occupied by two chains. A more detailed description of crystalline order in solid bodies is given in sec. 3.1.1.

Depending on the size of the crystallite, the chains are too long to fit completely into the corresponding number of unit cells. As a result, the chains either stick out of the crystal surface and possibly reach into the next crystallite or they bend back into the crystallite. In this case the crystallites are called chain-folded.

When the crystallite size is increased, an entire PE chain fits into the crystallite. In that case the crystallites are denominated chain-extended. A detailed description of the formation process of chain-extended and chain-folded PE crystallites and can be found in [66, 70].

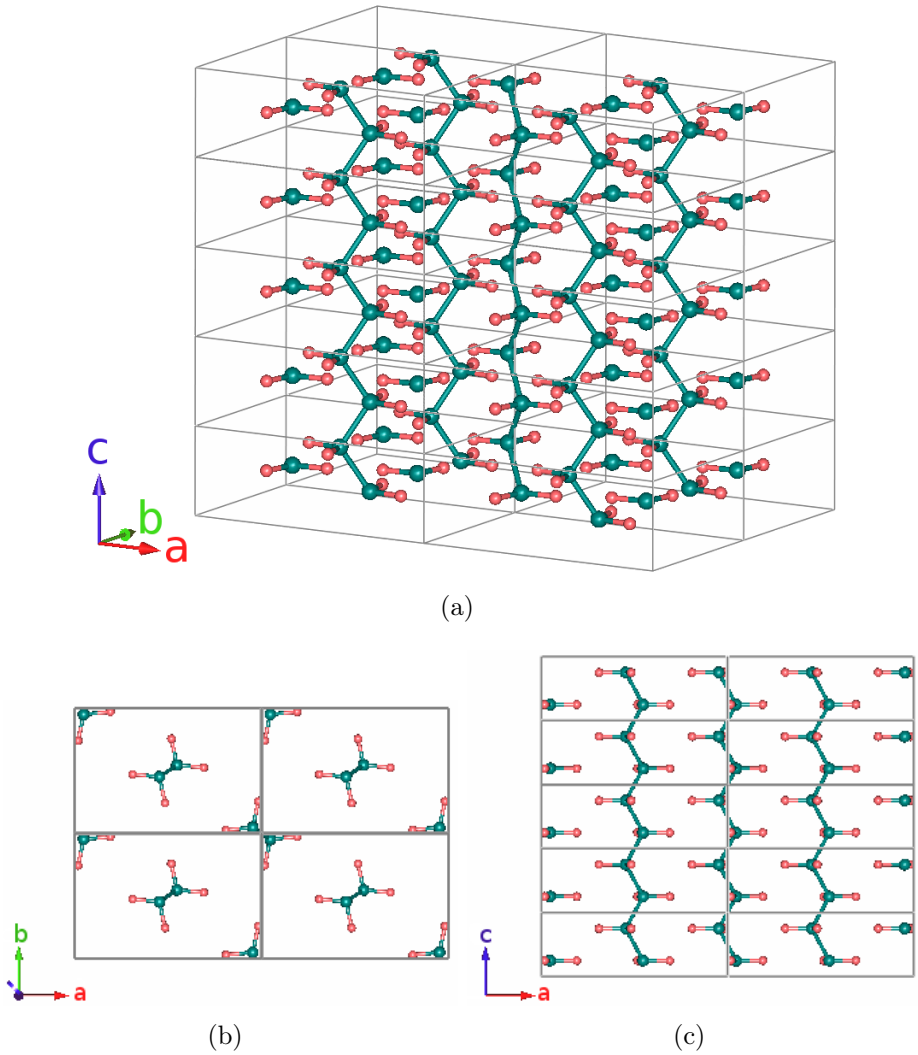

Fig. 2.4.: (Non-primitive) PE unit cells from different viewing angles: (a) Entire unit cell. (b) Top view. (c) Front view.

The amorphous regions of PE solid body are characterised by randomly oriented and entangled chains.

2.2.4. Superstructure of polyethylene

In semicrystalline materials amorphous and crystalline domains are randomly located in the solid body. In the case of PE the crystallites aggregate to large, lamellar structures, which are depicted in figure 2.5(a).

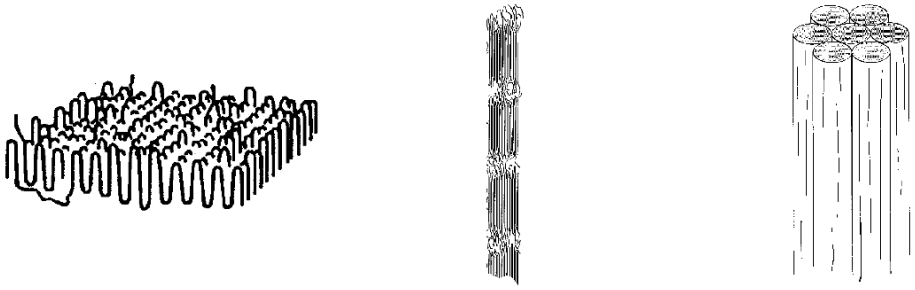

(a) Lamellar crystallite (b) Fibre (c) Fibril

Fig. 2.5.: Development from an individual lamellar crystallite [13] to a fibre with alternating crystalline and amorphous layers and to a fibril (fibre bundle) [66].

Alternating crystalline lamellae and layers of amorphous PE are part of fibres. This can be described using a two-phase model with crystalline layers of thickness d_c and amorphous layers of thickness d_a that add up to the longspacing d_{ac}. The two-phase model (see section 3.1.4) is used for the description of the mesoscopic scattering signal in section 3.4. A fibrillar structure is formed by aggregated fibres.

When the crystallisation of PE starts at a single nucleus point, crystalline lamellae arrange in a starlike structure, which is called spherulite. An example of a spherulite is shown in figure 2.6. The left hand side shows a schematic representation of star like ordered lamellae. The right hand side displays an optical micrograph of spherulites. The concentric rings result from lamellar sections, which are rotated about 90 ° with respect to each other.

Another superstructure is a combination of fibrillar and spherulite structures. The basic element is a fibril, consisting of fibres with amorphous and crystalline layers. These bundles are encapsulated by spherulites. A schematic image of this superstructure can be seen in figure 2.7(a). This structure is denominated shish-kebab structure, following the notation of Hosemann *et al.* [43, 67]. A TEM image of a PE shish-kebab superstructure

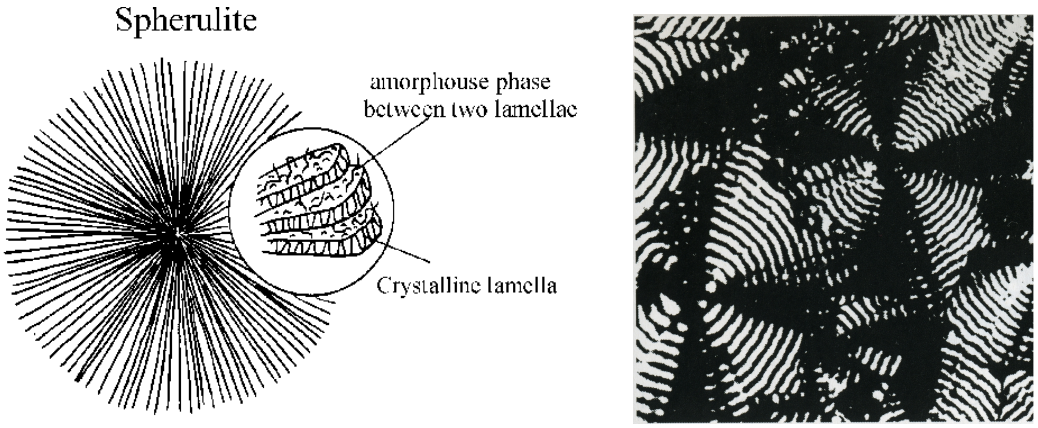

(a) (b)

Fig. 2.6.: (a) Schematic representation of a spherulite structure [79]. (b) Spherulite structure of PE, optical micrograph [89]..

for better visualisation is shown in fig. 2.7(b). In this notation, shishs represent fibrils, while kebabs can be identified as spherulites.

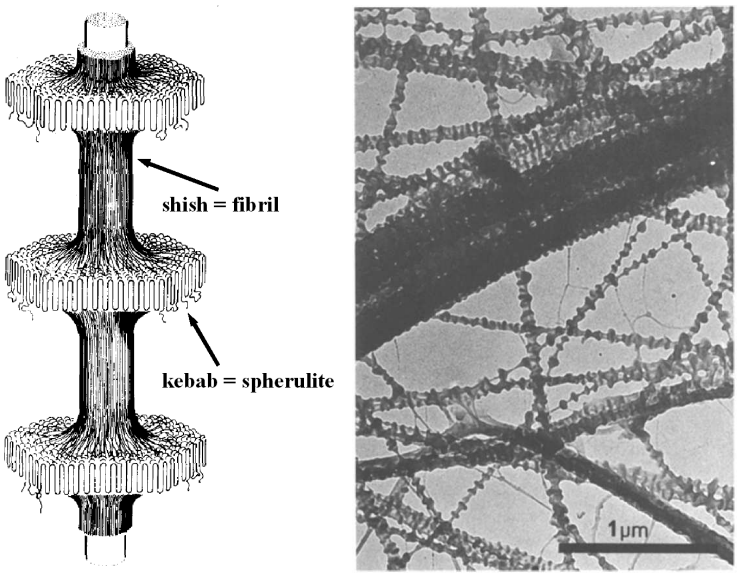

(a) (b)

Fig. 2.7.: (a) Schematic image of a shish-kebab structure as proposed by Hosemann, i.e. fibril encapsulated with spherulites [67]. (b) TEM image of a shish-kebab superstructure of PE [45].

2.3. Production of gas pipes

2.3.1. Extrusion – Basic principles

Extrusion is a production process which results in a material grade of fixed cross-sectional profile and arbitrary length. The advantage of this technique is the production of materials with very complex cross-sections.

In the so-called extruder chamber the stock is heated up by a heater to melt, plasticise, homogenise and compress the material. The pressure inside the barrel is increased in order to press the material through the shape-giving die. The extruded material is normally cooled by a water bath. The basic elements of an extrusion apparatus are depicted in fig. 2.8.

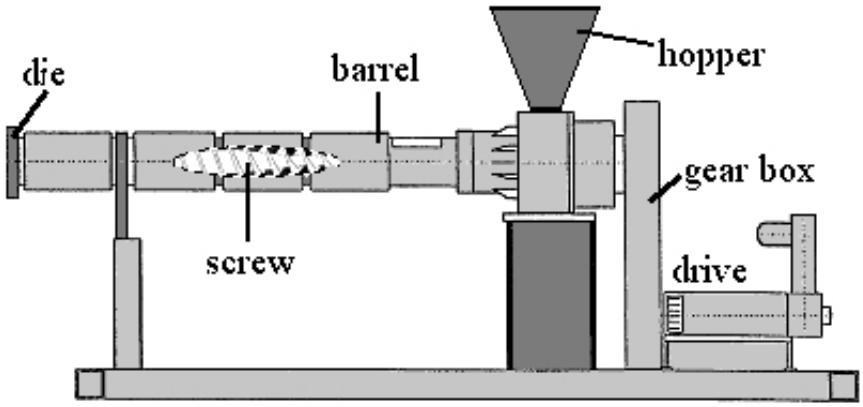

Fig. 2.8.: Schematic image of an extrusion apparatus. The raw material comes from the hopper into the extruder chamber, where it is heated up by successive heater elements, which are placed over the whole length of the barrel. The emerging melt is pressed by the rotating extrusion screw in the direction of the shape-giving die. The viscous paste is pressed through the die by a dummy block. This shape-giving process is followed by the cooling of the pipe.

Different extrusion defects can arise. Surface cracking can occur due to the extrusion temperature, friction or too high speed, but also at lower temperatures, when the extruded material sticks at the die. A flow pattern transports surface oxides and impurities to the centre of the material grade due to tensions or decreasing temperature of the outer regions of the billet. Surface lines across the surface of the extruded profile are caused by a low quality die.

2.3.2. Plastics extrusion

The raw material (small beads), additives like plasticisers, colourants and UV inhibitors in liquid or solid form are filled into the barrel. Within the barrel the beats are heated up to the required melting temperature between 220 and 250 °C [81], depending on the raw material. A gradual heating is achieved by the application of several heating areas, monitored and operated by independent temperature controllers along the barrel from the rear to the front. The advantage is a gradually increased temperature, which reduces the possibility for overheating. The latter might lead to a degradation of the polymer. A temperature control is achieved by a cooling fan. A breaker plate reinforcement at the front end of the barrel reduces pressures that exceed 34 MPa. A screen pack is installed to remove any contaminants from the melt. This assembly additionally generates a back pressure in the barrel, which is required for steady melting and adequate mixing of the polymer and the additives. After cleaning of the molten plastic the material is pressed into the die chamber. The die shapes the molten plastic into its final profile.

Cooling is usually achieved by a water bath. In the further pipe processing the formed plastic moves through a sealed water bath in a carefully controlled vacuum in order to keep the newly formed and still viscous work piece in form. In some cases the water cooling is additionally realised by spraying water onto the moving pipe. Surfactants to seal or label the material grade are applied while the material is still hot.

2.4. Natural ageing of polyethylene materials

In general, ageing is defined as irreversible physical and chemical process, which leads to a degradation of material quality. Besides aggressive chemicals PE suffers from UV radiation, heat exposure, and oxygen exposure, that are responsible for material abrasion.

Chemical ageing causes irreversible modifications of the chemical composition and the molecular structure of the material, like e.g. splitting of polymer chains. Physical ageing involves recrystallisation processes and the relaxation of intra- and intermolecular tensions. Another problem is the loss of plasticisers in the course of time. Different chemical modifications can occur, leading to an ageing of PE. Oxidation is responsible for changed molecular weights and molecular weight distributions, which is the main reason for material failure. It is important to notice that the material grade changes unevenly from the surface to the bulk due to progressing oxidation processes. The reaction rate is determined by the diffusion of O_2 into the vicinity, which is faster for LDPE compared to HDPE. Higher flexibility of the individual chain segments results in higher diffusion rates. Thus oxygen preferentially diffuses into amorphous domains of the material. Crystalline areas are substantially inerter towards auto oxidation [15]. Metal ions catalyse these oxidation processes.

Chemical ageing is influenced by the thermal conditions, as an increasing temperature results in a higher reaction rate. In general the ageing of a material is determined by a combination of thermal-oxidative processes. The diffusion rate of plasticisers is also effected by the temperature.

The absorption of UV radiation with wavelengths below 190 nm is responsible for the breaking of chemical bonds in a PE chain (C–C, C–H) [71], since these photon energies are larger than the binding energies. Due to additives with double-bonds an absorption of UV radiation for wavelengths of $\sim$280 nm occurs [35]. This is not a problem for pure PE, but technical PE exhibits impurities, on purpose or unintended. That is the reason why radiation with longer wavelength has a degrading effect on PE chains. When polymerisation reactions during the synthesis are terminated, endgroups arise, that often exhibit critical chromophores with double bonds that are responsible for the absorption of UV radiation.

Aqueous precipitation is responsible for photo oxidation of polymer foils. Chemicals composed of sulfur compounds and acid rain in combination with UV radiation exposure reduce the lifetime of PE material grades.

Stabilisation of the polymeric matrix can be achieved by the addition of stabilisers that inhibit the auto-oxidation process, chain propagation or chain branching. There are different classes of stabilisers which should only be mentioned here:

- primary and secondary anti-oxidants,
- sun screens: carbon black, UV radiation absorber [87], steric impaired amines (HALS) [62]

For more details see [48, 31].

3. Theory

Polyethylene shows structural characteristics on different length scales. As a semicrystalline material it consists of amorphous and crystalline domains with varying mixing ratios. Crystals are characterised by a high periodicity of the structure and show short as well as long range order. The dimensions of the smallest crystalline structures are in the order of several Å, which are the lattice parameters of the primitive orthorhombic unit cell (see section 2.2.3). In contrast, amorphous materials only possess a short range order of the constituting atoms. The solid body of PE shows characteristic length scales in the mesoscopic range (10-100 Å). These can be attributed to the lamellar superstructure of the molecules.

Powerful methods to analyse semicrystalline structures like polyethylene are x-ray diffraction techniques like X-Ray Diffraction (XRD) and Small Angle X-Ray Scattering (SAXS).

Atomic length scales can be investigated by XRD or Wide Angle X-ray Scattering (WAXS). XRD provides information about the sample's crystallinity, lattice constants and crystallite sizes. Furthermore, average chain distances in amorphous domains can be detected. SAXS yields information on larger length scales e.g. about the two-phase layer structure and the present superstructure of the PE solid body. These techniques are described in the sections 3.2 and 3.4.

The terms small and wide angle refer to scattering angles, at which the observed structures produce detectable scattering signals. The real space angular positions 2θ of these features in the scattering pattern are connected by the following relation with reciprocal space: $|\vec{q}| = \frac{4\pi}{\lambda} \sin\left(\frac{2\theta}{2}\right)$, whereas q is called wavevector transfer or scattering vector. Approximately, the positions of these features are related to characteristic length scales L within the sample by $q = \frac{2\pi}{L}$.

3.1. Solid state order

In the following, different manifestations of order in solids will be discussed. These are crystalline order, amorphous structures, semicrystalline order and the special case of two-phase layer systems with alternating crystalline and amorphous layers.

3.1.1. Crystalline Solids

A crystalline structure can be identified by the strict order of its structure elements in a fixed pattern. In this arrangement the so-called unit cell is the smallest repetitive unit. An ideal crystal lattice is built up by the infinite repetition of unit cells in the three-dimensional space.

The crystal structure is described by the combination of a so-called translation lattice and a basis. The translation lattice is represented by a set of translation vectors $\vec{a}_i$, $i = 1, 2, 3$:

$$\vec{R}_n = n_1\vec{a}_1 + n_2\vec{a}_2 + n_3\vec{a}_3, \qquad n_i \in \mathbb{Z}. \tag{3.1}$$

$\vec{R}_n$ is the so-called lattice vector. Starting at a lattice point $\vec{r}$ in the crystal, each other lattice point $\vec{r}\,'$ can be reached by

$$\vec{r}\,' = \vec{r} + \vec{R}_n.$$

The unit cell is spanned by the translation vectors $\vec{a}_i$, whereas their choice is ambiguous [21, 51]. The smallest possible unit cell is called primitive unit cell and the associated translation vectors are correspondingly called primitive translation vectors. The primitive translation vectors define the crystallographic axes, whereas non-primitive axis are sometimes more convenient [21, 51].

In a crystal structure, every lattice point is identically occupied by a basis, i.e. an arrangement of atoms or molecules as depicted in 3.1. Thus the basis contains the information of the positions of all atoms in the unit cell. The position $\vec{r}_j$ of an atom j

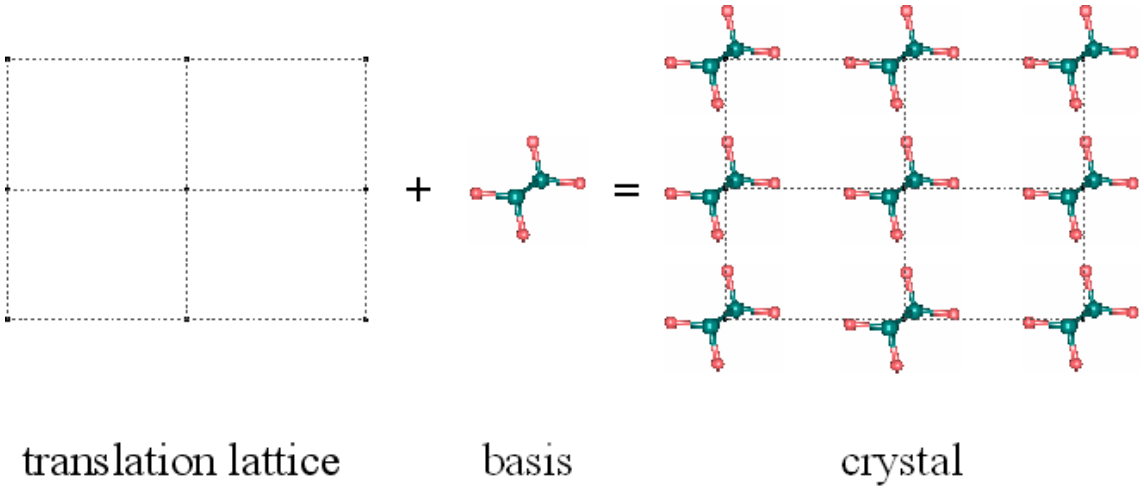

Fig. 3.1.: Deduction of the crystal structure.

of the basis within the primitive unit cell with respect to a lattice point is defined by fractions of the primitive lattice vectors $\vec{a}_i$:

$$\vec{r}_j = x_j\vec{a}_1 + y_j\vec{a}_2 + z_j\vec{a}_3, \qquad j = 1, \ldots, k, \tag{3.2}$$

with $0 \leq x_j,\ y_j,\ z_j \leq 1$.

Various symmetry operations transfer the crystal into itself. Point groups and space groups define and categorise all possible combinations of symmetry operations [93]. There are 32 different point group operations. Translational symmetry operations combine point group operations with translations in the so-called space groups. They include 230 possible symmetry operations at all.

In three-dimensional space there are seven crystal systems with decreasing degree of symmetry and 14 different Bravais lattices.

Of special relevance for this work is the primitive orthorhombic unit cell (see P in fig. 3.2), since polyethylene crystallises in this crystal system. An orthorhombic unit cell is characterised by three differing lattice constants and perpendicular lattice planes.

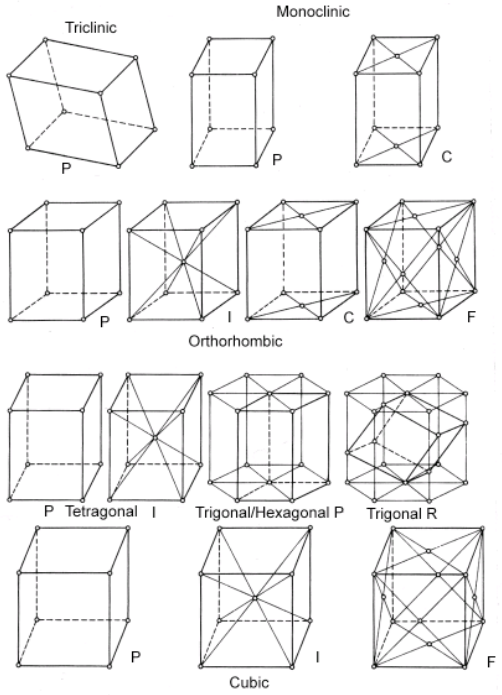

Fig. 3.2.: Bravais lattices [1].

The Fourier transform connects real space with reciprocal space, which becomes important for the calculation of the intensity of scattered x-rays [51]. The reciprocal Bravais lattice is defined by the reciprocal lattice translation vector

$$\vec{G}_{hkl} = h\vec{b}_1 + k\vec{b}_2 + l\vec{b}_3, \qquad h,k,l \in \mathbb{Z}. \tag{3.3}$$

$\vec{b}_i$, $i = 1, 2, 3$, are the primitive translation vectors in reciprocal space and can be calculated using the real space translation vectors $\vec{a}_i$ [51].

The basis vectors $\vec{r}_j$ and the translation vectors are used for the calculation of the unit cell structure factors and the selection rules for the occurrence of a Bragg reflection in an x-ray scattering experiment (see section 3.2.3).

The three-dimensional crystal structure is characterised by lattice planes. The reciprocal lattice translation vectors $\vec{G}_{hkl}$ are perpendicular to the lattice planes, which

are defined by the so-called Miller indices (hkl) [51]. The distance d_{hkl} between two adjacent parallel lattice planes of the family of planes (hkl) is given by

$$d_{hkl} = \frac{2\pi}{|\vec{G}_{hkl}|}. \tag{3.4}$$

3.1.2. Polycrystalline structures

In nature, crystalline solid bodies are frequently not monocrystalline, but polycrystalline. In this case the object consists of small crystallites, which are in a first treatment randomly distributed and oriented with respect to each other. Microcrystalline areas consist of $10^9 - 10^{15}$ atoms. Due to external factors like stress or elevated temperatures a realignment of the microcrystalline areas can be observed [66, 70, 33]. This phenomenon is called texture.

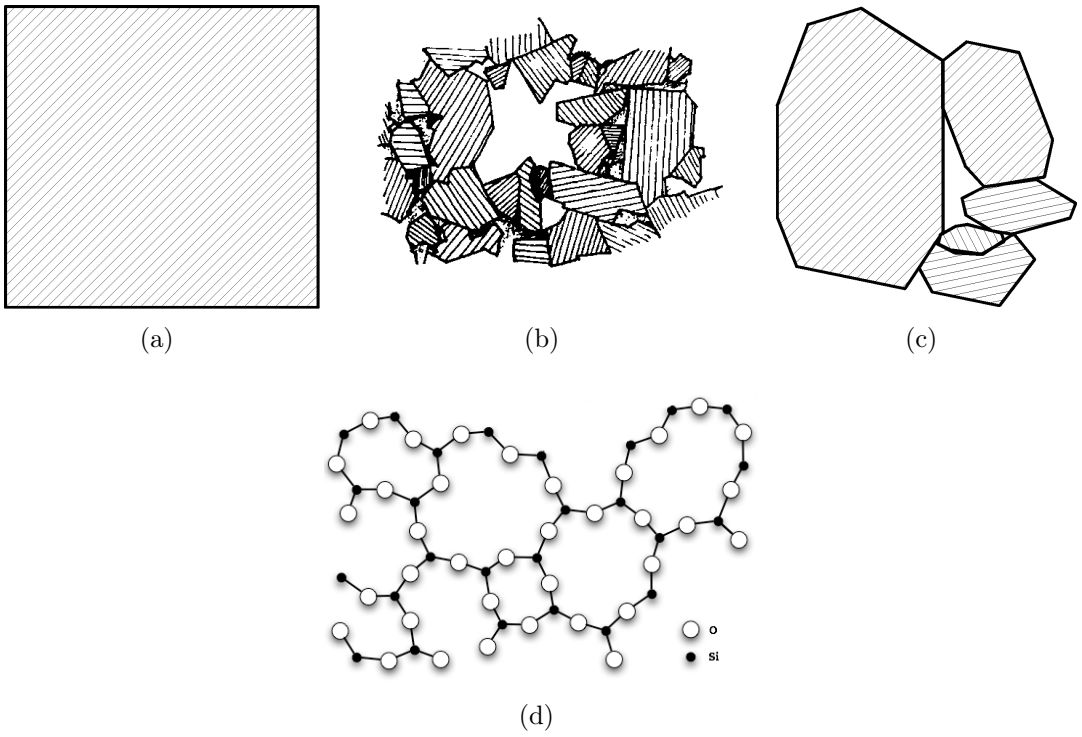

Fig. 3.3.: Crystalline structures: (a) Single-crystal with perfect repetition of lattice planes, (b) Polycrystal with microcrystalline domains [2], (c) Textured polycrystalline structure with few larger microcrystalline domains. (d) An amorphous structure [3].

Figures 3.3 (a) to (c) represent the different manifestations of crystalline structures.

3.1.3. The amorphous state

Amorphous structures are characterised by a non-regular arrangement of their constituents. Thus there does not exist a long-range order. Nevertheless, a short-range order can be observed due to the present chemical bonds. Amorphous structures in PE solid bodies offer a rather low density, since the atoms are not so densely packed (see section 2.2).

Prominent examples for amorphous structures are glasses, but also many polymer materials consist at least partially of amorphous domains. These kind of materials are denominated semicrystalline and characterised by varying ratios of crystalline and amorphous fractions.

3.1.4. Two-phase layer system

In the model supposed by Bonart and Hosemann [52, 23, 43] PE consists of lamellae that are composed of alternating crystalline and amorphous layers. A schematic image of the two-phase layer system is depicted in fig. 3.4. The different layers are characterised by the layer thicknesses d_c and d_a of the crystalline and amorphous layer, that add up to the so-called longspacing or long period d_{ac}.

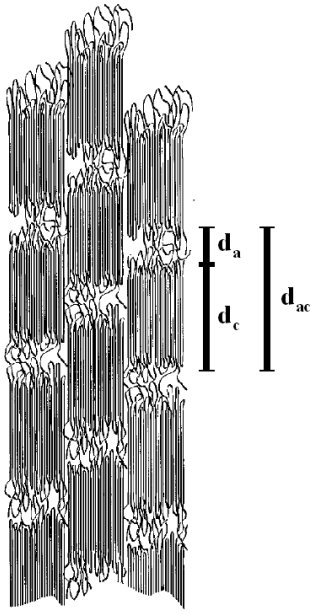

Fig. 3.4.: Schematic image of a two-phase layer system with longspacing d_{ac}, thickness d_c of the crystalline lamella and the amorphous layer thickness d_a [66].

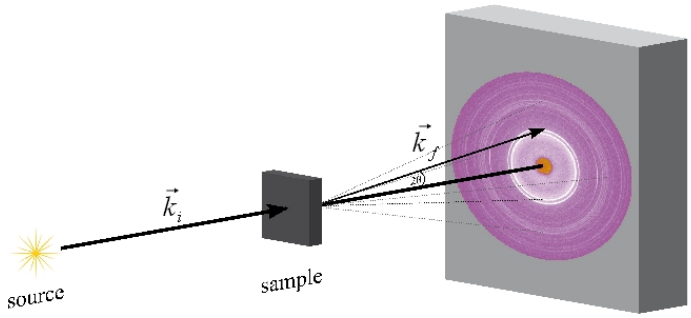

Fig. 3.5.: Transmission scattering geometry. A monochromatic x-ray beam with wavelength λ and wavevector $\vec{k}_i$ hits the sample.

3.2. Theory of x-ray scattering

In the following sections the theory of x-ray scattering will be discussed. First the general scattering geometry will be presented, followed by a discussion of the basic theory. Afterwards, the scattering function of scattering from polycrystalline and amorphous material will be deduced. At the end of the section, the theory of small angle scattering will be presented.

3.2.1. Scattering from a single scattering centre

All experiments performed in the course of this thesis have been accomplished in transmission (scattering) geometry, as depicted in fig. 3.5. An electromagnetic plane wave with wavelength λ (energy $E = \frac{\mathrm{h\,c}}{\lambda}$ with the Planck constant h and the velocity of light c) and momentum $\hbar\vec{k}_i$ impinges on the scattering material. The electrons within the sample are forced to oscillate and emit dipole radiation [46]. The scattered radiation is detected by a two-dimensionally resolving detector.

The wavevector transfer $\vec{q}$, also denominated as scattering vector, is defined as

$$\vec{q} = \vec{k}_f - \vec{k}_i, \tag{3.5}$$

with the initial and final wavevectors $\vec{k}_i$ and $\vec{k}_f$. In the case of elastic scattering the energy (and therefore the wavelength) remains constant, $|\vec{k}_i| = |\vec{k}_f| = \frac{2\pi}{\lambda}$. In terms of the scattering angle 2θ, the absolute value of the scattering vector is defined as

$$|\vec{q}| = q = \frac{4\pi}{\lambda} \sin\left(\frac{2\theta}{2}\right). \tag{3.6}$$

3.2.2. Differential cross-section

In an x-ray scattering experiment, the intensity $I_{\mathrm{sc}}$of the scattered radiation is measured. It is associated to the differential cross-section $\left(\frac{d\sigma}{d\Omega}\right)$, which is defined as

$$\left(\frac{d\sigma}{d\Omega}\right) = \frac{I_{\mathrm{sc}}}{(I_0/A_0)\Delta\Omega}, \tag{3.7}$$

with the incident intensity I_0, the cross-sectional area A_0 and the covered solid-angle $\Delta\Omega$ of the detector.

$\left(\frac{d\sigma}{d\Omega}\right)$ is the experimentally accessible quantity and can be expressed as the product of the scattering function $S(\vec{q})$ and the intrinsic Thomson scattering cross-section $\left(\frac{d\sigma}{d\Omega}\right)_0$:

$$\left(\frac{d\sigma}{d\Omega}\right) = \left(\frac{d\sigma}{d\Omega}\right)_0 S(\vec{q}). \tag{3.8}$$

The first term describes the coupling between an electron and the incident electromagnetic wave [86],

$$\left(\frac{d\sigma}{d\Omega}\right)_0 = \left(\frac{\mathrm{e}^2}{4\pi\varepsilon_0 \mathrm{m_e c}^2}\right)^2 \approx 2.8 \cdot 10^{-5}\,\text{Å} = 2.8 \cdot 10^{-15}\mathrm{m} \tag{3.9}$$

with the electron charge e, the dielectric constant ε_0 and the electron mass $\mathrm{m_e}$.

The scattering function $S(\vec{q})$ reflects the structure of the sample and is defined as the modulus squared of the sample structure factor $F(\vec{q})$ of the sample

$$S(\vec{q}) = |F(\vec{q})|^2. \tag{3.10}$$

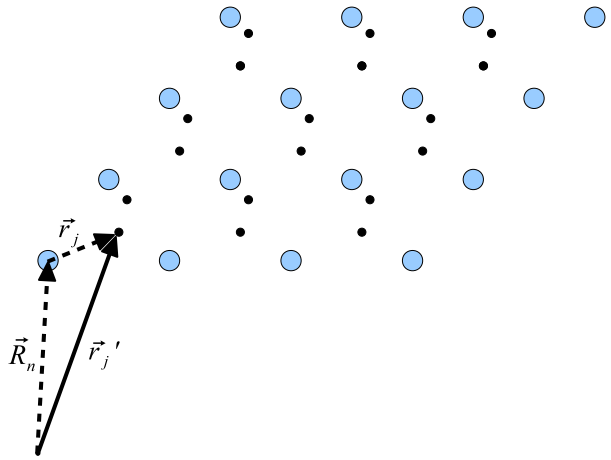

Fig. 3.6.: Replacement of the position vector $\vec{r}_j\,'$ by the sum of the lattice vector $\vec{R}_n$ and the unit cell position vector $\vec{r}_j$, as defined in sec. 3.1.1.

The structure factor $F(\vec{q})$ is the fourier transform of the scattering length density (electron density distribution) $\rho(\vec{r})$ of the sample:

$$F(\vec{q}) = \int \rho(\vec{r}) e^{i\vec{q}\cdot\vec{r}} d\vec{r}. \tag{3.11}$$

3.2.3. The scattering function of a crystal lattice

Because of its periodicity, the scattering length density $\rho(\vec{r})$ of a crystal is invariant with respect to lattice translations $\vec{R}_n$: $\rho(\vec{r}) = \rho(\vec{r} + \vec{R}_n)$. Thus, a discrete description of the structure factor seems natural and the scattering length density can be expanded to a Fourier series:

$$F(\vec{q}) = \sum_{r'_j} f_j(\vec{q}) e^{i\vec{q}\cdot\vec{r}'_j}, \tag{3.12}$$

with the atomic form factor $f_j(\vec{q})$, which describes the scattered x-rays from a single atom. The sum over the vectors $\vec{r}'_j$ includes all atoms within the crystal.

The position vector $\vec{r}_j\,'$ is the vector between the origin and the atom j within the unit cell of a crystal. It can be replaced by a sum of the translation vector $\vec{R}_n$ and the position vector $\vec{r}_j$ within the unit cell, as depicted in fig. 3.6, yielding

$$F(\vec{q}) = \sum_{\vec{r}_j} f_j(\vec{q}) e^{i\vec{q}\cdot\vec{r}_j} \cdot \sum_{\vec{R}_n}^{N} e^{i\vec{q}\cdot\vec{R}_n} \tag{3.13}$$

$$= F^{\mathrm{uc}}_{hkl}(\vec{q}) \cdot S_N(\vec{q}). \tag{3.14}$$

The first term F^{uc}_{hkl} is denominated as unit cell structure factor and describes the scattering from a basis of atoms or molecules in the crystalline unit cell. The second term $S_N(\vec{q})$, denominated as lattice sum, regards the phase between waves scattered at N different unit cells of the entire crystal. The lattice sum determines the positions of Bragg reflections, while the unit cell structure factor modulates the intensity of the peaks. The analysis of the lattice sums leads to the Laue interference function. In the limit of large N the Laue interference function becomes a δ distribution.

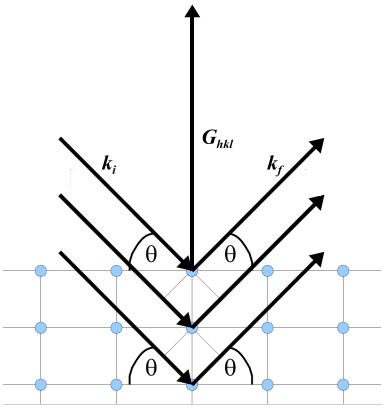

Fig. 3.7.: Bragg scattering at a set of parallel lattice planes. Incident parallel x-rays hit the surface of a crystal and are partially reflected and partially transmitted by the topmost plane. The transmitted beams are then reflected by subjacent parallel lattice planes in the distance d_{hkl}.

The lattice sum provides the maximum intensity contribution, when the product $\vec{q}\cdot\vec{R}_n$ is an integer multiple of 2π. This condition is fulfilled, when the wavevector transfer $\vec{q}$ equals a reciprocal lattice vector: $\vec{q} = \vec{G}_{hkl}$. Here one yields

$$\vec{G}_{hkl}\cdot\vec{R}_n = 2\pi(hn_1 + kn_2 + ln_3), \tag{3.15}$$

$$= 2\pi m,\ m \in \mathbb{Z}. \tag{3.16}$$

$\vec{q} = \vec{G}_{hkl}$ is the so-called Laue condition. Bragg's law follows directly from the Laue condition using $d_{hkl} = \frac{2\pi}{G_{hkl}}$ to $\lambda = 2d_{hkl}\sin(2\theta/2)$. Fig. 3.7 should pronounce the used

relations. If the path length difference between incident and outgoing beam is an integer multiple of the wavelength λ of the radiation, constructive interference between various reflected beams can occur.

For the deduction of the intensity distribution of the scattered radiation the calculation of the lattice sum is required. Following [19], it yields for an ideal, infinitely large crystal a δ function:

$$|S_N(\vec{q})|^2 = \underbrace{N_x \cdot N_y \cdot N_z}_{N} \cdot V_{uc}^* \cdot \delta(\vec{q} - \vec{G}_{hkl}), \tag{3.17}$$

with the total number of scattering unit cells N.

The differential cross-section for a crystalline sample is thus given by

$$\left(\frac{d\sigma}{d\Omega}\right) = r_0^2 P |F_{hkl}^{\mathrm{uc}}(\vec{q})|^2 \mathrm{N}\ V_{\mathrm{uc}}^* \delta(\vec{q} - \vec{G}_{hkl}). \tag{3.18}$$

Like every dipole, no radiation is emitted along the oscillation axis. This circumstance is incorporated with the source-depending so-called polarisation P, which is in the case of the horizontal polarisation of a synchrotron x-ray beam and a horizontal scattering plane given by $P = \cos^2\psi$ (ψ: observation angle). For vertical scattering planes the polarisation is $P = 1$.

Since a polyethylene solid body is a polycrystalline material and thus composed of randomly oriented crystallites, an isotropic scattering distribution can be expected. Due to this fact the scattering of x-rays by a polycrystalline powder will be deduced in the following section.

3.2.4. Powder diffraction

In order to calculate the scattering contribution of a crystalline powder, all possible orientations of the crystallites must be considered. The lattice sum has to be averaged over all possible orientations of the wavevector $\vec{k}_f$. According to [19], the following integral has to be solved:

$$\int d\hat{\vec{k}}_f \delta(\vec{q} - \vec{G}_{hkl}) = \int d\hat{\vec{k}}_f \delta(\vec{k}_f - \vec{k}_i - \vec{G}_{hkl}), \tag{3.19}$$

with the unit vector $d\hat{\vec{k}}_f$ in the direction of $\vec{k}_f$. Using $|\vec{k}_f| = |\vec{k}_i|$ the solution yields

$$\int d\hat{\vec{k}}_f \delta(\vec{k}_f - \vec{k}_i - \vec{G}_{hkl}) = \frac{2}{k_i} \delta(G_{hkl}^2 - 2k_i G_{hkl} \sin(\theta)), \tag{3.20}$$

with the scattering half angle θ.

Substitution of $\delta(\vec{q} - \vec{G}_{hkl})$ by (3.20) in (3.18) yields

$$\left\langle \left(\frac{d\sigma}{d\Omega} \right) \right\rangle_{\vec{k}_f} = r_0^2 P |F_{hkl}^{\mathrm{uc}}(\vec{q})|^2 \mathrm{N} V_{\mathrm{uc}}^* \frac{2}{k_i} \delta(G_{hkl}^2 - 2k_i G_{hkl} \sin(\theta)). \tag{3.21}$$

Thus, the cross-section depends only on the length of the scattering vector and no longer on the direction. Each vector $\vec{G}_{hkl}$ with length $|\vec{G}_{hkl}| = G_{hkl}$ fulfilling the non-vectorial Laue condition $\delta(G_{hkl}^2 - 2k_i G_{hkl} \sin(\theta))$ leads to a non-zero contribution to the cross-section. When an incoming x-ray beam hits a polycrystalline sample, ideally composed of many small crystallites with random orientation with respect of each other, the Bragg scattering condition $\vec{q} \stackrel{!}{=} \vec{G}_{hkl}$ is always fulfilled for a set of parallel [hkl] planes. The resulting cone is the Debye-Scherrer cone [19] with opening angle 2θ. The scattering pattern is thus composed of Debye-Scherrer rings with varying radii, that correspond to the involved lattice planes (hkl). If the isotropy is high, the intensity distribution over a ring is homogeneous.

Due to external forces either during the synthesis or the use of the material grade, it is possible to produce a less polycrystalline but textured material. In this case, a larger amount of crystallites possesses a preferred orientation. Thus, the isotropy is disturbed. This also shows up in the scattering pattern as texture. In this case, the Debye-Scherrer

(a) (b) (c)

Fig. 3.8.: Exemplary scattering patterns (a) of pure amorphous PE with broad halo, (b) of a semicrystalline PE sample, which is a superposition of amorphous (dark circular shadow) and crystalline scattering contributions (light circles), and (c) of a textured PE sample.

cones are no longer isotropically illuminated, but show higher irradiated spots or arcs in the direction of the preferred orientation, as can be seen in the example of a texture PE sample. The corresponding 2D scattering pattern is depicted in fig. 3.8(c).

3.2.5. Scattering from amorphous material

Due to the missing long-range order, scattering from amorphous structures cannot result in sharp diffraction peaks. There are different approaches for the description of scattering from amorphous material. One common possibility to incorporate the amorphous scattering contribution I_{am} is the Debye formulation [30], suggested in [53, 47, 28]:

$$I_{\mathrm{am}}(q) = \sum_{n=1}^{N} \sum_{m=1}^{N} f_n f_m \frac{\sin(q r_{mn})}{q r_{mn}}, \tag{3.22}$$

with the molecular formfactors f_m and f_n of adjacent scatterers with average distances $r_{nm} = |\vec{r}_{nm}|$. Eq. 3.22 follows from the averaging of the phase factor $|\sum_{\vec{r}_n} e^{i\vec{q}\cdot\vec{r}_n}|^2$ over the total solid angle $d\Omega$:

$$\left\langle \left| \sum_{\vec{r}_n} e^{i\vec{q}\cdot\vec{r}_n} \right|^2 \right\rangle_\Omega = \sum_{\vec{r}_n}\sum_{\vec{r}_m} \frac{1}{4\pi} \int d\Omega r^{i\vec{q}\cdot r_{nm}}, \tag{3.23}$$

$$= \frac{1}{4\pi} \int_0^{2\pi} d\phi \int_0^{\pi} \sin\theta d\theta e^{iqr_{nm}\cos\theta}, \tag{3.24}$$

$$= \sum_n \sum_m \frac{\sin(qr_{nm})}{qr_{nm}}, \tag{3.25}$$

with the angle θ between wavevector $\vec{q}$ and $\vec{r}_{nm}$.

Scattering from amorphous materials shows up in diffraction patterns as broad halos, as can be seen in 3.8(a). In semicrystalline materials, amorphous and crystalline domains contribute simultaneously to the scattering pattern. The resulting scattering pattern is a superposition of amorphous and crystalline scattering signals and looks like the exemplary WAXS pattern of semicrystalline PE depicted in 3.8(b).

3.3. The diffraction signal of semicrystalline polyethylene

When taking all atom positions and symmetry operations of space group *Pnam* into account, the list in table 3.1 of reflections with peak positions referring to a photon energy of $E = 27\,\text{keV}$ is obtained:

The corresponding powder diffraction pattern with superimposed amorphous scattering contribution is depicted in fig. 3.9.

The dimension of the unit cell can be determined from the positions of the Bragg reflections in a powder diffraction pattern. The ratio of crystalline scattering contribution and total scattering intensity yields the samples crystallinity. The crystallite sizes in certain directions follow from the full width at half maximum of the diffraction peaks. As complementary technique for the determination of material crystallinities serve small angle x-ray scattering experiments.

hkl	$S(q)$	2θ [°]	q [Å^{-1}]	D [Å]
110	147.8487	6.3927	4.115994	1.526529
200	127.0782	7.0968	3.708100	1.694449
210	27.7492	8.8717	2.967315	2.117465
020	92.8907	10.6454	2.474000	2.539687
120	22.6670	11.2239	2.346859	2.677274
011	49.7132	11.6359	2.264023	2.775231
310	47.5253	11.9137	2.211429	2.841233
111	42.3456	12.1680	2.165368	2.901671
201	68.2638	12.5543	2.099000	2.993419
220	42.6223	12.8054	2.057997	3.053058
211	33.5177	13.6421	1.932322	3.251625
400	45.6914	14.2210	1.854050	3.388897
320	34.0470	15.0826	1.748698	3.593064
410	25.1027	15.1920	1.736168	3.618995
121	44.3100	15.2852	1.725655	3.641044
311	54.6293	15.8014	1.669619	3.763244

Tab. 3.1.: List of possible diffraction peaks ($E = 27\,\mathrm{keV}$), calculated from the lattice positions presented in tab. 2.2 and applying space group *Pnam* in the scattering angle range between 0 and 16 °.

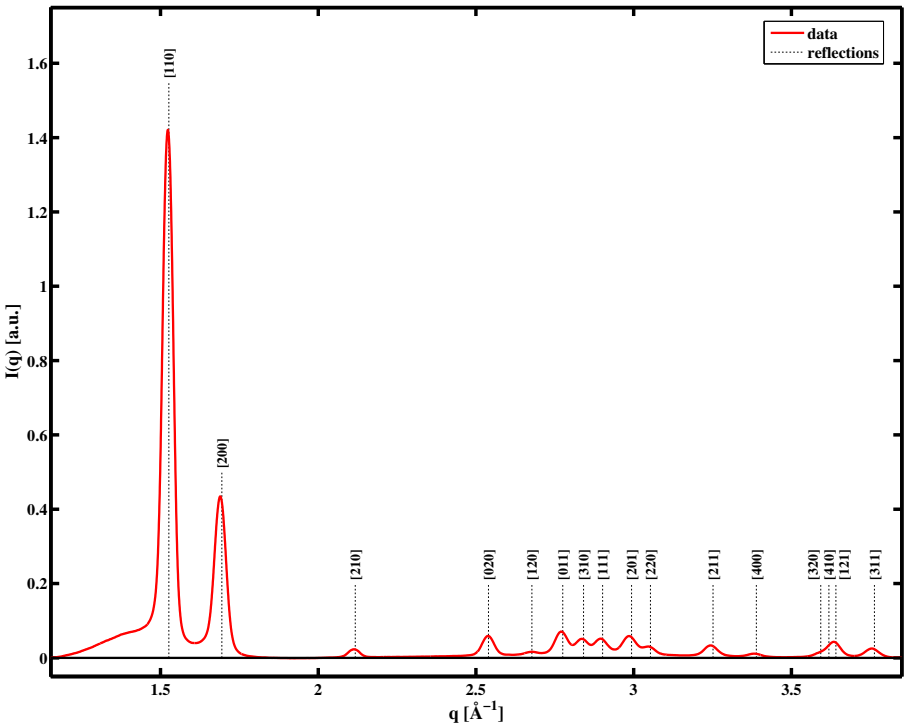

Fig. 3.9.: Exemplary isotropic powder pattern of semicrystalline PE.

3.4. Small angle x-ray scattering at mesoscopic structures

Structures in the order of several 10 to 100 Å are, according to $q = \frac{2\pi}{L}$, responsible for scattering signals observable at low q. The Small Angle X-Ray Scattering technique (SAXS) is thus a suitable tool to examine structures on these length scales.

If the structures within the samples investigated by SAXS do not possess preferred orientation, a homogeneous intensity distribution of the scattered intensity can be observed.

Sample systems analysed by SAXS are in general disordered systems, like e.g. polymers or proteins in solution [77], defects (inhomogenities in the electron density distribution) or amorphous domains in solid bodies [32]. Furthermore, the small angle scattering technique is an adequate tool to obtain the supermolecular structure. During the quantitative data analysis of two-phase layer systems like PE, the determination of the correlation function offers the opportunity to deduce the longspacing and the crystalline thickness within the lamellar system. Additionally, the sample's crystallinity directly follows from the ratio of these two quantities.

In the case of samples showing a preferred orientation, an anisotropy can be observed in the two-dimensional scattering pattern.

3.4.1. Theory of Small Angle X-Ray Scattering

The differential cross-section per unit volume $\Sigma(\vec{q})$ can be defined as

$$\Sigma(\vec{q}) = \frac{1}{V}\frac{d\sigma}{d\Omega} = \frac{1}{V}\frac{I(\vec{q})}{I_0/A_0^2}, \tag{3.26}$$

with the incident intensity I_0, the area A of the sample illuminated by the beam and the unit volume V. The cross-section thus depends on the scattering intensity $I(\vec{q})$ of the particles exposed to the beam. In the case of x-rays, the scattering intensity is determined by the electron density distribution of the scattering material. For polymer systems, monomeric units of the macromolecules are these scattering particles. When these monomers are identical, the scattering properties are represented by the scattering function $S(\vec{q})$. The scattering function is given by

$$S(\vec{q}) = \frac{I(\vec{q})}{I_m N_m}, \tag{3.27}$$

with the number N_m of scattering particles (monomeric units) and the scattering intensity I_m per single monomer. The relation between the differential cross-section and the scattering function is

$$\Sigma(\vec{q}) = \langle\rho_m\rangle \left(\frac{d\sigma}{d\Omega}\right)_m \cdot S(\vec{q}). \tag{3.28}$$

$\langle\rho_m\rangle := \frac{N_m}{V}$ is the mean density of the irradiated material and $\left(\frac{d\sigma}{d\Omega}\right)_m = \frac{I_m(q)}{I_0/A^2}$ is the scattering cross-section per monomer.

The scattering function results from the superposition and interference of waves scattered by the single monomers. The scattering amplitude of these waves is given by

$$C(\vec{q}) = \sum_{i=1}^{N_m} e^{i\vec{q}\cdot\vec{r}_i}. \tag{3.29}$$

The modulus squared of $C(\vec{q})$ is proportional to the scattering intensity:

$$I(\vec{q}) \propto \langle|C(\vec{q})|^2\rangle. \tag{3.30}$$

The differential cross-section can be expressed by means of the scattering amplitude as follows:

$$\Sigma(\vec{q}) = \langle \rho_m \rangle \frac{1}{V} \left(\frac{d\sigma}{d\Omega} \right)_m \frac{1}{N_m} \langle |C(\vec{q})|^2 \rangle, \tag{3.31}$$

The acquisition of a scattering pattern is a measurement of averaged quantities. The ensemble average $\langle \ldots \rangle$ is thus an average of all microscopic states of the sample. In the case of ergodic systems, the time average equals the theoretical ensemble average:

$$S(\vec{q}) = \frac{1}{N_m} \langle |C(\vec{q})|^2 \rangle \tag{3.32}$$

$$= \frac{1}{N_m} \sum_{i,j=1}^{N_m} \langle e^{-i\vec{q} \cdot (\vec{r}_i - \vec{r}_j)} \rangle. \tag{3.33}$$

Describing the particle density distribution by a continuous distribution function $\rho_m(\vec{r})$, if follows:

$$C(\vec{q}) = \int_V e^{-i\vec{q} \cdot \vec{r}} \left(\rho_m(\vec{r}) - \langle \rho_m \rangle \right) d\vec{r}. \tag{3.34}$$

$C(\vec{q})$ is thus the Fourier transformation of density fluctuations within the sample. Substitution of (3.34) into (3.33) gives

$$S(\vec{q}) = \frac{1}{N_m} \int_V \int_V e^{-i\vec{q} \cdot (\vec{r}' - \vec{r}'')} \langle \left(\rho_m(\vec{r}') - \langle \rho_m \rangle \right) \left(\rho_m(\vec{r}'') - \langle \rho_m \rangle \right) \rangle d\vec{r}' d\vec{r}''. \tag{3.35}$$

The double integral reduces to a single integral for some macroscopically homogenous systems [82]. In this case,

$$\langle \rho_m(\vec{r}') \rho_m(\vec{r}'') \rangle = \langle \rho_m(\vec{r}' - \vec{r}'') \rho_m(0) \rangle, \tag{3.36}$$

holds. With $\vec{r} := \vec{r}' - \vec{r}''$, the scattering function is given by

$$S(\vec{q}) = \frac{1}{\langle \rho_m \rangle} \int_V e^{-i\vec{q} \cdot \vec{r}} (\langle \rho_m(\vec{r}) \rho_m(0) \rangle - \langle \rho_m \rangle^2) d\vec{r}. \tag{3.37}$$

The scattering function is thus the Fourier transformation of the mutual correlation function of the particle density.

The characterisation of the scattering particles can be expressed via the pair distribution function $g(\vec{r})$, which is defined as the sum of the self-correlation $\delta(\vec{r})$ and the contribution $g'(\vec{r})$ of neighbouring particles: $g(\vec{r}) = \delta(\vec{r}) + g'(\vec{r})$. $g(\vec{r})d\vec{r}$ gives the probability to find a particle or another one in the vicinity in the volume element $d\vec{r}$ at distance $\vec{r}$. The relation between density distribution and pair distribution function is given by

$$\langle \rho_m(\vec{r})\rho_m(0)\rangle = \langle \rho_m\rangle g(\vec{r}). \tag{3.38}$$

Substitution of (3.38) into the scattering function (3.33) leads to

$$S(\vec{q}) = \int_V e^{-i\vec{q}\cdot\vec{r}}(g(\vec{r}) - \langle\rho_m\rangle)d\vec{r}. \tag{3.39}$$

Here the scattering function is the Fourier transformation of the pair distribution function.

In isotropic systems,

$$g(\vec{r}) = g(|\vec{r}|) = g(r) \tag{3.40}$$

is valid. Hence, the scattering function is also isotropic: $S(\vec{q}) = S(|\vec{q}|) = S(q)$. In that case, it can be reformulated to

$$S(\vec{q}) = \int_V e^{-i\vec{q}\cdot r}(g(\vec{r}) - \langle\rho_m\rangle)d\vec{r} \tag{3.41}$$

$$S(q) = \int_{r=0}^{\infty} \frac{\sin(qr)}{qr} 4\pi r^2 (g(r) - \langle\rho_m\rangle)dr. \tag{3.42}$$

The differential cross-section for an isotropic system is thus given by

$$\Sigma(q) = \langle\rho_m\rangle \left(\frac{d\sigma}{d\Omega}\right)_m \cdot \int_{r=0}^{\infty} \frac{\sin(qr)}{qr} 4\pi r^2 (g(r) - \langle\rho_m\rangle)dr. \tag{3.43}$$

All considerations that have been made so far have been done concerning relative quantities. But also measurements of absolute intensities provide important information on multi-component and multi-phase polymer systems, like e.g. semicrystalline polymer systems.

In a one-component system with z_m electrons, the cross-section per monomer is given by

$$\left(\frac{d\sigma}{d\Omega}\right)_m = z_m^2 r_e^2.$$

The general expression ρ_m is now replaced by the spatially varying electron density $\rho(\vec{r})$, defined as

$$z_m \rho_m(\vec{r}) = \rho_e(\vec{r}). \tag{3.44}$$

Replacement of ρ_m by ρ_e in equation (3.37) yields as differential cross-section for an one-component system in terms of the electron density $\rho_e(\vec{r})$:

$$\Sigma(\vec{q}) = r_e^2 \int_V e^{-i\vec{q}\cdot\vec{r}} (\langle \rho_e(\vec{r})\rho_e(0)\rangle - \langle \rho_e \rangle^2) d\vec{r}. \tag{3.45}$$

3.4.2. Application for semicrystalline two-phase layer systems

In the following, the case of a two-phase layer system should be considered.

Isotropic samples of polycrystalline polymers are organised as an ensemble of packed, isotropically distributed stacks of lamellar crystallites, that are separated by amorphous regions. The stacks possess a large extension in both directions parallel and normal to the lamellar surface compared to interlamellar distances. This results in a scattering behaviour that can be related to the one-dimensional electron density distribution $\rho_e(z)$, when z is the direction parallel to the surface normal of a crystalline lamella. This relation is illustrated in fig. 3.10(b). In contrast, when the spatial orientation of the lamellae is not so well defined, the system in fig. 3.10(a) is observed and only averaged spacings can be determined. In the following considerations the case of lamellar stacking in z-direction will be discussed. In that case, the z-axis passes through amorphous

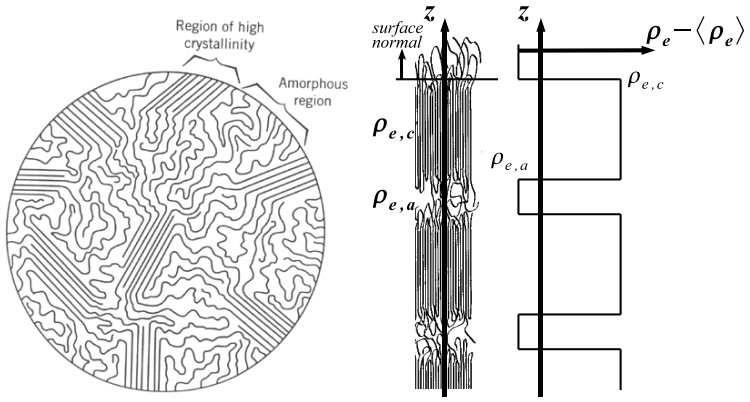

(a) (b)

Fig. 3.10.: (a) Schematic representation of a semicrystalline two-phase system with random orientation of lamellae [4] and with (b) spatial orientation along the z direction. Representation of the one-dimensional electron density distribution $\rho_e(z)$ with respect to the two-phase layer system. Burrowed from [66].

domains described by density $\rho_{e,a}$ and crystallites with density $\rho_{e,c}$. The density $\langle \rho_e \rangle$ is the average of these two limiting values.

The scattering cross-section is given by

$$\Sigma(\vec{q}) = r_e^2 \int_{x,y,z} e^{-i(q_x x + q_y y + q_z z)} \left(\langle \rho_e(z)\rho_e(0) \rangle - \langle \rho_e \rangle^2 \right) dxdydz. \tag{3.46}$$

x- and y- integrations lead to

$$\Sigma(\vec{q}) = r_e^2 (2\pi)^2 \delta(x)\delta(y) \int_{-\infty}^{\infty} e^{-iq_z \cdot z} K(z) dz, \tag{3.47}$$

with the δ distributions $\delta(x)$ and $\delta(y)$ and

$$K(z) = \langle (\rho_e(z) - \langle \rho_e \rangle)(\rho_e(0) - \langle \rho_e \rangle) \rangle \tag{3.48}$$

$$= \langle \rho_e(z)\rho_e(0) \rangle - \langle \rho_e \rangle^2. \tag{3.49}$$

To determine the scattering function, the isotropic average has to be calculated, leading to

$$\Sigma(q) = \frac{2}{4\pi q^2} r_e^2 (2\pi)^2 \int_{-\infty}^{\infty} e^{-iq_z z} K(z) dz. \tag{3.50}$$

The inverse Fourier transform yields the one-dimensional density correlation function

$$K(z) = \frac{1}{2r_e^2} \frac{1}{(2\pi)^3} \int_{-\infty}^{\infty} e^{iq_z z} 4\pi q^2 \Sigma(q) dq. \tag{3.51}$$

Due to the characteristic shape of the correlation function $K(z)$, a determination of the stack structure is possible.

Fig. 3.11 shows the electron density distribution $\rho_e - \langle \rho_e \rangle$ for an ideal stack of crystalline and amorphous lamellae, which is marked by equidistant distances between the individual stacks and constant lamellar thickness. The intensity distribution can be described by the long period $d_{ac} = d_a + d_c$ with the crystallite thickness d_c, the size d_a of the amorphous layer, and the electron density difference $\delta\rho = \rho_{e,c} - \rho_{e,a}$.

The crystallinity of the sample material is defined as ratio of the crystallite thickness d_c and the long period d_{ac} (volume crystallinity):

$$\chi = \frac{d_c}{d_{ac}}. \tag{3.52}$$

In the following, the crystallinity is kept fixed for the moment below 50 %.

First of all, a correlation function for the amorphous phase can be defined as

$$K_a(z) = \langle (\rho_e(z) - \rho_{e,a})(\rho_e(0) - \rho_{e,a}) \rangle. \tag{3.53}$$

Here all electron densities refer to the electron density of the amorphous domains. The ensemble average is equivalent to an average over all points z' within a stack. The correlation function thus can be calculated by

$$K_a(z) = \frac{1}{\Delta} \int_{-\Delta}^{\Delta} [\rho_e(z') - \rho_{e,a}][\rho_e(z + z') - \rho_{e,a}] dz'. \tag{3.54}$$

The integration range Δ includes both phases, amorphous and crystalline domains. Contributions to the integral only arise when two crystalline regions overlap, thus when

$\rho_e(z)$ or $\rho_e(z+z')$ fall into a crystalline domain. For the amorphous correlation function follows (see [82]):

$$K_a(z) = \begin{cases} (\rho_{e,c} - \rho_{e,a})^2 \frac{d_c - z}{d_{ac}} & \text{if } |z| < d_c, \\ 0 & \text{if } d_c < |z| < \underbrace{d_{ac} - d_c}_{d_a}. \end{cases} \tag{3.55}$$

The correlation function is thus periodic in the size of the crystalline lamellae with

$$K_a(z + d_{ac}) = K_a(z). \tag{3.56}$$

The one-dimensional correlation function for the whole system can be determined by

$$K(z) = K_a(z) - (\langle \rho_e \rangle - \rho_{e,a})^2. \tag{3.57}$$

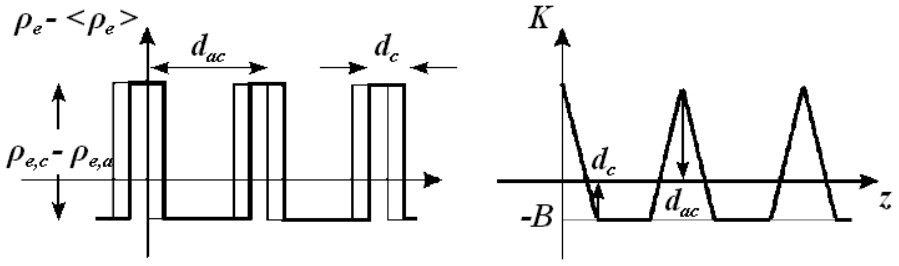

Fig. 3.11.: Density distribution of an ideal two-phase layer system and the corresponding correlation function $K(z)$. Burrowed from [82].

The curve depicted on the right side in figure 3.11 is the correlation function $K(z)$ and follows directly from the electron density distribution on the left hand side of the figure. It shows a regular sequence of triangles, centred at $z = 0,\ z = d_{ac},\ z = 2d_{ac}, \ldots$. The triangles reflect the correlations within one crystallite, between next neighbours, second neighbours, etc. The so-called self-correlation triangle is centring at the origin and intercepts the baseline $-B$ at $z = d_a$.

The correlation function can be approximated for small z as a linear function, which crosses the baseline $-B$ at $z = d_c$. This linear function intersects with the horizontal line marking the minimal value of the correlation function at $z = d_a$, thus forming a triangle.

All presented equations are only valid for ideal stacks as defined before, but can nevertheless be reformulated for the case of non-ideal stacks with varying thicknesses of the amorphous and crystalline domains or diffuse phase boundaries. The first distortions to be considered are fluctuating intercrystalline spacings. The self-correlation part remains constant for this case. There only occurs a broadening of the correlation peak due to diffuse next-neighbour correlations (see fig. 3.12). The self-correlation triangle thus keeps its shape and the quantities d_c and $-B$ can be deduced as before.The correlation peak reflects the most probable distance between neighbouring crystallites. The corresponding quantity is denoted as longspacing.

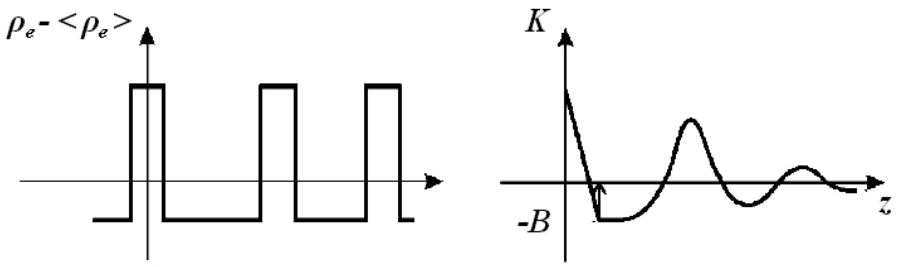

Fig. 3.12.: Density distribution of a two-phase layer system with fluctuating intercrystalline spacings and the corresponding correlation function $K(z)$. Burrowed from [82].

Deviating crystalline thicknesses with constant χ do not lead to a change for the initial slope $\frac{dK(z=0)}{dz}$ or baseline $-B$. In contrast, $K(z)$ becomes curved close to the baseline and at $z = d_c$ (see fig. 3.13).

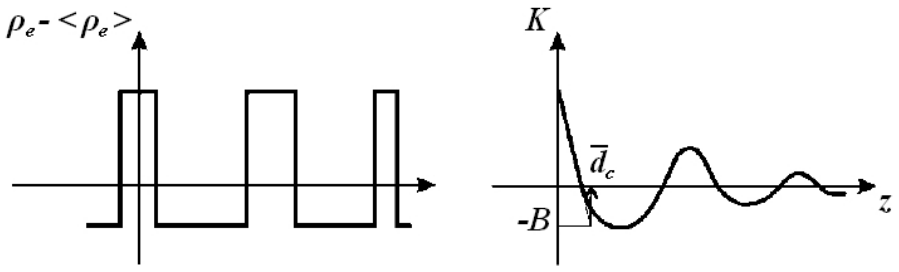

Fig. 3.13.: Density distribution of a two-phase layer system with fluctuating intercrystalline spacings and varying crystalline thicknesses and the corresponding correlation function $K(z)$. Burrowed from [82].

4. Experimental section

4.1. Samples

PE offers several properties, which are beneficial for the application in the supply of gas and water, for example their resistance against all kinds of chemicals and a broad temperature range, in which they can be used. In the following sections the application of PE gas pipes by gas suppliers like e.g. RWE in the past decades and the inspection of the remaining lifetime will be discussed. Afterwards, the gas pipe samples provided by RWE will be presented. In the subsequent sections, the sample preparation of small sample slices and the artificial ageing performed in the scope of this work will be explained.

4.1.1. Polyethylene gas pipes

Shortly after the invention of low pressure PE by Ziegler and Natta in 1955 industrial production of HDPE pipes started. In the same year, the first pipes were installed by Hoechst [73]. Between 1960 and 1978 10000 km gas pipes and 20000 km pipes for the supply of drinking water have been installed [38] at different places. To these belong supply lines in buildings as well as gas and water pipes under streets and pavements, which result in different workloads. The long term stability of pipes in the supply is influenced by several further factors: a proper installation with sand bed for the prevention of point loads and a tension-free laying are very important. Another point is long outdoor storage of pipes before installation, which might also have a lifetime reducing effect due to the irradiation with sun light.

RWE provided a large number of so-called PE63 pipes from different operation places in order to analyse certain material properties. The operation places were pavements and streets, resulting in differing loads onto the pipes.

4.1.2. Simulation of long term stability of polyethylene gas pipes

Creeping tests are a good tool to simulate long term stability and ageing behaviour of PE gas pipes. One possibility is the application of internal pressure creep rupture tests.

In these tests well-defined pressures and elevated temperatures are simultaneously applied to small test specimens of 80 cm length. The time until burst is measured for each combination of stress and temperature. The point of burst is connected to a certain activation energy for material failure. The results of these measurements yield creeping test curves. Using the so-called Modified Arrhenius concept [20, 41], the remaining lifetime for real working conditions can be extrapolated.

PE pipes installed in the early seventies were of PE63 type and belong to the class of HDPE pipes of first generation. These pipes have to withstand a pressure of $6.3\,\mathrm{N/mm^2}$ at temperatures of 80 °C in creeping tests. The predicted lifetime for these type amounts to 50 years. PE80 and PE 100 are HDPE pipes of second and third generation and have to endure pressures of 8.0 and $10.0\,\mathrm{N/mm^2}$ and possess larger expected lifetime. The gas pipes investigated in the scope of this work are of PE63 type. For sample R3 the corresponding information was not available (see tab. 4.1).

Creeping tests

Internal pressure creeping tests were performed by egeplast [1]. An 80 cm long pipe part was closed with caps equipped with valves on top and at the bottom. Via these valves, the creep test pressure p_{ct} higher than the normal operational pressure was applied to the inner surface of the pipe. At the same time the stressed pipe was subject to an elevated temperature T_{ct} higher than the normal working conditions by the use of a water bath from the outside. During these tests the time until burst was measured.

A schematic image of the creeping test apparatus is shown in figure 4.1, while the applied temperatures and pressures are listed up in tab. 4.1. After finishing of the

[1] egeplast Werner Strumann GmbH & Co. KG, Robert-Bosch-Str. 7, D-48268 Greven

creeping tests, the pipe samples 2, 3, 4, and 7 have been used for x-ray diffraction experiments.

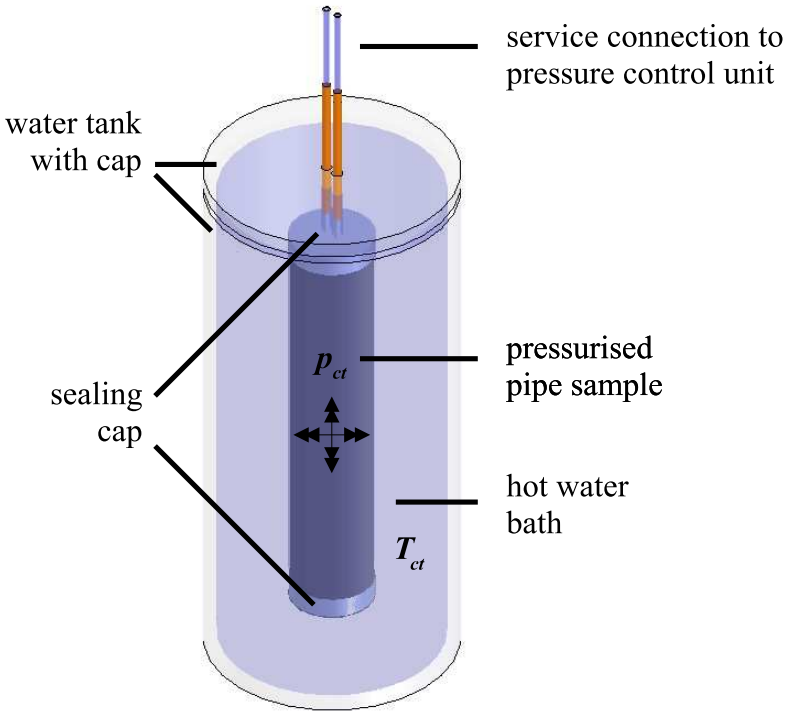

Fig. 4.1.: Schematic image of the creeping test apparatus. The high creeping test pressure p_{ct} is applied to the closed sample volume by a pump, while the stressed sample is subject to the elevated temperature T_{ct} by the use of a water bath.

In order to simulate the ageing behaviour of PE gas pipes, different ageing procedures have been applied to the pipe samples. The artificial ageing of native pipes took place in three different ways:

- creeping tests with entire pipe parts by egeplast,
- ex-situ annealing of pipe sample slices in an oven,
- in-situ annealing of pipe sample slices in a temperature cell.

4.1.3. Pipe samples provided by RWE

RWE provided overall 15 different pipe samples. 11 native pipe samples, denominated from 2 to 11 and R3 were available. A native sample is defined as pipe, that has just been removed from earth and not been treated in any form. Two differently aged pipe samples of the latter could be investigated. Samples aged by creeping tests could be examined for the samples 2, 4 and 7. For the eleven successive labelled samples the following notation holds: the native samples are labelled rX.1 (X = 2, ..., 11), the aged samples are marked by an rX.2, (X = 2, 4, 7). The aged sample of pipe R3 is named R2.

The examined pipes have been in use under different environmental conditions. The pipe samples 2.1, 4.1, 6.1, 7.1, 8.1, 10.1, and 11.1 have been installed under pavements, while the samples 3.1, 5.1 and 9.1 were part of the pipe system under streets (see tab. 4.1, besides other information). For all samples a proper sand-back filling took place. Thus, point loads should have been reduced.

The parts 2 to 9 and 11 as well as the parts R3 and R2 are of the same size. They have a nominal diameter of 160 mm and a wall thickness of 9.1 mm. The exact sizes are presented in tab. 4.1. Pipe 10.1 possesses deviating dimensions. Its wall thickness amounts to 5.1 mm at a diameter of 90 mm.

The creeping tests (see 4.1.2) have been conducted with the pipe samples 2, 3, 4, and 7. The samples 2.2, 3.2 and 4.2 have been aged under identical ageing conditions of 80 °C and a pressure of 4.6 N/mm^2 for 165 hours (until bursting). The last examined aged pipe 7.2 sample has been exposed to the same temperature, but a slightly lower pressure of 4.3 N/mm^2. In this case, the load test lasted 150–300 hours (until bursting).

The samples 5, 6, 8 and 9 have been artificially aged, too. The ageing conditions are listed up in tab. 4.1. For samples 1, 10 and 11 no information about creep testing are available until now.

While the samples 2.2, 4.2 and 7.2 were examined during a beamtime at DELTA, the other samples haven't been on hand for experiments. The creeping tests of the samples 5, 6, 8, 9, 10, and 11 have not been finished yet at the time of experiments.

Sample label	Sample state	Ageing conditions p [N/mm^2]	T [°C]	t [h]	Ø [mm]	Wall thickness [mm]	Manufacturing date	Operating place
2.1	native				160	9.1	30.03.78	pavement
2.2	aged	4.6	80	165				
3.1	native				160	9.1	15.05.79	street
4.1	native				160	9.1		pavement
4.2	aged	4.6	80	165				
5.1	native				160	9.1	09.07.79	street
6.1	native				160	9.1		pavement
7.1	native				160	9.1	28.03.76	pavement
7.2	aged	4.3	80	150–300				
8.1	native				160	9.1	28.03.76	pavement
9.1	native				160	9.1	30.06.76	street
10.1	native				90	5.1	06.07.78	pavement
11.1	native				160	9.1		pavement
R3	native				160	9.1		
R2	aged							

Tab. 4.1.: Examined samples with information about dimensions, ageing conditions (pressure, temperature and time to withstand), working place and manufacturing date. Information was provided by *RWE Westfalen-Weser-Ems Netzservice GmbH*.

4.1.4. Sample preparation

The first step is the preparation of a 1 cm broad stripe over the whole length out of the pipe wall along the long axis of the pipe. This stripe is divided into 4 cuboids of equal size. In a second step, the cuboids are divided into slices along the radius of the pipe wall. This procedure yields 4 sample slices of PE, 2 surface slices and 2 bulk slices. The steps in sample preparation are visualised in fig. 4.2. There are two reasons for this

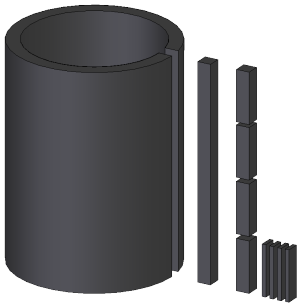

Fig. 4.2.: Sample preparation. After sawing a 1 cm broad stripe out of the pipe wall, it is divided into cuboids. Afterwards, these cuboids are divided into slices along the radius of the pipe wall.

preparation of rather thin slices. First of all the samples should not be too thick due to the low x-ray energy at the laboratory source in Helsinki (see section 4.2.5). The second and more important reason is the aim of position dependent investigations of pipe properties, since all properties of the material grade depend on the position, e.g. at outer surface or inner surface.

The sample preparation of a pipe part with a diameter of 22.5 cm and pipe wall thickness of 12.8 mm in the above described way yielded 6 sample slices, 2 surface slices and 4 bulk slices. The last pipe part had a diameter of 9 cm and a pipe wall thickness of 5.1 mm. In this case it was possible to prepare 3 sample slices, 2 surface slices and 1 bulk slice.

The following notation has been applied for labelling the finally prepared sample slices, described using the example of sample 4.1ia1. This sample slice has been prepared out of the native pipe sample 4.1. "i" is the first stripe, cut out from the pipe wall, while "a" stands for the first cuboid, separated from stripe 4.1i. The digit "1" at the end stands for the outer surface slice of the cuboid 4.1ia.

4.2. Experimental setup

X-ray diffraction and Small Angle X-Ray Scattering experiments for structure determination of PE material grade PE63 took place at three different experimental stations: the beamline BL9 at the synchrotron radiation source DELTA [58], at a laboratory x-ray source at the University of Helsinki, Finland, as well as at the beamline BW5 at Hasylab/DESY in Hamburg. The various experimental stations, setups and measuring programs will be discussed in the subsequent sections.

4.2.1. Beamline BL9 at DELTA: Small and wide angle x-ray scattering

A super conducting asymmetric wiggler is the x-ray source for beamline BL9 at DELTA [59]. The white beam is monochromatisized by a Si[311] double monochromator crystal within a wavelength range of 4 and 30 keV. The energy resolution is $\Delta E/E \sim 10^{-4}$. A slit system defines a beam size between $1.5{\times}4$ mm^2 and $0.5{\times}0.1$mm^2 at the sample stage. A fast-shutter system at the entrance of the experimental hutch protects the sample as well as the detector from unintentional exposure. A two-dimensional image plate MAR345 detector [5] is used for data acquisition.

The setup, in principle used for both types of experiments of the beamline BL9 is presented in figure 4.3.

The setup for XRD and SAXS experiments differs only in a few points:

1. used sample cell,
2. distance between sample and detector
3. bypassing of the air gap between sample and detector in the SAXS experiments,
4. used photon energy.

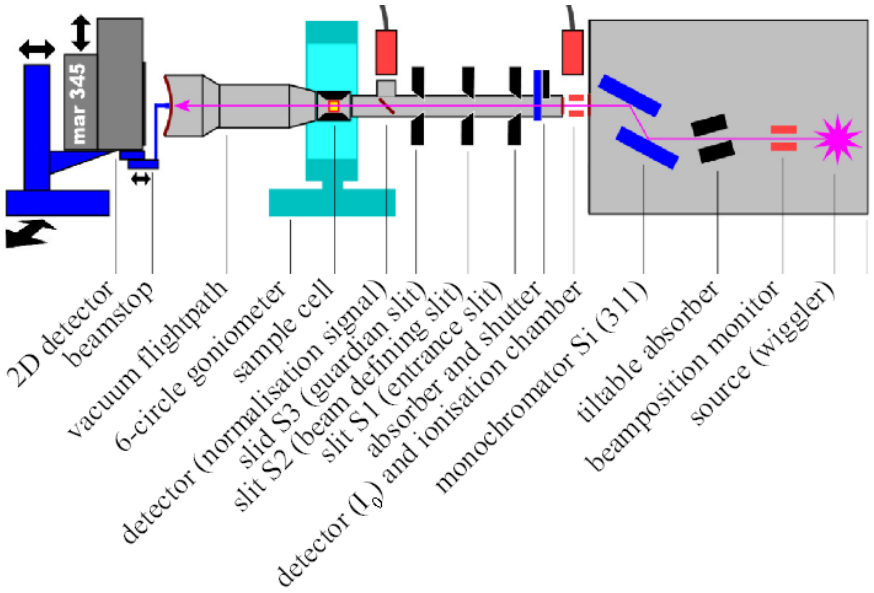

Fig. 4.3.: Schematic overview of beamline BL9 of DELTA.

The small angle x-ray scattering setup

The SAXS experiments have been carried out with a sample cell, which has been constructed during the PhD thesis of C. Krywka [57, 60], extended by a special sample holder. The sample cell is directly connected to an evacuated flightpath with a diameter of 20 cm and a length of ∼110 cm to avoid air scattering. There is only a small gap between the Kapton foil of the flightpath and the surface of the MAR345 image plate detector [59]. This flightpath is used to avoid air scattering. The scattering setup enabled an accessible q range between 0 and 0.8 Å^{-1}.

During the performed SAXS experiments a detector pixel size of $100 \times 100\,\mu m^2$ was selected with a detector diameter of 34.5 cm. The distance d is with 1.08 m relatively large due to the necessity to separate closely occurring scattering signals. A 1 mm thick beamstop protects the image plate detector from over exposure by the direct beam.

SAXS spectra were calibrated by measuring the well-known diffraction pattern of silver behenate [44]. With this information it was possible to extract the one-dimensional small angle scattering spectra of the PE samples.

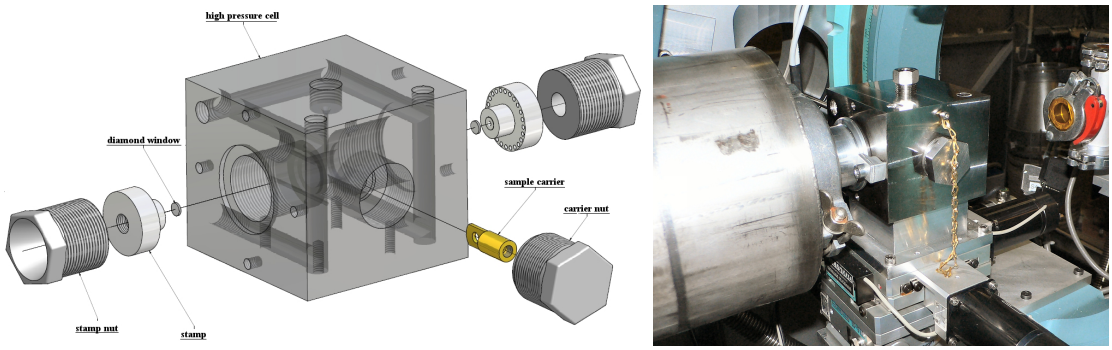

(a) (b)

Fig. 4.4.: Pictures of the SAXS cell [57]. A conical flightpath can be attached (see fig. (b)) in order to avoid air scattering.

Sample cell for SAXS experiments

For the SAXS experiments a sample cell for high pressure and temperature measurements was used [57]. The cell is depicted in figure 4.4. The massive cubic cell made of Inconel 718 possesses openings for entrance and exit windows fixed at a sealing nut, pressure supply, temperature control, and an opening for the sample holder. For experiments with normal pressure it is possible to utilise Kapton windows instead of diamond windows. In order to reduce air scattering, a conical flightpath is attached to the sample cell. The sample is fixed in a sample holder with a diameter of 10 mm and placed in the cell through the corresponding opening at the front.

SAXS measurements

The sample slices were irradiated with 10 keV radiation ($\lambda = 1.238\,\text{Å}$). With the abovementioned distance of 1.08 m and an active detector area of $\varnothing = 34.5$ cm a q-range of 0 to 0.81 Å^{-1} was accessible, which corresponds to a scattering angle range of $\sim 18.4\,°$.

Preliminary short data acquisition was applied in order to check the flux onto the detector. Following these results, acquisition times adapted to the flux were determined. In order to conduct a background correction, images without samples were taken. Three scans were accomplished for each sample slice, so that an averaging over 3 values for every quantity was possible.

The wide angle x-ray diffraction setup

In contrast to SAXS experiments a smaller distance between sample and detector is required for diffraction experiments. Due to the stronger scattering signal no flightpath is needed. For that reason a detector distance d of 35 and 40 cm was selected in different experiments, which allows a large covering in the reciprocal space.

An aluminium rod with a 2.5 mm thick and 5 mm deep slit was used as sample holder. The sample slices were fixed in this slit by a M2 slug. This kind of sample attachment allows a fast sample exchange. After fixing the sample holder into the goniometer head of the diffractometer, data acquisition took place.

Diffraction measurements

Two types of experiments have been accomplished in this setup: XRD measurements as a function of the position within the pipe wall and ex-situ annealing experiments. In the first case after sample exchange varying numbers of succeeding scans have been accomplished for each sample slice. An x-ray energy of 27 keV ($\lambda = 0.459\,\text{Å}$) was used and enabled an accessible q-range of $6\,\text{Å}^{-1}$.

Ex-situ annealing

Elevated temperatures have been applied to selected native samples slices, which have already been examined in their native state before. The annealing took place in an oven at temperatures between 70 and 140 °C for a period of 15 minutes each. After heating, the slices could cool down to room temperature. Subsequently the measurements took place and the next temperature step was taken.

4.2.2. The experimental station BW5 at Hasylab/DESY: Diffraction experiments

The beamline BW5 at Hasylab/DESY is a high energy diffraction beamline for energies between 60 and 150 keV [6]. The used photon energy in this experiment was 70 keV ($\lambda = 0.177$ Å). This ensured a sufficient q space covering at the detector of 6.5 $Å^{-1}$. The experimental station is equipped with a MAR345 image plate detector for the recording of the two-dimensional scattering patterns.

After passing beam defining slits the beam hits an aluminium foil. The scattered radiation of the foil is detected by a sodium iodide scintillation detector in order to measure the incoming intensity. Afterwards the beam intensity can be controlled by the help of an absorber system. The scattered intensity hits the MAR detector, which was located in a distance of 99.64 cm behind the sample. Its centre is protected by an active beamstop, measuring the remaining intensity of the transmitted beam.

The sample cell was attached to a movable sample stage, which allows a horizontal translation. For temperature regulation a LakeShore340 temperature controller was used.

4.2.3. Sample cell for in-situ temperature dependent experiments

In-situ temperature dependent experiments require an accordingly equipped sample cell. Such a sample cell was developed in the diploma thesis of M. Krämer [54].

The sample cell is of cylindrical shape ($Ø = 20$ cm) with two opposite Kapton windows and a height of 8 cm from the bottom plate to the upper rim. It is fixed to a base plate with a diameter of 28 cm in order to attach it to a goniometer head of a diffractometer.

A circular ceramic block is attached to this base plate for thermal insulation. Two 1 cm broad immersions have been milled into this block to accommodate an 100 Ω resistance in each case. Furthermore the cell is equipped with two Pt100 temperature sensors. One is attached to the heating block, the other is suspended in air in order to measure the temperatures of the heating resistances and the surrounding medium. The

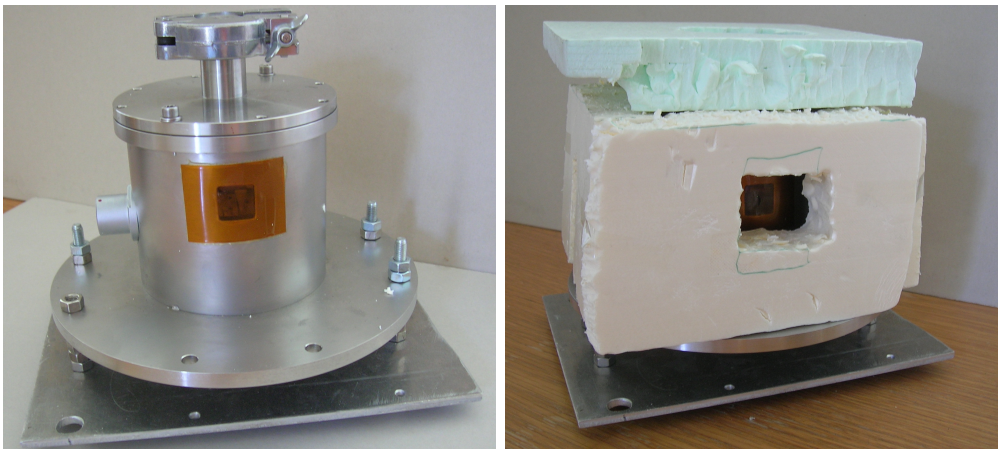

(a) Not thermally isolated heating cell. (b) Thermally isolated heating cell.

Fig. 4.5.: Picture of the heating cell. It consists of a hollow cylinder cupped by a circular plate equipped with a sheath to introduce the sample (holder). For heating the cell is equipped with two 100 Ω resistances, parallel interconnected. The temperature is measured by two Pt100 temperature sensors.

measurement of the air temperature instead of the actual sample temperature requires a temperature calibration. It is described in section 4.2.4.

The chamber is closed by a circular plate that is equipped with a barrel sheath of 0.5 cm height. This opening is used to introduce the sample holder into the chamber volume. The cell is filled with air as thermoconductive medium.

The heating resistances and the two sensors are connected to a LakeShore 440/430 in order to control the temperature in the sample cell. The sample cell is depicted in figure 4.5. In order to ensure a good thermal stability and isolation, a polystyrene shell is fixed around the cell, as can be seen in 4.5(b).

In-situ annealing and data acquisition

In order to conduct in-situ annealing experiments, the temperature cell described in section 4.2.3 was fixed in the diffractometer. During the annealing procedure, 2D scattering images were acquired for ambient temperature, 30 °C, 50 °C, and 70 °C immediately after reaching the temperature and 15 minutes later. In the following, the sample was annealed in a ramp up to a temperature of 100 °C. During this ramp,

consecutive 2D images were acquired. Only the last sample slice R3E4 was annealed in temperature steps of 40 °C, and 70 °C. Subsequently the heating ramp started.

4.2.4. Temperature calibration

During the in-situ experiments the temperature within the sample cell was controlled by the air temperature. The relationship between heater and air temperature was used for calculating the sample temperature. Image 4.6 depicts sample temperatures T_{sample} calculated from heater temperatures T_{heater}.

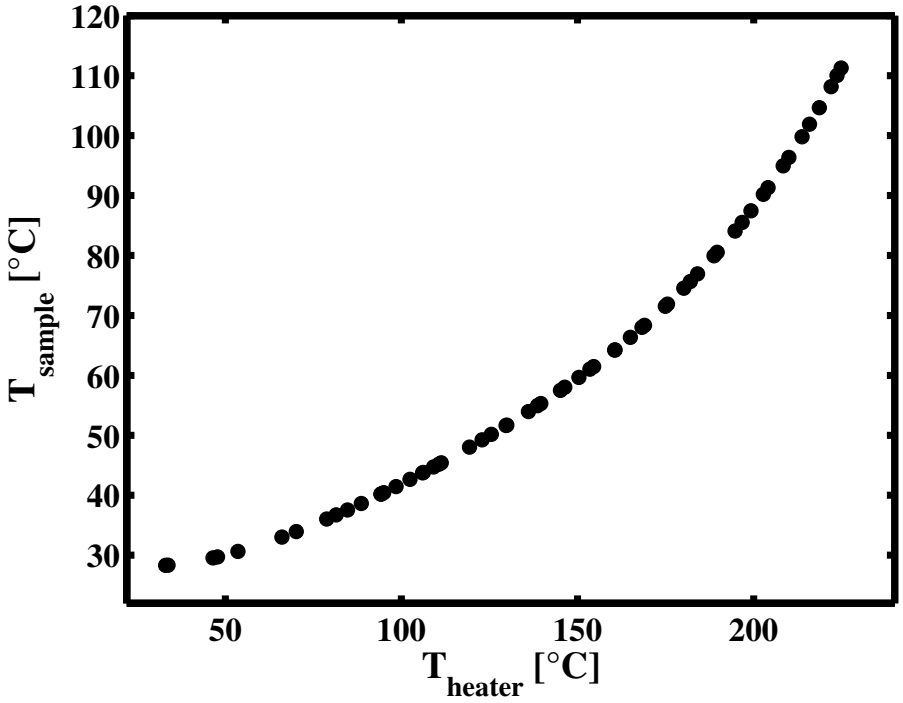

Fig. 4.6.: Relationship between heater and sample temperature.

(a)

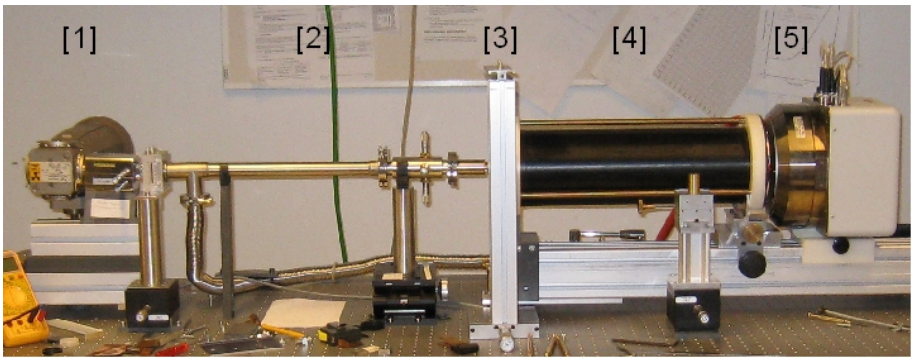

(b)

Fig. 4.7.: (a) Sample holder and (b) SAXS setup at the laboratory x-ray source in Helsinki with source [1], flightpath before sample [2], sample holder with sample [3], flightpath [4] and area detector [5].

4.2.5. Laboratory x-ray source at the University of Helsinki, Finland: space dependent SAXS experiments

A laboratory x-ray source with a small angle scattering setup could be utilised in the faculty of physics of the University of Helsinki, Finland, department material physics. A Cu target generates an x-ray beam with a wavelength of 1.54 Å and corresponding energy of 8.048 keV. A flightpath is attached to the source to reduce parasitical scattering. After passing the flightpath the x-ray beam hits the sample in transmission geometry. Another flightpath was placed between sample and a Bruker AXS HI-STAR area detector system with a spatial resolution of 200 µm [7], in which the 2-dimensional signal is detected. The detector owns a sensitive area of diameter of 11.5 cm. The distance between sample and detector amounted to 48.35 cm. The scattering patterns, recorded by this detector, had a resolution of 512×512 pixels. A beamstop, consisting of a semitransparent material, lets a part of the beam pass. Thus it is possible to measure a normalisation signal. The setup is depicted in fig. 4.7(b).

SAXS measurements

In order to acquire SAXS spectra, the sample slice was fixed in the sample holder depicted in fig. 4.7(a). Afterwards, the sample holder itself was fixed into a support rail. Preliminary short data acquisition took place in order to check the flux onto the detector. Following these results, an acquisition time of 300 s was determined. In order to conduct a background correction, images without samples were taken.

5. Results

5.1. X-ray diffraction measurements

5.1.1. Qualitative analysis of diffraction data

At the first glance a qualitative inspection of two-dimensional scattering patterns of PE reveals an inhomogeneous intensity distribution in some of the diffraction rings, as can be seen in fig. 5.1(a). Obviously the origin of this texture denominated phenomenon

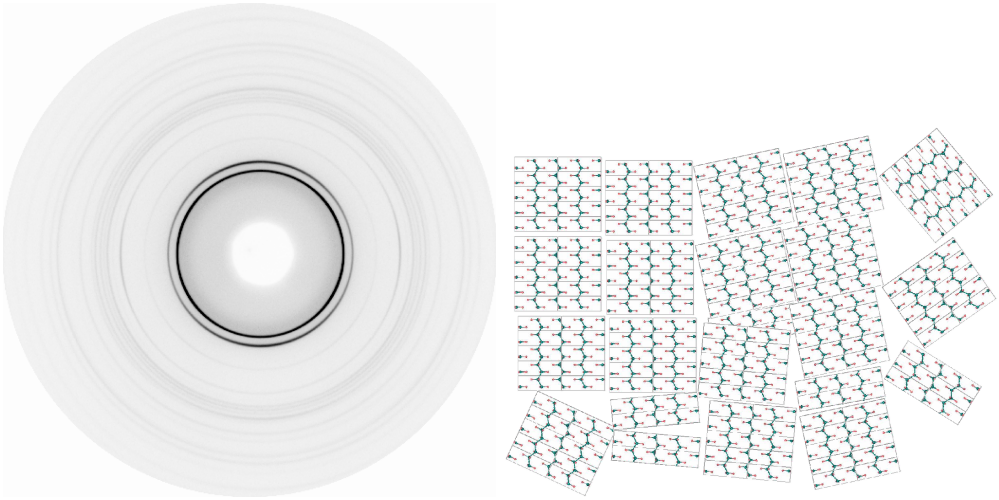

(a) (b)

Fig. 5.1.: (a) Exemplary two-dimensional diffraction pattern for a surface slice of PE. Some diffraction rings show arcs of higher intensity and areas with lower intensity. This phenomenon is called texture. (b) Schematic representation of partially oriented PE crystallites in a polycrystalline sample.

is a preferred orientation of crystallites in the polycrystalline material. In that case, a relatively large amount of crystallites is oriented more or less parallel to each other, giving rise for the inhomogeneously intensity distribution. A smaller number of crystallites

still has a random orientation, which results in weaker illuminated ring areas due to a smaller number of contributing lattice planes. This partial orientation of crystallites is illustrated in fig. 5.1(b).

In section 3.3 an example for a one-dimensional scattering pattern of PE with indexes was shown. Referring to this list of indices, the Debye-Scherrer rings of inhomogeneous intensity can be identified as shown in the following image (fig. 5.2(a)).

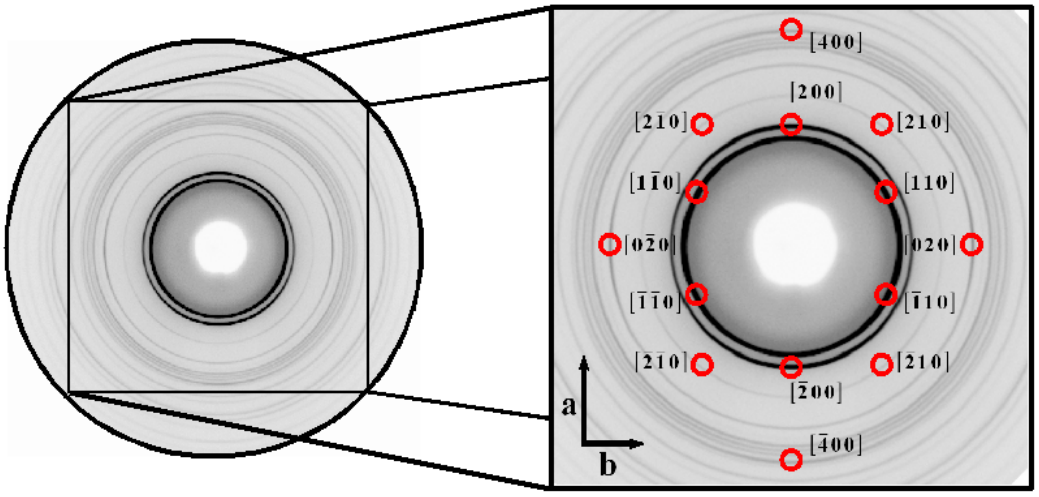

(a)

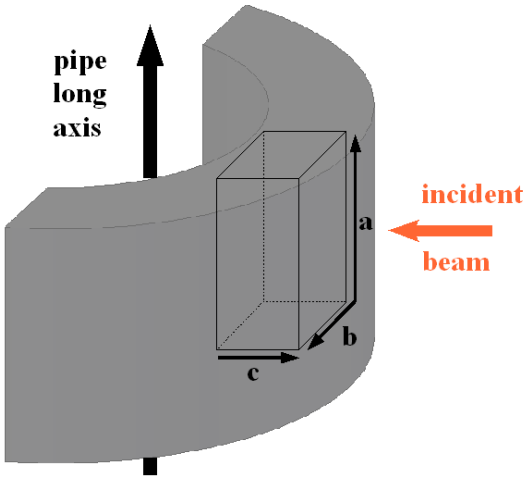

(b)

Fig. 5.2.: (a) Diffraction pattern of a PE pipe sample. The intensity maxima of the corresponding reflections are indexed for an orientation of a in the vertical plane, b in the horizontal plane and c in beam direction. (b) Preferred orientation of the PE unit cell with respect to the incoming beam of the pipe samples as deduced from the texture of the diffraction patterns.

The maxima of the corresponding diffraction rings are indicated, indexed and refer to the preferred orientation of crystallites as shown in fig. 5.2(b)). The a-axis is oriented preferentially alongside the long axis of the pipe. The b-axis indicates a tangential direction (i.e., parallel to the wall surface), while the c-axis points in the radial direction perpendicular to the plane defined by a and b, which is also the direction of the incident beam.

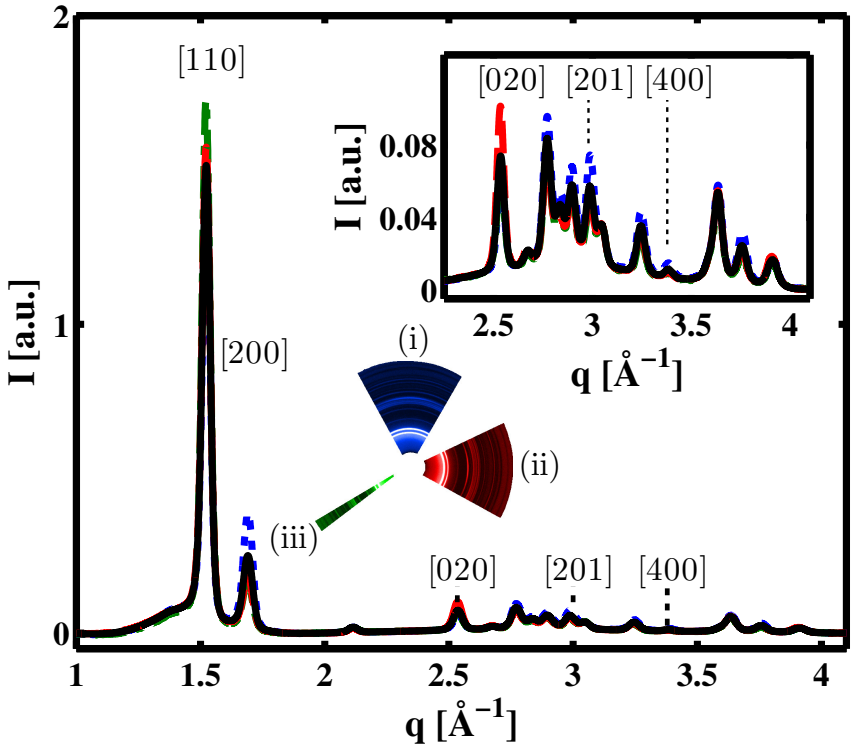

Fig. 5.3.: Texture comparison for a native surface slice between (i) {100} direction (▪▪▪), (ii) {010} (▬ ▬), (iii) {110} direction (▬ ▪ ▬) and full integration (▬). Inset: Integration masks for the pie integrations.

To discuss the texture for different samples pie integrations have been conducted in (i) the vertical plane ({100} direction), (ii) the horizontal plane ({010} direction) and (iii) at an angle of 33.70 ° with respect to the horizontal plane for the $\{\overline{1}10\}$ direction, as visualised in the inset of fig. 5.3. Exemplarily, the result of these integrations for a native surface slice showing texture is depicted in fig. 5.3 and compared to the full integration.

In the following discussion, the focus is set on the intense [110] and [200] reflection.

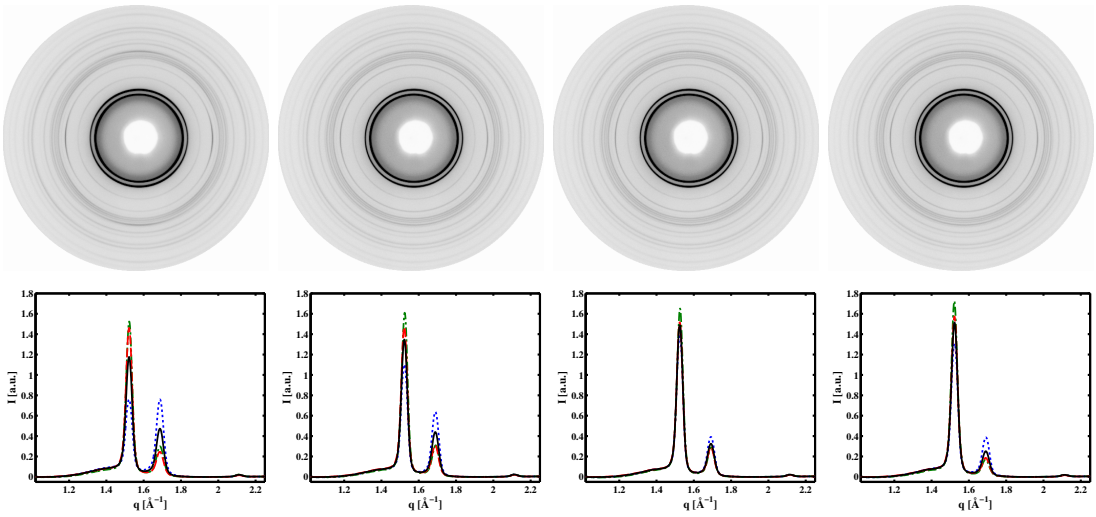

(a) (b) (c) (d)

Fig. 5.4.: 2D and 1D diffraction patterns for a native pipe sample for (a) outer surface, (b) first and (c) second bulk and (d) inner surface slice comparing (i) {100} direction (▪ ▪ ▪), (ii) {010} (▬ ▬), (iii) {$\overline{1}$10} direction (▬ ▪ ▬) and full integration (▬).

In order to analyse, if the texture changes with respect to the investigated position of material in the pipe wall, two-dimensional scattering images over the entire pipe profile are compared. The images are depicted in the first row of fig. 5.4. The left image shows the 2D spectrum for the native outer surface slice. The two bulk slices are represented by the two images 5.4(b) and 5.4(c). The pipe wall is completed by the inner surface slice R3D4, whose 2D scattering pattern is shown in figure 5.4(d).

Both surface slices show a strong texture, while the texture is less pronounced for the two bulk slices. While the first bulk slice shows a reduced texture, almost no texture can be observed for the second bulk slice in fig. 5.4(c). The spatial orientation might originate from the manufacturing technique, as will be discussed later. These varying textures in the cross-section of the pipe wall should be pronounced with the comparison of the individually integrated patterns in {100}, {010}, and {$\overline{1}$10} direction with the full integration, as depicted in the bottom row of fig. 5.4. The full integration is marked by a solid line, the integration in the vertical plane by a dotted, the {$\overline{1}$10} direction as dash-dotted, and the integration in vertical direction by a dashed line.

At the outer surface, both reflections show a strong texture. Whereas the intensity of the [110] reflection is the more intense in the horizontal direction and weaker in

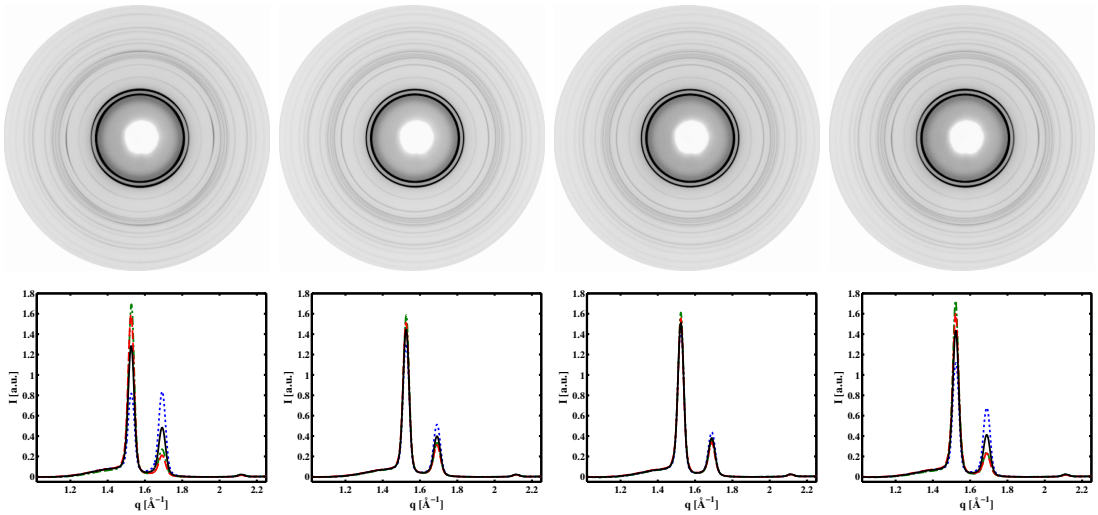

Fig. 5.5.: 2D and 1D diffraction patterns for an aged pipe sample for (a) outer surface, (b) first and (c) second bulk and (d) inner surface slice comparing (i) {100} direction (▪ ▪ ▪), (ii) {010} (▬ ▬), (iii) {$\overline{1}$10} direction (▬ ▪ ▬) and full integration (▬).

vertical direction, the intensity distribution of the [200] reflection behaves just vice versa. The [110] reflection shows the highest intensity in {$\overline{1}$10} and equivalent directions and correspondingly the [200] reflection in {100} direction. Both reflections show an inhomogeneous intensity distribution for the first bulk slice, whereas the texture is stronger pronounced for the [200] reflection. Nearly no texture could be recognised for both reflections for the second bulk slice. At the inner surface, a texture can be observed again.

A strong texture at the outer surface can be observed for all pipe samples. Both bulk slices and the inner surface slice of all examined native slices show a considerably lower texture. In contrast, a strong texture can be observed at the inner surface of aged samples.

In the following, the effect of ageing onto the texture should be examined. In accordance to the analysis for the native sample presented above, the four images in fig. 5.5 show on the left and right hand the 2D scattering patterns for the outer (fig. 5.5(a)) and the inner surface slice (fig. 5.5(d)) for the aged sample R2D. Again, the figures (c) and (d) display scattering patterns for the corresponding bulk slices.

In this case, the outer surface slice shows a rather strong texture comparable to the corresponding native slice. While the texture is rather weakly pronounced regarding the first bulk slice, the texture is enhanced for the second bulk slice. At the inner surface, the intensity of [200] reflection is strongly pronounced in {100} integration direction and considerably lower in {010} and $\{\overline{1}10\}$ direction. The aged inner surface slice finally shows the strongest texture with respect to the [200] reflection and especially compared to the native inner surface slice. The texture of the [110] reflection has also enhanced with respect to the other slices.

5.1.2. Quantitative analysis of diffraction data

Since the structure of PE is well understood [25] with respect to lattice parameters and atom positions within the unit cell, a complete structure determination is not necessary. The analysis is thus essentially confined to the determination of lattice parameters and the evaluation of integral peak intensities for the calculation of relative crystallinities. These quantities can be determined focusing on a q range between 1.02 and 2.25 Å^{-1}. In this range the [110], [200] and [210] reflections are located together with a broad amorphous scattering contribution. Focusing on these Bragg reflections information on lattice constants a and b are obtained. Investigations of the lattice constant c are not discussed, since former experiments by Bunn and Alcock [24] and Davis *et al.* [29] showed that even in annealing experiments no modification of the C-C bonding length and thus the lattice constant c (double bonding length) takes place.

The data analysis is divided into several steps and exemplarily presented in all steps by the sample R3D1. The data acquisition with an image plate detector yields a two-dimensional scattering pattern. In order to deduce structural parameters, the pattern must be transferred into a one-dimensional intensity distribution. The integration is performed by the Fit2D software [8] with apparatus parameters presented in tab. 5.1.

In the next step the background correction is conducted. After a normalisation to the integral intensity a Pearson function is fitted to the 1D pattern and then subtracted. Subsequently the background corrected scan is normalised to the integral scattering signal between 1 and $2\,\text{Å}^{-1}$. The decomposition of the signal into Bragg peaks and an amorphous portion is done in the next step and in good accordance to

parameter	value
energy [keV]	27
λ [Å]	0.459
pixel size [μm^2]	100×100
sample-detector distance [mm]	352.524
beam centre x_0 & y_0 [px]	1227.618 & 1198.606
rotation angle °	-53.099
tilt angle °	-0.082

Tab. 5.1.: Exemplary parameters for the integration of two-dimensional scattering data of sample R3D1.

[88, 56, 72, 74, 49, 16], as can be seen in fig. 5.6. Exemplarily, a background correction for a one-dimensional diffraction pattern of PE is shown in fig. 5.7(a). The expected orthorhombic crystal structure could be confirmed by comparison of the data with the theoretical scattering pattern shown in sec. 3.3.

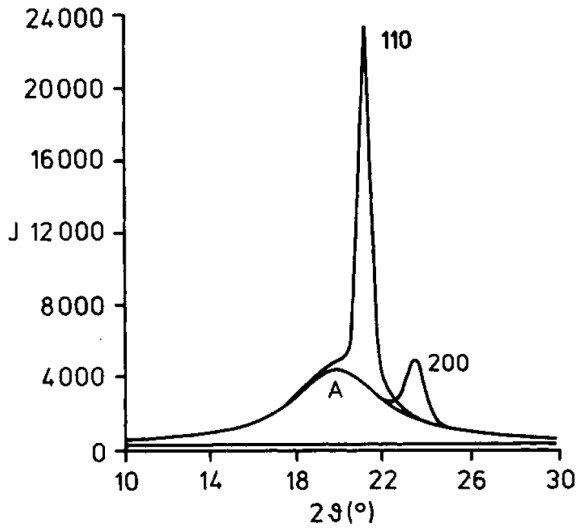

Fig. 5.6.: One-dimensional diffraction pattern of a polyethylene sample with decomposition in amorphous and crystalline contributions as discussed in [72].

The parameters of interest are crystallinity, crystallite sizes and lattice constants. The latter is particularly important for temperature dependent measurements. This information can be obtained by analysing the positions of the scattering peaks. The decomposition of the intensity is performed by a combination of three Voigt profiles to model the Bragg reflections and a single Gaussian profile to account for the amorphous

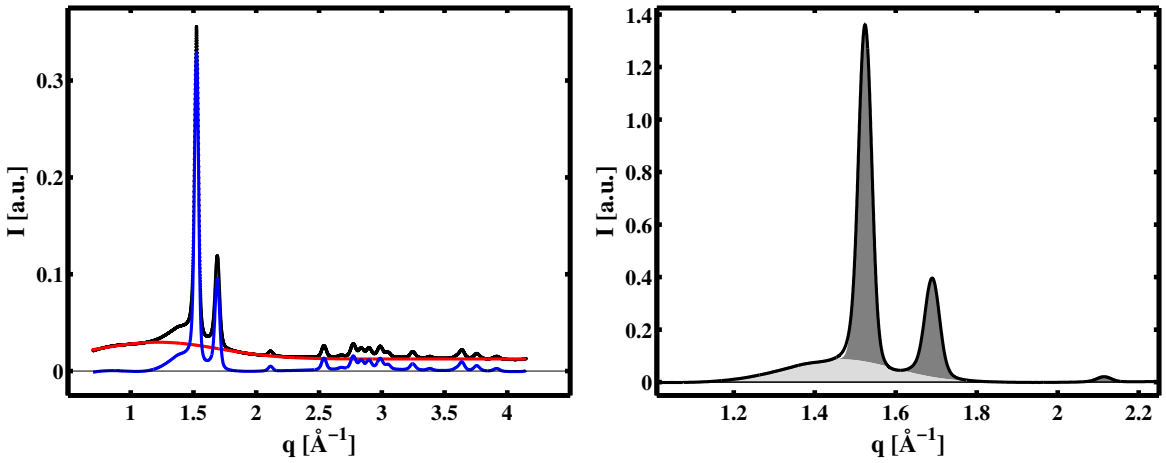

(a) (b)

Fig. 5.7.: (a) Background correction for XRD data with experimental data (▬), background (▬), and background corrected data (▬). (b) Exemplary profile fit with data (▬), light grey: amorphous scattering contribution (▬), and crystalline contribution (▬).

scattering contribution, denominated as I_{cr} and I_{am}, that were fitted to the experimental data. The result of this fit is shown in figure 5.7(b). For this example peak positions of Bragg peaks in this decomposition are $q_{110} = 1.52\,\text{Å}^{-1}$ for the [110] reflection, $q_{200} = 1.69\,\text{Å}^{-1}$ for the [200] reflection and $q_{210} = 2.11\,\text{Å}^{-1}$ for the [210] reflection. The distance between parallel lattice planes indexed by the Miller indices hkl are calculated by $d_{hkl} = \frac{2\pi}{q_{hkl}}$ (section 3.2.3) and the lattice constants follow from the general expression

$$d_{hkl} = \frac{1}{\sqrt{\left(\frac{h}{a}\right)^2 + \left(\frac{k}{b}\right)^2 + \left(\frac{l}{c}\right)^2}}, \tag{5.1}$$

Also using geometrical considerations, lattice constant a could be determined to 7.44 Å, while lattice constant b amounts to 4.96 Å. This is in good accordance to results found by Bunn and Alcock ($a = 7.42\,$Å, $b = 4.93\,$Å, [24]), Caminiti *et al.* ($a = 7.4241\,$Å, $b = 4.9491\,$Å, [28]), Swan ($a = 7.414\,$Å, $b = 4.942\,$Å, [83])

The maximum of the amorphous contribution to the scattering signal is located at $1.47\,\text{Å}^{-1}$. The amorphous and crystalline contributions I_{am} and I_{cr} of the total scattering intensity I_{tot} in this q range are the integral intensities of the corresponding scattering contributions, obtained in the step before. Crystallite sizes are calculated

using reflection positions and half width maxima as real space values with the Scherrer formula [39, 74]

$$D_{hkl}^{1/2} = \frac{K\lambda}{L_{hkl}\cos\theta_{hkl}}. \tag{5.2}$$

For cubic crystal systems the factor K amounts to 0.94 [9]. The corresponding full width half maxima D_{hkl} of the profiles are $D_{110} = 0.040\,\text{Å}^{-1}$, $D_{200} = 0.048\,\text{Å}^{-1}$ and $D_{110} = 0.051\,\text{Å}^{-1}$. Thus for the crystallite sizes follow these values: $L_{110} = 149.63\,\text{Å}$, $L_{200} = 124.50\,\text{Å}$, and $L_{210} = 117.39\,\text{Å}$. These crystallite sizes are in good accordance to Walenta *et al.* [91], who examined the structure of PE foils, but a bit underestimated with respect to all examined pipes except pipe R2.

For further analysis and comparison of results of different samples averaged values of all conducted scans for each sample for crystallite sizes, amorphous and crystalline ratios and lattice constants with corresponding errors are calculated. The averaging is conducted over all scans carried out for the corresponding sample slice. To calculate the sample's crystallinity, the following equation is used:

$$\chi_C = \frac{\overline{I}_{cr}}{\overline{I}_{tot}}, \qquad \text{with} \qquad \overline{I}_{tot} = \overline{I}_{am} + \overline{I}_{cr}, \tag{5.3}$$

with the average intensities $\overline{I}_{cr}$ and $\overline{I}_{am}$ of the determined crystalline and amorphous scattering contributions of each scan. For this sample, the crystallinity amounts to 67.4 %.

Averaged values for positions of the Bragg peaks, full width half maxima and corresponding crystallite sizes for the sample slice R3D1 can be found in tab. 5.2. The

hkl	$2\theta_{hkl}$ [°]	D_{hkl} [°]	q [Å^{-1}]	D_{hkl} [Å^{-1}]	L_{hkl} [Å]
110	6.37	0.17	1.52	0.040	149.75 ± 0.27
200	7.07	0.20	1.69	0.048	124.25 ± 0.06
210	8.85	0.21	2.11	0.051	116.60 ± 0.92

Tab. 5.2.: Averaged values for crystallinity, full width half maxima and corresponding crystallite sizes of sample R3D1.

deduced lattice constants amount to $a = 7.45\,\text{Å}$ and $b = 4.96\,\text{Å}$. The values of χ are determined with high uncertainty, but relative changes of the crystallinity can be deduced with high accuracy.

In the following the results of x-ray diffraction experiments performed at beamline BL9 at DELTA and beamline BW5 at Hasylab will be presented.

5.1.3. Results of position dependent XRD experiments

In order to investigate possible precursors for material abrasion in PE gas pipes, x-ray diffraction experiments of various samples at different experimental stations have been conducted.

Native pipe sample R3 and aged pipe sample R2

The native sample R3 was prepared as described in section 4.1.4 and the experiments took place as presented in section 4.2.1. The data analysis was carried out as discussed before. The results for crystallinity χ and crystallite sizes L_{hkl} as a function of the sample slice are obtained for all cuboids and depicted as circular markers in fig. 5.8(a). The average values are shown as black diamonds. As mentioned in section 4.1.4, slice 1 is the outer surface slice. Thus, the chart shows a cross-section of the crystallinity over the entire pipe wall from the outer wall on the left hand over two bulk slices in the middle (slices 2 and 3) and the inner surface slice 4 on the right side.

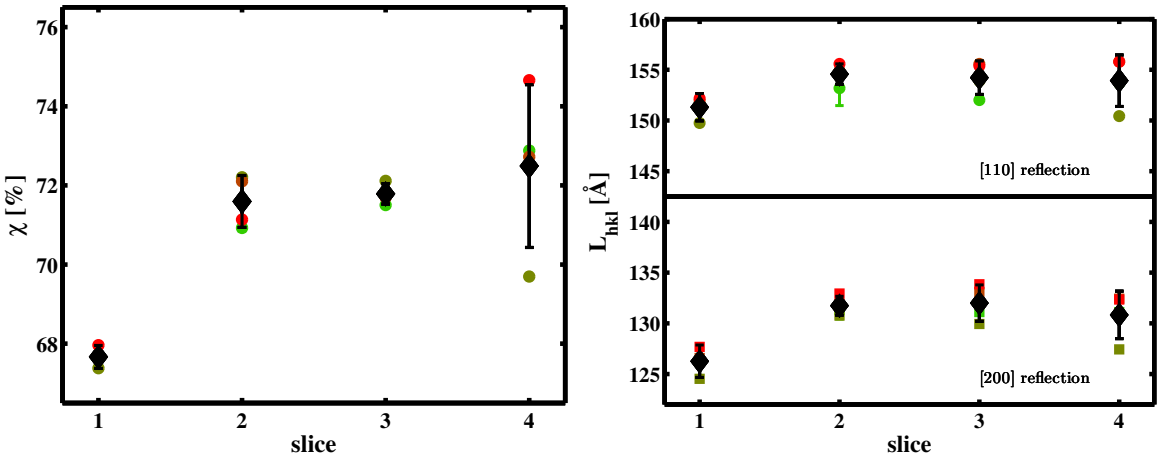

(a) (b)

Fig. 5.8.: (a) Individual and averaged crystallinities χ and (b) crystallite sizes L_{hkl} determined by x-ray diffraction for the native pipe R3 as a function of the sample slice. Averaged values represented by ♦.

The lowest amount of crystalline material can be found at the outer surface of pipe R3. With transition to the bulk, the crystallinity is considerably enlarged and rather constant for slices 2 and 3 and also for the inner surface. The crystallite sizes L_{hkl}, depicted in fig. 5.8(b), show a rather constant behaviour with only slightly varying crystallite sizes over the entire pipe wall in {110} direction as well as in {200} direction with minimum size at the outer surface for both directions.

The crystallite sizes presented in figures 5.8(b) and 5.9(b) are considerably lower than the crystallite sizes deduced for the other examined samples, as will be shown later.

The results of the aged pipe sample R2 show a similar behaviour as the corresponding values of the native sample R3. The results for crystallinity and crystallite sizes are depicted in fig. 5.9. It amounts to a value of $70.5 \pm 0.5\,\%$ and increases to a value of $74.3 \pm 0.2\,\%$ at the outer surface. The crystallinity difference between outer and inner surface thus amounts to $\sim 4\,\%$.

The crystallite sizes in {110} and {200} direction are rather constant as found for the native pipes, though especially L_{200} shows a slight minimum for the outer surface slice.

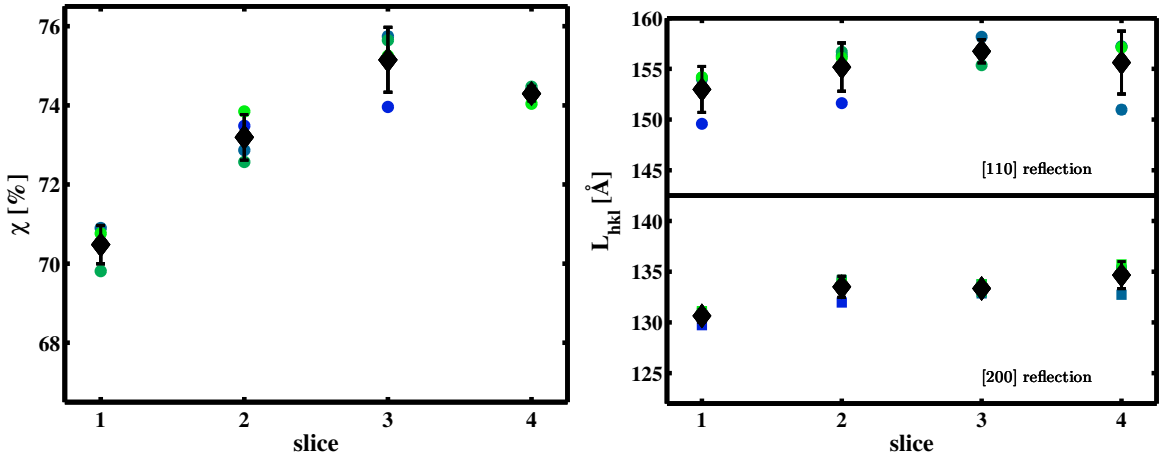

(a) (b)

Fig. 5.9.: (a) Individual and averaged crystallinities χ and (b) crystallite sizes L_{hkl} determined by x-ray diffraction for the aged pipe R2 as a function of the sample slice. Averaged values represented by ⧫.

Fig. 5.10 shows the comparison between the deduced crystallinities for the native sample R3 as blue circles and for the aged sample R2 as red squares. The development of

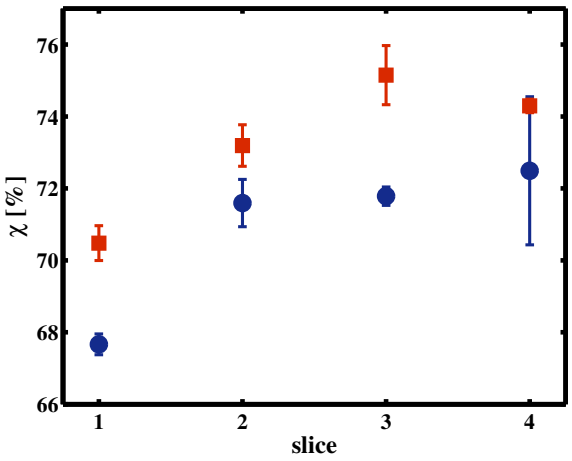

Fig. 5.10.: Comparison between crystallinities obtained for the native sample R3 (●) and the aged sample R2 (■) as a function of the sample slice.

χ over the cross-section of the pipe wall is in good accordance, whereas the crystallinity of the aged pipe R2 is slightly higher than the crystallinity of pipe R3.

Lattice constant a shows for all examined pipes lowest values for slice 1 and is thus in good agreement with the behaviour of χ. This is most significant for the {200} direction.

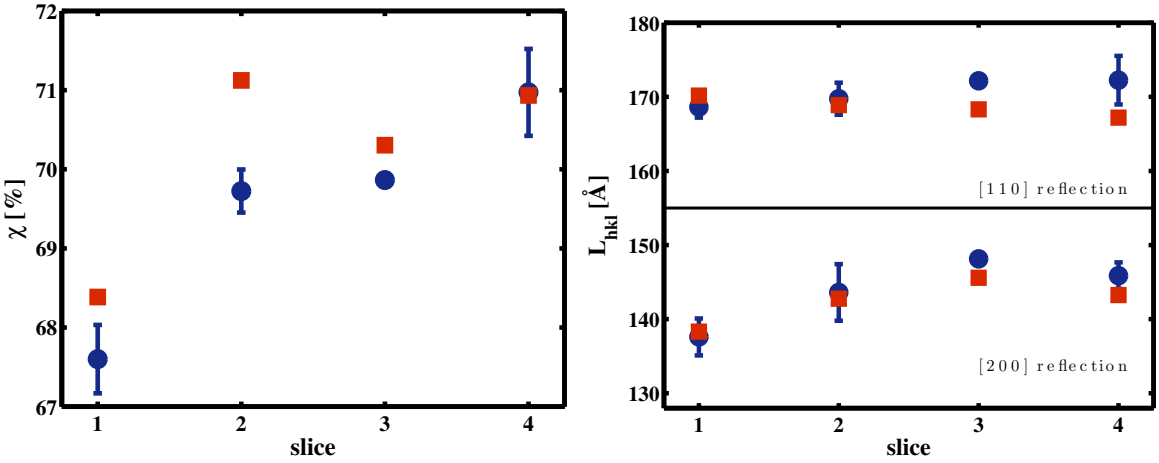

(a) (b)

Fig. 5.11.: Averaged (a) crystallinities χ and (b) crystallite sizes L_{hkl} of the native pipe sample r2.1i (●) and the aged sample r2.2i (■) as a function of the sample slice.

Pipe r2:

In the case of the pipe sample r2 two native cuboids have been examined, whereas one aged cuboid was investigated. Unfortunately sample slice r2.1ai3 turned out to be too thick to be fixed into the sample holder. Thus it is missed in the overview shown in fig. 5.11, which depicts the sample crystallinity χ and crystallite sizes L_{hkl} in {110} and {200} direction as a function of the sample slice and thus the position within the pipe wall. The χ and L_{hkl} values of both native cuboids are averaged for better statistics. Native sample slices are marked by blue circles, aged by red squares.

The crystallinity of the native sample depicted in fig. 5.11(a) shows the lowest contribution of crystalline material at the outer surface, which is rather strongly increasing in the transition to the inner surface slice, where the maximum can be observed. The lowest amount of crystalline material in the aged sample cuboid of pipe r2 can also be found at the outer surface. Afterwards, χ increases. In principle both crystallinities follow the same trend, but the crystallinities of the native sample are lower than the ones of the aged sample.

The corresponding crystallite sizes L_{hkl} are depicted in fig. 5.11(b). The top row above the horizontal line shows the crystallite sizes in the {110} direction, while the bottom line presents the crystallite sizes in {200} direction. Colours and markers are

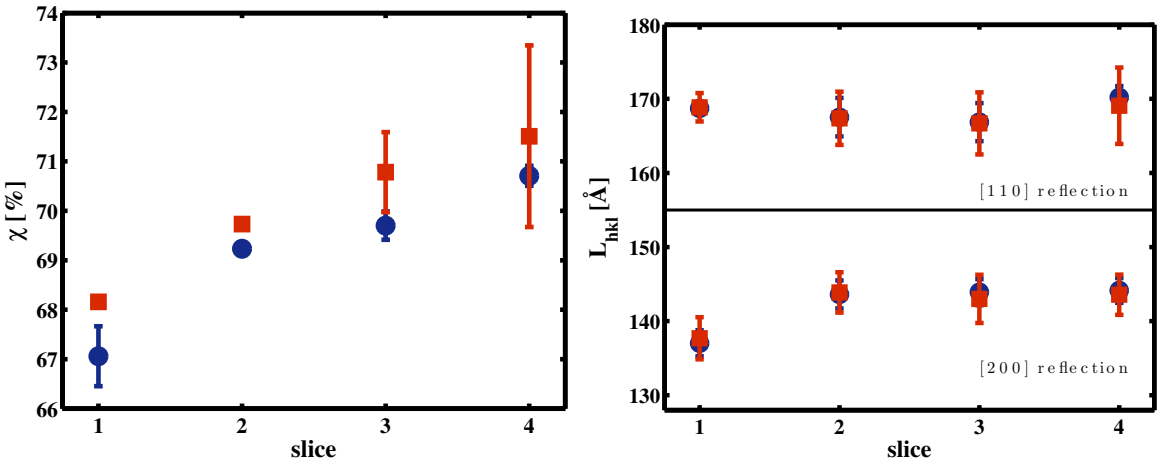

(a) (b)

Fig. 5.12.: Averaged (a) crystallinities χ and (b) crystallite sizes L_{hkl} of the native pipe sample r4.1i (●) and the aged sample r4.2i (■) as a function of the sample slice.

the same as in fig. (a). While L_{110} of the both samples shows only small deviations over the cross-section of the pipe wall, L_{200} is stronger varying. The smallest crystallite size in {200} direction can be again be observed at the outer surface.

Pipe r4:

For pipe r4 overall 4 cuboids could be prepared. The crystallinities of both native (blue circles) and both artificially aged samples (red squares) are averaged and depicted in fig. 5.12 as a function of the sample slice. Both samples possess the highest accumulation of crystalline material at the outer surface of the pipe wall. In the following transition to bulk and inner surface the crystallinity increases to its particular maximal value at the inner wall surface. Both crystallinities show the same trend, but the crystallinity of the aged sample seems to be slightly larger in the first two sample slices.

The crystallite sizes of the native and the aged sample do not considerably deviate from each other. The crystallite size L_{110} is only slightly varying, while L_{200} shows its minimum at the outer surface of the pipe wall.

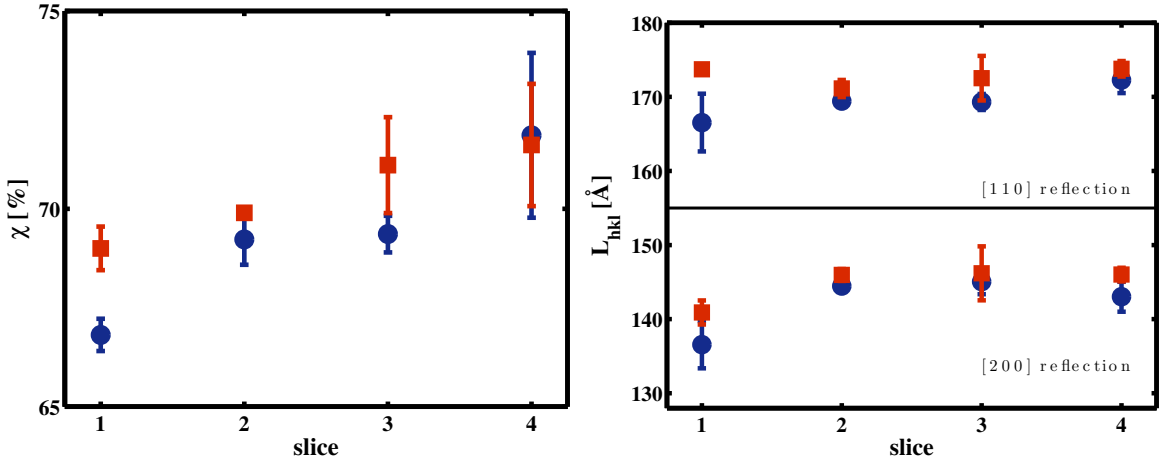

(a) (b)

Fig. 5.13.: Averaged (a) crystallinities χ and (b) crystallite sizes L_{hkl} of the native pipe sample r7.1i (●) and the aged sample r7.2i (■) as a function of the sample slice.

Pipe r7:

Two cuboids have been prepared for this pipe for both states. The crystallinities of the native and the aged cuboids, respectively, have again been averaged and are shown in fig. 5.13(a).

Both samples confirm the general trend of lowest crystallinities in the outermost surface slices, rising crystallinities in the bulk and maximum crystallinities at the inner surfaces. In accordance to pipe r2 and r4, the crystallinity of the aged sample is slightly larger than the crystallinity of the native sample for the first three slices and identical at the inner surface within the errors.

The crystallite sizes in {110} direction of the examined r7-sample cuboids are depicted in fig. 5.13(b). While L_{110} of both aged samples is rather constant over the entire pipe wall, L_{200} shows its maximum at the inner surface for the native and aged sample.

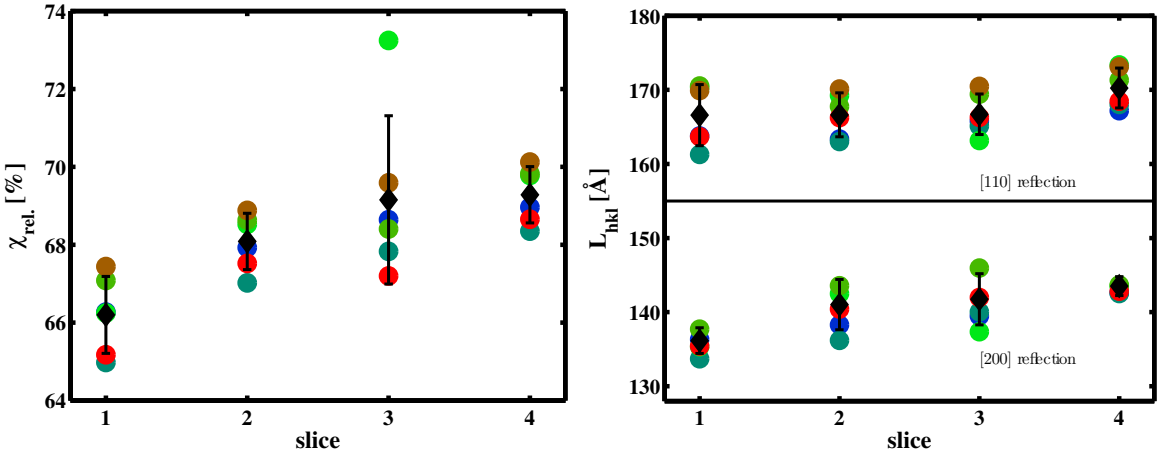

(a) (b)

Fig. 5.14.: Averaged and individual **??** crystallinities χ and crystallite sizes L_{hkl} for the pipe samples r3, r5, r6, r8, r9, and r11. **??** Crystallite sizes in {110} and {200} direction. Averaged values represented by ⧫.

Pipes r3, r5, r6, r8, r9, r10, and r11:

A series of native pipe samples was examined. The five pipe samples r3, r5, r6, r8, r9, and r11 with identical dimensions are presented and compared in this subsection. Furthermore, the single example for a pipe with a wall thickness of 5.1 mm (r10) is discussed at the end of the subsection. The crystallinities and crystallite sizes in {110} and {200} direction, respectively, are presented in fig. 5.14.

All crystallinities show a minimum at the outer surface and their maximum at the inner surface. The crystallinity value of slice r6.1ia3 is considered as anomaly. The crystallite sizes in {110} and {200} direction are shown in fig. **??**. While L_{110} shows in accordance to the pipes discussed before no large variations, the minimum of L_{200} can again be observed for the outer surface slice 1. The good accordance of the individual values should be emphasised by averaged values, represented by ⧫.

The crystallinity of pipe sample r10, depicted in fig. 5.15(a), is steadily increasing from outer surface over the bulk to the inner surface. The crystallite size in {110} direction is nearly constant over the entire cross-section of the pipe wall, while the crystallinity growth by assigned to the slightly growing crystallite size in {200} direction.

Thus it could finally be stated, that the behaviour of crystallinity and crystallite sizes is independent of the wall thickness.

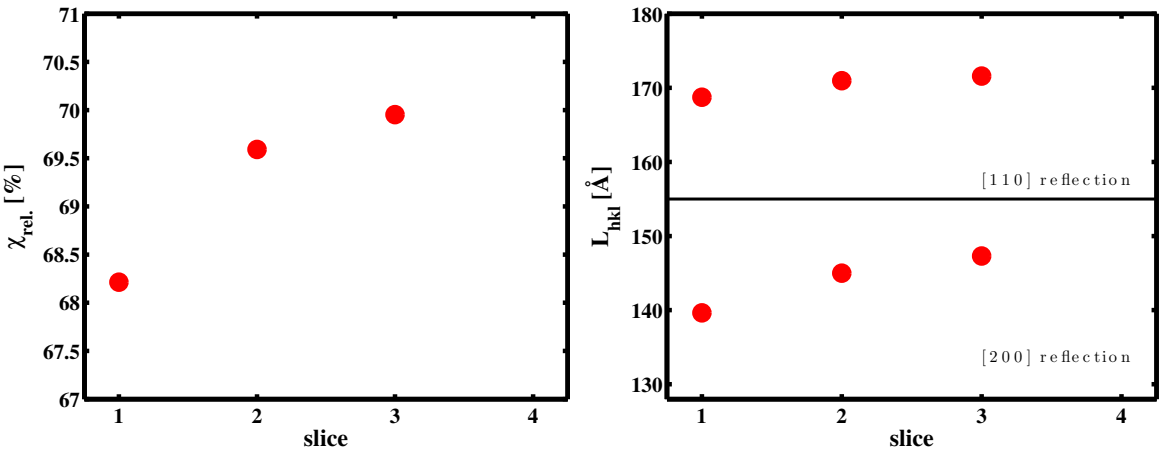

(a) (b)

Fig. 5.15.: (a) Crystallinities of the native pipe sample cuboid r10.1ia ( ) as a function of the sample slice. (b) Crystallite sizes in {110} and {200} direction.

Comparison between pipes with similar operating places

In the following, pipe samples with similar operating places will be compared. The crystallinities of the samples r3.1ia, r5.1ia, and r9.1ia, operated under streets, are illustrated in fig. 5.16(a). The curves show an almost perfect agreement in the trend with lowest amounts of crystalline material at the outer surface and steadily increasing crystallinity within the bulk and highest accumulation of crystallites at the inner surface. The crystallinity values only differ in their height, but are very similar in the slope of the curves. The difference in χ between outer and inner surface amounts for all regarded pipes to about 3 %. The similarity is pronounced by averaged values depicted in the figure, too.

The different crystallinity values of pipes operated under pavements are compared in fig. 5.16(b). Here the similar trend is less pronounced than in the case of pipes used under streets, though still existent. The crystallinities of the pipe samples r2.1i (averaged over both cuboids), r7.1ia (averaged over both cuboids), r8.1ia, and r11.1ia show the lowest amount of crystalline material at the outer surface, followed by a rather strong increase of χ to the first bulk slice. Afterwards, the crystallinity stays rather constant or is slightly decreasing, while the growth shows a similar slope with respect to the first increase in the last step to the inner surface. The crystallinity difference

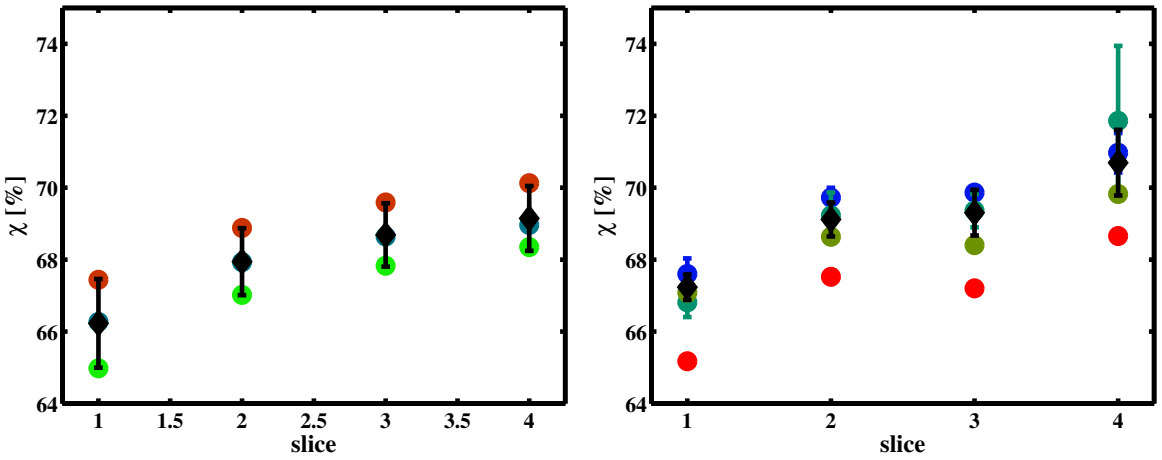

(a) (b)

Fig. 5.16.: Comparison of individual and averaged (a) crystallinities of native street pipe samples and (b) native pavement pipe samples as a function of sample slice. Averaged values represented by ♦.

regarding operation under pavements amounts to about 3.5 %. Again, averaged values are calculated and depicted in fig. 5.16(b).

Operation under streets thus does not seem to have a effect onto the crystallinity gradient within the pipe wall. Similar crystallinity differences between outer and inner surface can be observed. Solely the progression of the crystallinity curve is different.

5.1.4. Conclusions

In the following, the findings presented in the previous section should be related to the production process of gas pipes, the position within the pipe wall, natural and artificial ageing, recrystallisation processes and the operating place.

Two-dimensional XRD scattering patterns measured for PE sample slices showed Debye-Scherrer rings with inhomogeneous intensity distribution. A rather strong texture could be observed in the horizontal plane for the [020] reflection and in vertical direction for the Debye-Scherrer rings belonging to the {200} and {400} direction. The [110] and [210] reflections show texture in the corresponding {110} and {210} and equivalent directions. Referring to this identification of Bragg reflections, a preferred orientation of crystallites within the pipe wall can be supposed. The observations indicate an a-axis

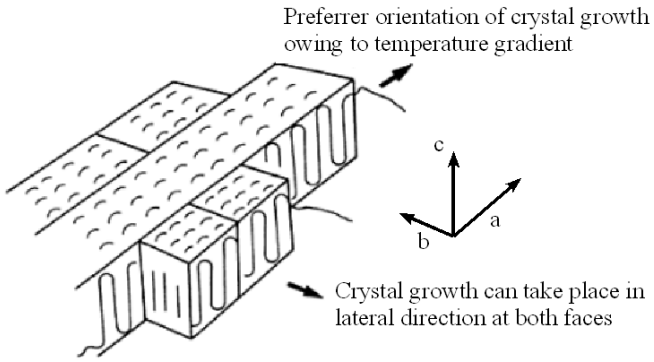

Fig. 5.17.: Schematic representation of lamellar crystal growth in a cooling melt. From [64].

oriented parallel to the long axis of the pipe and a b-axis parallel to the lateral wall surface.

Due to the direction of the incoming beam, the analysis is less sensitive concerning the crystallographic c-axis. Referring to the deduced orientation of a- and b-axis and an orthorhombic PE unit cell, the c-axis and thus the chain direction are supposed to point in radial direction. This assumption is only valid for the surface slices, whereas the missing or substantially less pronounced texture does not indicate a preferred orientation of crystallites within the bulk. Thus, only a- and b-direction are discussed.

A stronger texture corresponds to an enhanced preferred orientation of crystallites with respect to each other. In general, the texture is rather weakly pronounced, but deviations between different slices can nevertheless be detected. Outer surface slices of all samples show a higher preferred orientation of crystallites than in the bulk and at the outer surface, whereas a strong texture could be observed for the inner surface of artificially aged pipes.

The preferred orientation of crystallites might be associated to temperature gradients occurring in the extrusion process, which possibly cause direction dependent crystal growth [64]. Regarding the extruded pipe, the direction of the largest temperature gradient is parallel to its long axis. It results from the translation of the growing pipe through the cooling water bath. While passing the temperature gradient, lateral crystal growth could be induced in this direction, with a-axis parallel to the long axis of the pipe and b-axis presumedly perpendicular to the a-axis and lying in the wall surface, as should be emphasised in fig. 5.17.

This result is in strong contrast to texture observations in thin PE films. In this case chains possess an orientation parallel to the surface of the carrier material [75, 80]. The low film thickness is a strong constraint for crystal growth in direction normal to the carrier surface. This confinement is obviously not existent in the case of a bulk material. Experiments by Lindenmeyer and Lustig [63] and Holmes and Palmer [42] do instead of in fact confirm the results of this work.

The lowest amount of crystalline material could be found in all cases at the outer surface, while the highest crystallinity could be determined for the inner surface. The crystallinity deviation amounts to about 3-5 % and might be associated to the extrusion process. The cooling of the pipe at the outer surface via water bath could lead to a temperature gradient over the cross-section of the pipe wall. The closer the proximity to the hotter inner surface, the longer is the crystallisation time. This might result in a higher crystallinity at the inner surface.

This position dependency of χ does not agree with results by Gedde and Ifwarson [36], who examined the crystallinity of cross-linked PE water pipes. They obtained for both lateral surfaces similar and lower values than for thin bulk slices of the investigated 10 mm thick water pipe.

Furthermore, crystallinities of artificially aged pipes seem to be slightly higher than the deduced amounts of crystalline material of the native pipes. This might be associated to the fact that a crystallisation process has not finished after cooling down of the melt to the required temperature. In fact, secondary crystallisation processes can endure many years [82], resulting in increasing crystallinities due to permanent transformation of amorphous material into crystalline domains. Another reason for the observation of lower crystallinities in native gas pipes might be the consumption of anti-oxidants and plasticisers, which should prevent the material from ageing, by the elevated temperatures applied in the ageing experiments, or the washout of these additives by the streaming gas. Material failure due to higher crystallinities might be favoured by the temporary outdoor storage of the pipes before the transport or installation. The pipes are then exposed to air and UV radiation, what might lead to the consumption especially of the anti-oxidants and thus lead to ongoing ageing of the material. Although no information is available concerning long term exposure of the examined pipes to air and UV radiation

before their installation, this is at least often the case for today manufactured gas pipes. Thus, not only the consumption of anti-oxidants, plasticisers and UV stabilisers or by wash-out due to the streaming gas leads to a growing crystalline fraction, but also permanent crystallisation processes. Experiments yielding the residual content of anti-ageing additives could also affirm that the crystallinity is enlarged at the inner surface of most of the examined pipes.

As already mentioned in the introduction of the sample system, increasing crystallinities considerably influence material properties like Young's modulus. Fig. 5.18 visualises the relationship between crystallinity α (which corresponds to the quantity χ used in this work) and Young's modulus E_t ($\widehat{=}E$), as deduced by H. Beerbaum [22].

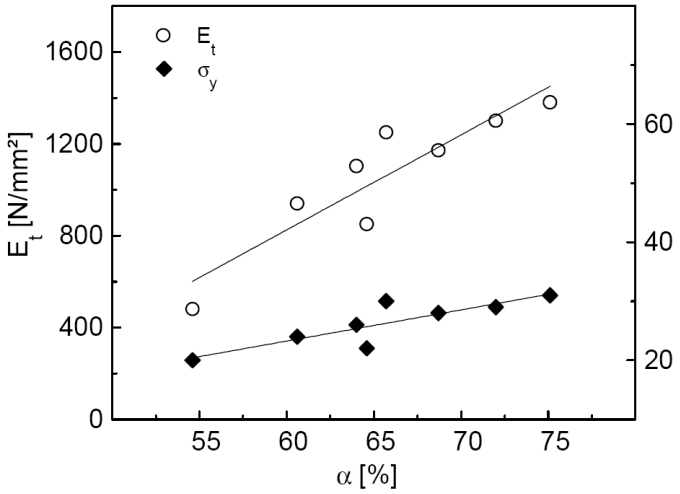

Fig. 5.18.: Interpolated relation between tensile modulus E_t and crystallinity α. From [22].

According to that, a crystallinity increase is associated to an disproportionate increase of Young's modulus. Due to the reciprocal relationship between Young's modulus and the elasticity of a material (see section 2.2), an increasing crystallinity is connected with a higher brittleness of the material and thus material failure becomes more probable.

According to Beerbaum, a crystallinity growth of 1 % is associated with an increase of Young's modulus that amounts to 3.53 %. In textured materials like the examined gas pipes, the direction dependency of Young's modulus and elasticity becomes considerably important. Regarding PE this means a higher tensile modulus in {200} direction than

in {020} direction [55]. The [200] lattice planes are thus more vulnerable for external forces and material failure is supposed to appear in this direction.

The rather strong texture and the increased crystallinity at the inner surface of aged pipes compared to the outer surface and the bulk indicate weak points in the structural integrity of the pipe wall, which is additionally confirmed by the results of the internal pressure tests. Fig. 5.19 shows a pipe sample after material failure in such a test. The nascent crack emanated from the inner wall surface and propagates to the outer surface, where the pipe finally bursts. Afterwards, a crack growth parallel to the long axis of the pipe could be observed. This finding is confirmed for all examined samples.

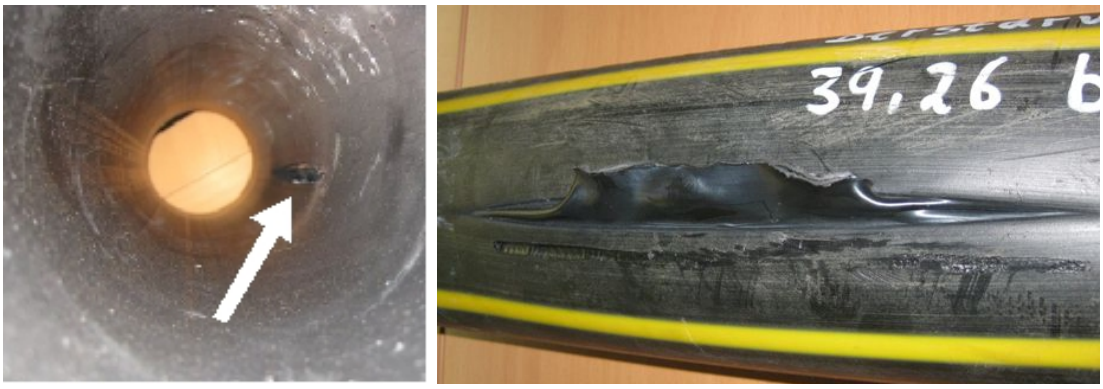

Fig. 5.19.: Views from inside and outside of a cracked pipe sample after internal pressure test. By courtesy of RWE.

Furthermore, pipes showing the highest crystallinity at the inner surface, also suffer first from material failure, confirming the assumption, that areas with enlarged crystallinity are weak points in the structural integrity of the pipe wall.

A comparison between gas pipes utilised under streets and under pavements indeed revealed a differing progression of the crystallinity curves between outer and inner surface, but the difference in the general amount of crystalline material was similar with about 2-3 %. A higher probability for material failure for one of the two working places cannot be deduced from these measurements.

5.2. X-ray diffraction studies of annealed polyethylenes

5.2.1. In-situ annealing experiments

In order to analyse the change of crystallinity with temperature, native samples have been heated in the temperature range between room temperature and 100 °C and diffraction patterns were measured in-situ for each temperature.

The 2D diffraction patterns are analysed as described before. Crystallinities, lattice constants and crystallite sizes were accordingly calculated by using equations (2.1), (5.1), and (5.2). These values are partially averaged for similar temperatures.

Temperature dependent background-corrected one-dimensional scattering patterns for the inner surface slice R3E4 are exemplarily depicted in fig. 5.20 and representatively for all examined sample slices discussed. For low temperatures the amorphous contribu-

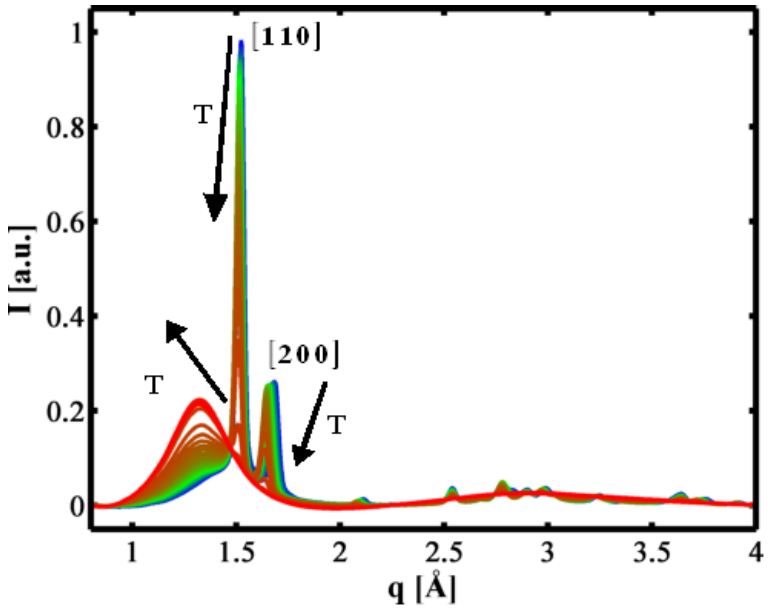

Fig. 5.20.: Temperature progression of one-dimensional scattering patterns of an inner surface slice (sample R3E4).

tion to the scattering pattern is superimposed by the strong diffraction peaks of the crystalline fraction of the sample. The positions especially of the [200] reflection and the amorphous scattering band shift to lower q-values with rising temperature, while reflections associated with the b- and c-direction of the crystallographic unit cell hardly

change. The peak height of the crystalline signal reduces with increasing temperature, while the amorphous scattering band becomes stronger. At a temperature of 94 °C a crystalline signal can no longer be detected. Crystalline peaks hidden by the amorphous halo at these elevated temperatures are in good accordance to [24, 88].

These changes will be analysed in detail in the following.

Determination of temperature dependent peak positions and lattice constants

First the evolution of peak positions of the [110] and [200] reflections are determined and the lattice constants a and b are deduced from this positions for each temperature using equation (5.1). Since large deviations could not be observed for different sample slices, the corresponding temperature dependent quantities will be illustrated for one representative sample. This is sample slice R3E4.

As can be clearly seen in fig. 5.21(a), the peak position q_{110} is slightly decreasing with rising temperature. The positions of the [200] reflection in contrast strongly shift to lower q values. While lattice constant $b(T)$ is only slightly varying with increasing temperature, the value of $a(T)$ is strongly depending on the annealing temperature, what is in good accordance to results found by Bunn *et al.* [24] for a flat surface film, Caminiti *et al.* [27] for a rod like sample and Schauer *et al.* [76]. This finding is supported by the fact that the [020] reflection does not change its position with rising temperature, as a qualitative analysis revealed. Accordingly, the lattice parameters follow the trend depicted in fig. 5.22 by Swan [83], who examined the temperature evolution of the two lattice constants a and b over a temperature range between -200 and 150 °C.

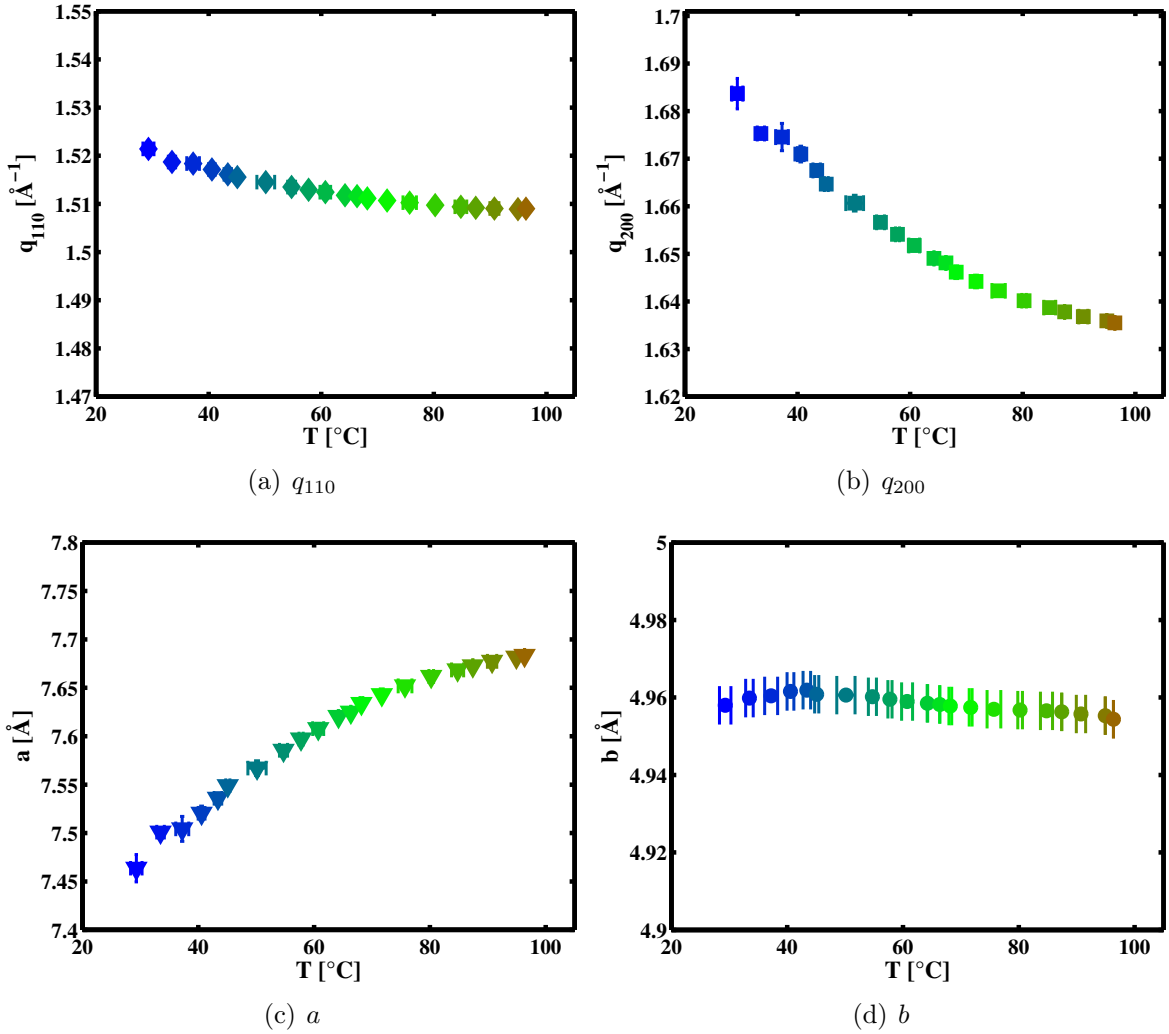

(a) q_{110} (b) q_{200}

(c) a (d) b

Fig. 5.21.: Temperature dependent (a) peak positions q_{110}, (b) q_{200}, (c) lattice constant a and (c) lattice constant b for the sample cuboid R3D.

Determination of temperature dependent crystallinities

The results for the crystallinities estimated according to eq. (5.3) of sample cuboid R3D are depicted in fig. 5.23. Image (a) and (d) show the χ-T-curves for the outer (a) and inner (d) surface wall slices R3D1 and R3D4. The crystallinities of the two bulk slices R3D2 and R3D3 can be seen in the figures (b) and (c), respectively. These temperature series have been conducted in order to find ideal heating parameters and are thus discussed in less detail than the results of cuboid E.

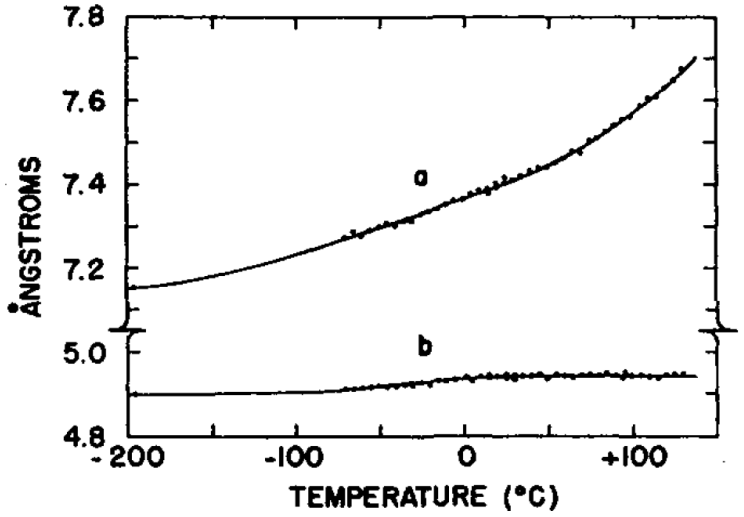

Fig. 5.22.: Temperature dependence of the lattice constants a and b as found by Swan [83].

Slice R3D1 was the first examined test sample and thus only the first three temperature steps are shown. For sample slice R3D3 the entire temperature series was measured for the first time.

All $\chi - T$-curves show a decreasing crystallinity with increasing temperature. In the temperature range between room temperature up to 65 °C the decrease of χ is rather slow. Above 65 °C the reduction of χ is accelerated until finally the entire crystalline material is vanished. The temperature, at which only amorphous material remains, differs for each sample, but can be estimated for the entire sample cuboid to 92.6 ± 3.5 °C. Table 5.3 should summarise these crystallite melting temperatures T_{CMT}.

The temperature dependent crystallinities of the sample cuboid R3E (which was directly connected to R3D within the pipe wall) are depicted in fig. 5.24. The crystallinity of the surface slices are shown in fig. (a) and (d), while the ones of the two bulk slices can be seen in images (b) and (c). For these samples, complete temperature series with fine temperature increment were measured, basing on the experiences of the first experiments with the sample cuboid R3D.

The $\chi - T$-curves of all four slices show clearly the same progression as the crystallinity obtained for sample slice R3E3. In principle, the amount of crystalline material is first slowly decreasing until the softening of the material is initialised at a temperature of

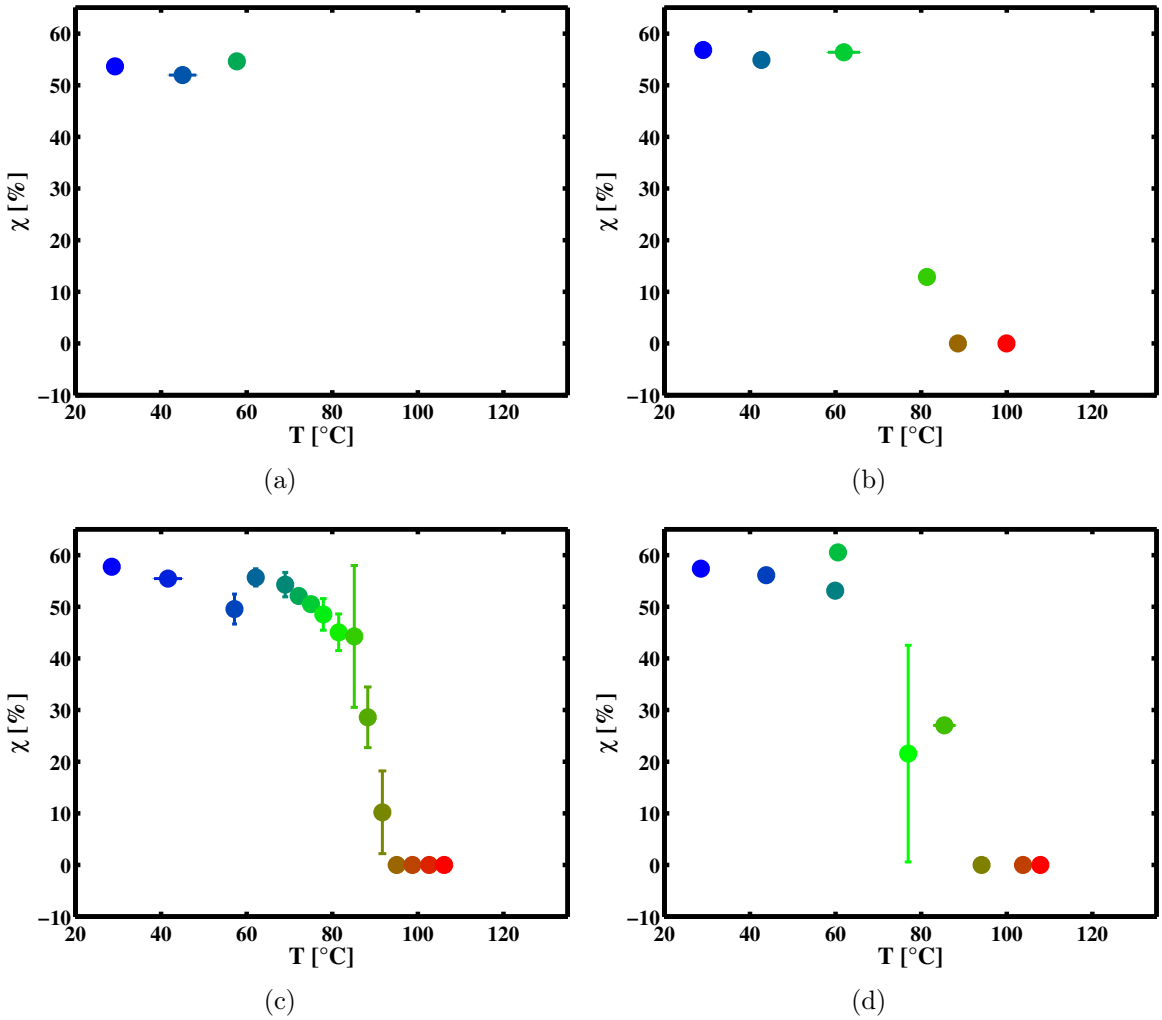

Fig. 5.23.: Temperature dependent crystallinities for the sample cuboid R3D.

about 70 °C. For further increasing temperatures a strong decay can be observed for all samples.

In the temperature range just before the crystallite melting a linear decrease of χ can be observed. In the course of this linear decay the crystalline fraction drops to zero, resulting in a fully amorphous sample slice. The averaged crystallite melting temperature for cuboid R3D can be estimated to 100.2 ± 2.8 °C. The temperatures, at which the complete transformation in a fully amorphous material has finished, are listed in tabular 5.3.

The transformation of crystalline into amorphous material with rising temperature found for PE samples used as pipes under real conditions are in agreement with results

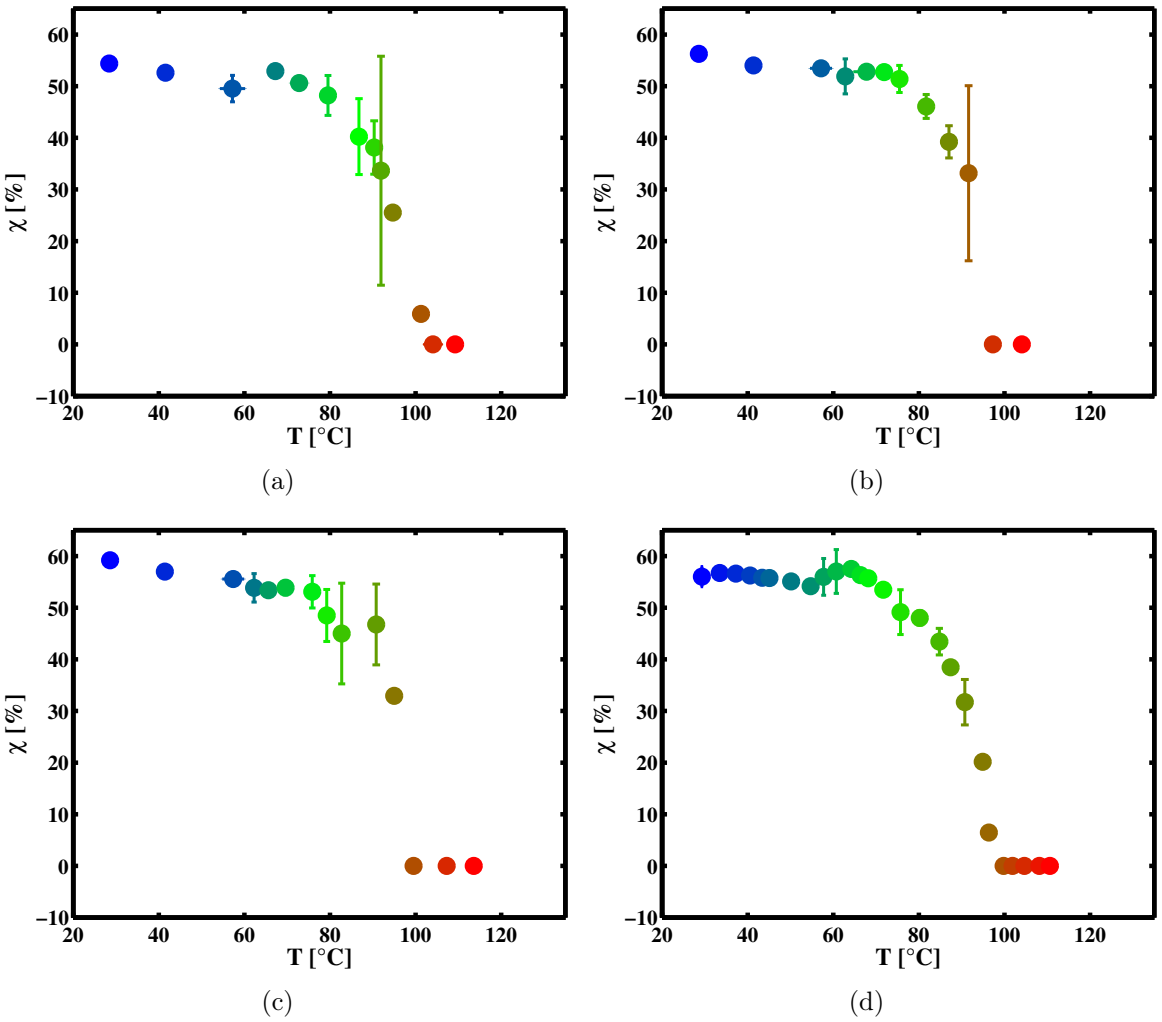

Fig. 5.24.: Temperature dependent crystallinities for the sample cuboid R3E.

	slice 1	slice 2	slice 3	slice 4	$\overline{T}_{\mathrm{CMT}}$
T_{CMT}(R3D) [°C]		88.6	95.1	94.1	92.6 ± 3.5
T_{CMT}(R3E) [°C]	104.1	97.3	99.5	99.8	100.2 ± 2.8

Tab. 5.3.: Crystallite melting temperatures T_{CMT}.

for similar experiments performed by Ueno *et al.*, Kakudu *et al.* and Albrecht *et al.* [88, 49, 18], who studied model systems. The similarity between these studies of model systems and the real PE pipes used for 35 years under working conditions investigated in this work should be illustrated by fig. 5.25, showing the temperature dependent crystallinity of thin films.

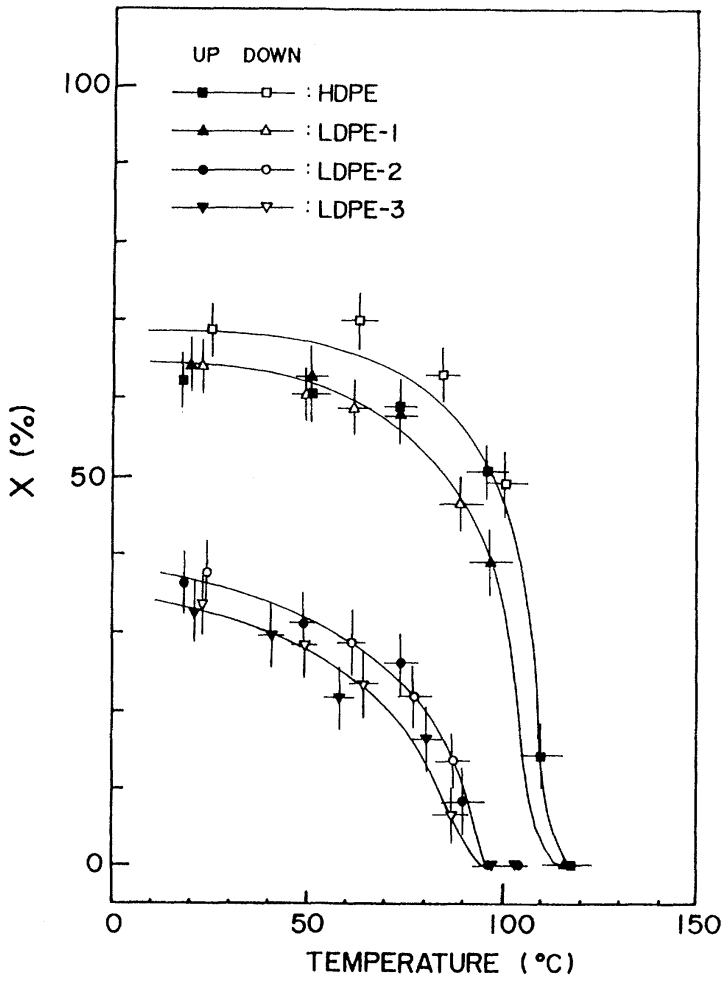

Fig. 5.25.: Temperature dependent crystallinity as found by Ueno *et al.* [88].

Determination of temperature dependent crystallite sizes

After the consideration of crystallinities depending on the positions within the pipe wall and the applied temperature, the crystallite size in {200} direction should calculated by using eq. (5.2) be discussed. The results are depicted in the figures 5.26 and 5.27.

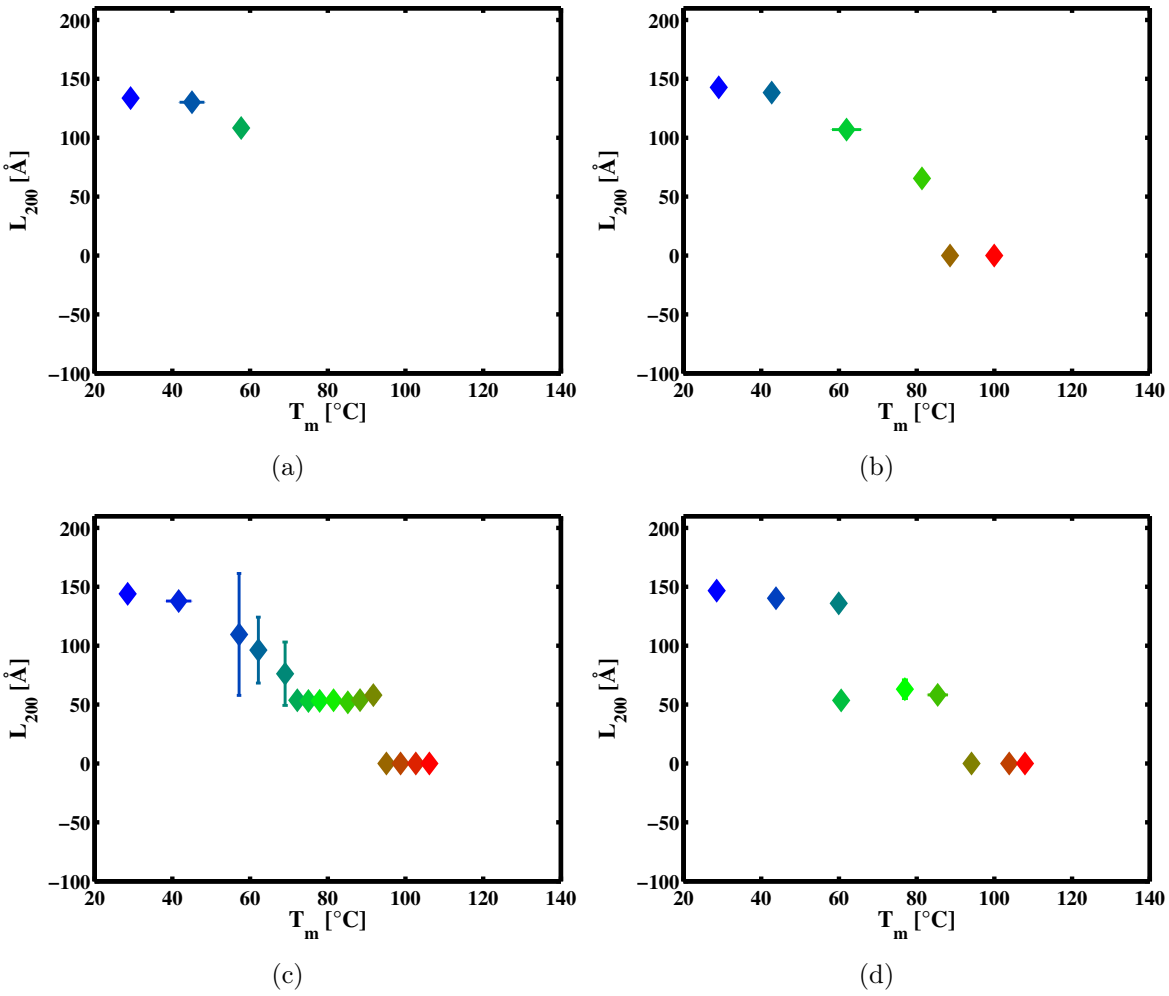

Fig. 5.26.: Temperature dependent crystallite size L_{200} for the sample cuboid R3D. The dotted lines are guide lines for the eye. (a) Outer surface, (b) first and (c) second bulk and (d) inner surface slice.

The crystallinities discussed before show decreasing values with rising temperature. This trend could be confirmed by analysing the corresponding temperature dependent crystallite sizes, as L_{200} is reducing from maximal values for room temperature to vanishing L_{200} at the crystallite melting temperatures shown in tab. 5.3 for each examined sample slice.

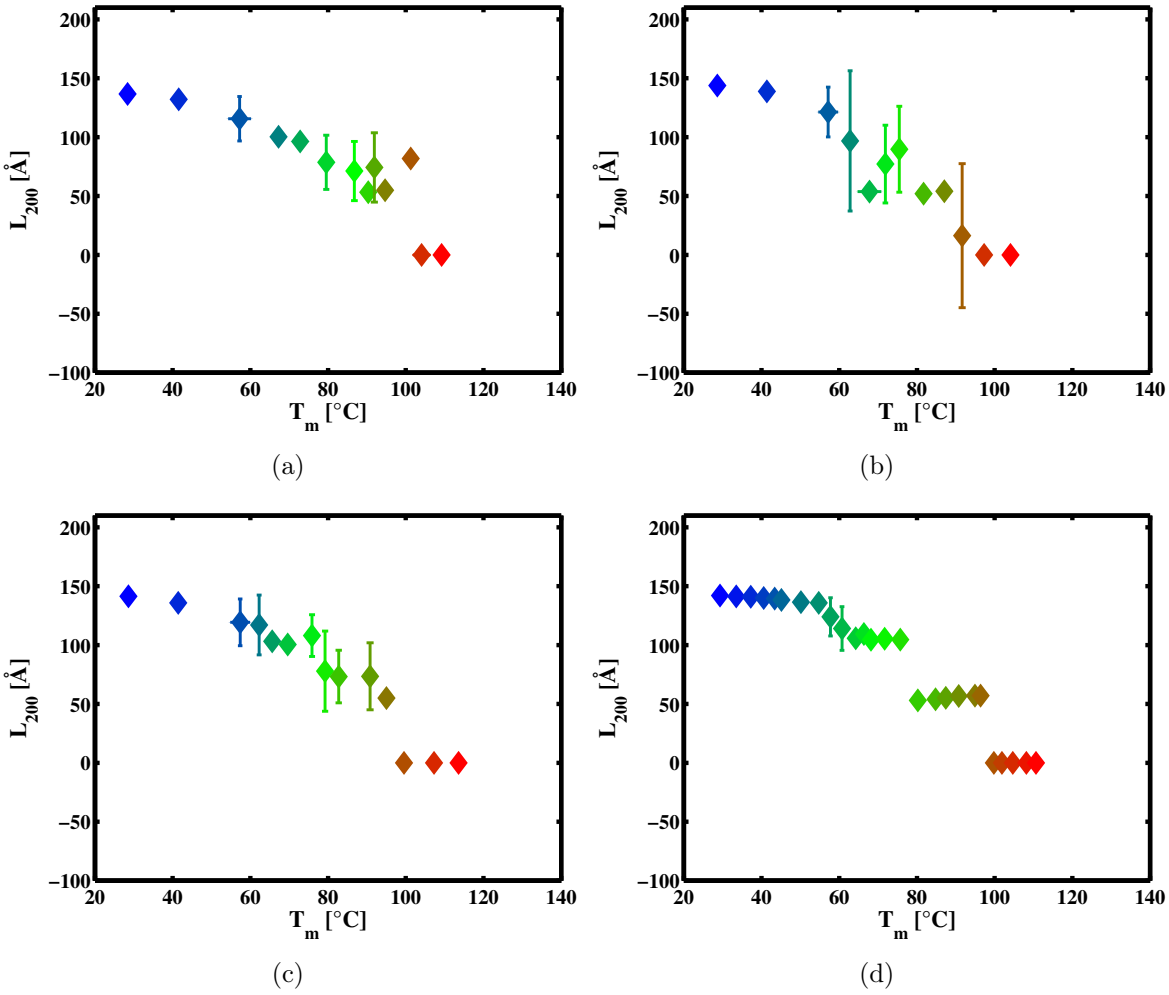

Fig. 5.27.: Temperature dependent crystallite size L_{200} for the sample cuboid R3E. The dotted lines are guide lines for the eye. (a) Outer surface, (b) first and (c) second bulk and (d) inner surface slice.

Linear thermal expansion coefficient

In the following, the development of the lattice constants a and b should be analysed with respect to the evolution of the unit cell size. According to the explanations in sec. 2.2, the differences between subsequent temperatures and values for lattice constants were calculated. To deduce the linear thermal extension coefficient, a straight line was fitted to the data. The highest temperatures were ignored due to the obvious influence of the final melting. After drawing the lattice constant deviations $\Delta a/a_0$ and $\Delta b/b_0$, respectively, vs. ΔT, a linear fit was conducted. a_0 and b_0 are the initial lattice

constants at room temperature. The deduced slope of the straight line is the linear thermal expansion coefficient for the corresponding direction.

The deduced lattice constant variations $\Delta a/a_0$ and $\Delta b/b_0$ and the result for the fit for lattice constant a for sample slice R3E4 can be seen in fig. 5.28. Since $\Delta b/b_0$ does not show large variations, the lattice expansion in b-direction is not significant. Thus the fit is missed in the image and this direction will not be considered in the following. For the linear expansion coefficient α_a in a-direction, a linear progression can be found for ΔT between 0 and 62 °C. The slope of the straight line and thus the expansion coefficient amounts to $(0.00061 \pm 0.00007)\,\mathrm{K}^{-1}$.

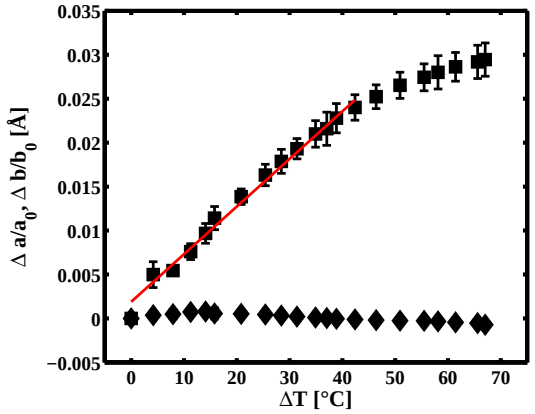

Fig. 5.28.: Temperature dependent lattice constant differences for a (■) and b (♦) for the sample slice R3E4 with fitted straight line for $\Delta a/a_0$. The slope yields the linear thermal expansion coefficient α_a.

The unit cell has thus suffered a size modification Δ_L of 2.93 % in the temperature range between 29.31 ± 0.99 °C and 95.65 ± 1.01 °C in the a-direction of the crystallographic unit cell, while the size is nearly constant in b-direction. The corresponding thermal expansion coefficient is two orders of magnitude smaller than α_a. The size growth was thus the strongest in the direction parallel to the surface and parallel to the long axis of the pipe wall, according to the deduced results presented in section 5.1.1. The constant cell parameter in b-direction could be found for all examined samples.

The size modifications Δ_L are in good accordance to Bunn *et al.* with $\Delta_L = 3.1\,\%$ and Caminiti *et al.* with $\Delta_L = 2.5\,\%$.

The following tabular 5.4 should give an overview of thermal expansion coefficients deduced for each examined sample slice. Average expansion coefficients of $0.00059 \pm$

$0.00009\,\mathrm{K}^{-1}$ and $0.00061 \pm 0.00004\,\mathrm{K}^{-1}$ could be determined for the sample cuboids R3D and R3E, respectively. The dimension of α_a confirms results by Bunn *et al.* [24] ($\alpha = 0.00038\,\mathrm{K}^{-1}$, flat surface film), Kerch *et al.* ($\alpha_a = 0.00031\,\mathrm{K}^{-1}$, stretched PE sample) and Swan [83] ($\alpha_a = 0.000578\,\mathrm{K}^{-1}$).

slice	α_a [$10^{-3}\mathrm{K}^{-1}$]	Δ_L [%]
R3D1	0.70 ± 0.03	2.69
R3D2	0.53 ± 0.05	2.86
R3D3	0.51 ± 0.09	3.13
R3D4	0.57 ± 0.05	2.79
R3D	0.59 ± 0.09	2.87 ± 0.19
R3E1	0.61 ± 0.07	2.91
R3E2	0.61 ± 0.06	2.59
R3E3	0.62 ± 0.06	2.51
R3E4	0.54 ± 0.07	2.40
R3D	0.61 ± 0.04	3.35 ± 1.38

Tab. 5.4.: Linear thermal expansion coefficients α_a for the sample cuboids R3D and R3E.

An enlargement of cell parameters is associated with a weakening of intermolecular interactions. This leads to a reduced resistance against external forces and thus to a higher probability of material failure.

Texture analysis

In order to investigate possible texture modifications, partial integrations of the two-dimensional scattering patterns have been conducted. The following data analysis follows the same course as before. The ratio of the determined peak heights in vertical and horizontal direction yields a measure of the texture. Values for temperatures lying close together are again averaged. The ratios for both analysed [110] and [200] reflections of both surface slices of sample cuboid R3E and one bulk slice can be seen in fig. 5.29. Besides small variations, that are within the error, no change in texture can be observed.

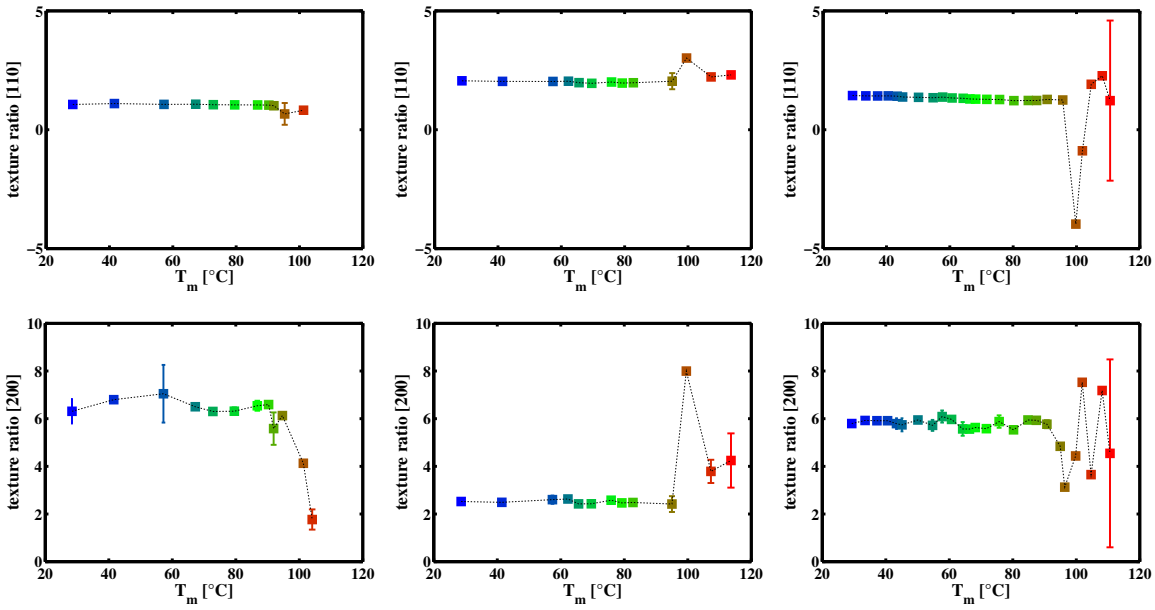

(a) Outer surface. (b) Bulk. (c) Inner surface.

Fig. 5.29.: Temperature dependent ratio of peak heights deduced from 0- and 3-9-o'clock-direction for the sample cuboid R3E for the [110] and [200] reflection. The dotted lines are guide lines for the eye.

The large variations for temperatures above 90 °C can be assigned to large modifications within the molecular and superstructure taking place during the fusing of the material.

5.2.2. Ex-situ annealing experiments

In the following, the results obtained from ex-situ annealing experiments will be presented. They have been conducted for the inner surface slice R3C4 and for the bulk slice R3C2 of the native sample cuboid R3C. The bulk slice was annealed at temperatures of $T = 90$, 100, 110, 120, 125, 130, 135, and 140 °C, respectively, and afterwards diffraction experiments took place after each temperature step. The last temperature step is missed for the inner surface slice due to strong softening of the sample, which inhibited the fixing of the sample slice into the sample holder. The course of the analysis was the same as before with a background correction, several normalisations and the final profile refinement outlined in section 5.1.2. The crystallinity data, derived from this procedure, is depicted in fig. 5.30 with temperature dependent crystallinities for both samples. Crystallinities of the surface slice R3C4 are characterised by red diamonds, while the bulk crystallinities of slice R3C2 are marked by blue squares. The level difference

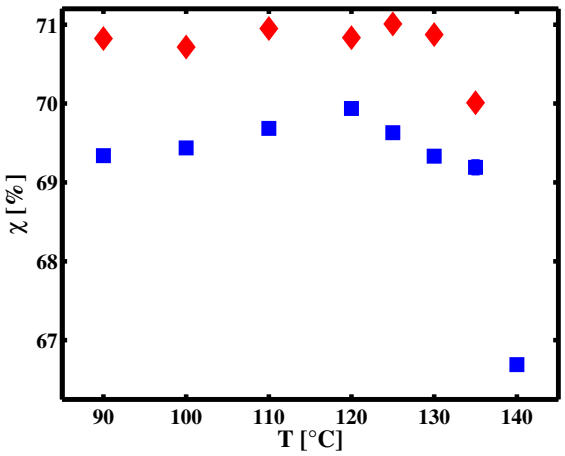

Fig. 5.30.: Temperature dependent crystallinities χ for the native bulk slices R3C2 (■) and the inner surface slice R3C4 (♦).

between surface and bulk slice can be seen on the first glance and is existent for all examined temperature steps. In each case the surface crystallinity is higher than the bulk crystallinity. The difference amounts to about 1.5 % at the lowest temperature of 90 °C and is reducing until a temperature of 120 °C. In the following, the difference enlarges for 125 and 130 °C, only to reduce again for 135 °C to 0.82 %.

5.2.3. Summary and comparison between ex-situ and in-situ annealing experiments

Crystallinities determined in in-situ annealing experiments first show a slight decrease and, after reaching a temperature of 70 to 80 °C, a strong reduction with regard to the amount of crystalline material. This temperature is associated to a softening of the material and its value is consistent with findings in [10, 11]. For each of the samples, a continuous diminution of the crystalline fraction can be observed for rising temperatures. At different temperatures of about 100 °C, the material is fully amorphous. These important temperature steps are in good accordance to the data shown in the following image.

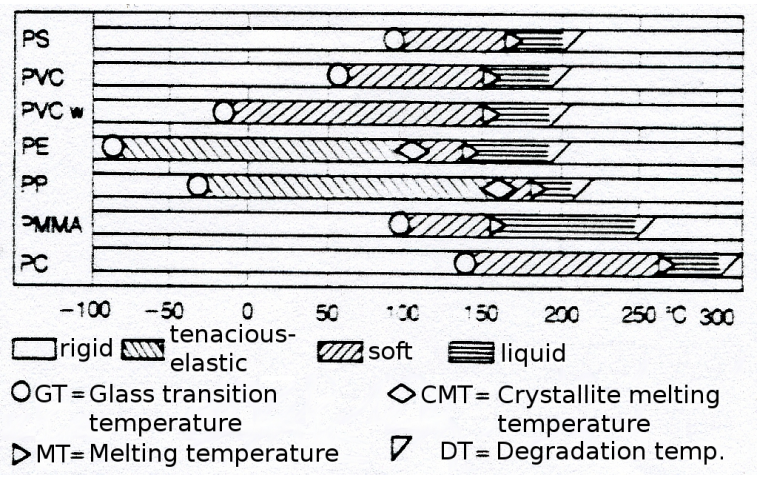

Fig. 5.31.: Temperature behaviour of some polymers. Burrowed from [37].

The image shows different important temperature regimes and corresponding phase transitions of some polymers. The temperature dependency of PE is depicted in the forth row and designates a crystallite melting temperature of 100 °C and an overall melting temperature of ∼140 °C, which could be confirmed in the annealing experiments.

Temperature dependent crystallinity curves shown in section 5.2.1 are in very good accordance to results obtained by Albrecht and Strobl [18] and Ueno *et al.* [88], although the authors have examined thin film samples with a thickness of only 20-400 Å, which describe exact the same progression as especially the $\chi - T$ curves with high temperature resolution presented in fig. 5.24. When comparing the temperatures at which the softening is starting and the crystallite melting is completed with the initial

crystallinity, it becomes clear that higher initial crystallinities result in higher softening and crystallite melting temperatures. The overall melting temperature shows the same temperature dependence.

χ curves obtained in ex-situ annealing experiments indicated recrystallisation processes during the subsequent cooling of the sample slices to room temperature during the scans, resulting in contrast to the discussed in-situ annealing studies in increasing crystallinities before reaching the softening temperature.

The strong reduction of the crystallite size in {200} and the growth of the lattice constant a with rising temperature accompany the discussed strongly decreasing amount of crystalline material. These findings indicate that in this direction first a unit cell expansion takes place, which is followed by a degradation of the crystallite at the {200} crystallite face. Since the lattice constant a is per se the largest lattice constant, the chains are also separated by the largest distance in this direction. This leads to the weakest intermolecular attraction between adjacent chains and thus to the lowest resistance against degradation. The attraction in direction of the crystallographic a-axis is characterised by the lowest binding energy, resulting in the easiest direction for aggregation during crystal growth, but also the lowest stability. This lateral separation was also suggested by Otegui *et al.* [65] and corresponds to higher Young's moduli in that direction, as discussed before. That finding matches the unfolding of chains in drawn crystallites as supposed by Peterlin [70]. Linear thermal expansion coefficients describing the behaviour of the lattice constants a and b confirm these observations and are in good accordance to experiments by other authors [25, 83, 50]. Thus, according to the temperature dependent progression of χ and L_{200}, the decomposition of the material is supposed to be obviously at the expense of the {200} direction. Texture analysis revealed that no modification of crystal orientation took place. Although the PE chains gained a higher mobility, the degradation of the crystallites happened obviously parallel to crystallographic axis and thus lattice planes.

5.3. Analysis of small angle scattering data

A qualitative inspection of two-dimensional SAXS patterns of the 4 sample slices of pipe R3D, depicted in figures 5.32(a) to 5.32(d), revealed inhomogeneous intensity distributions at low q-values. The second row represents the sections around the direct beam for better visualisation. Distinct differences can be observed especially in the

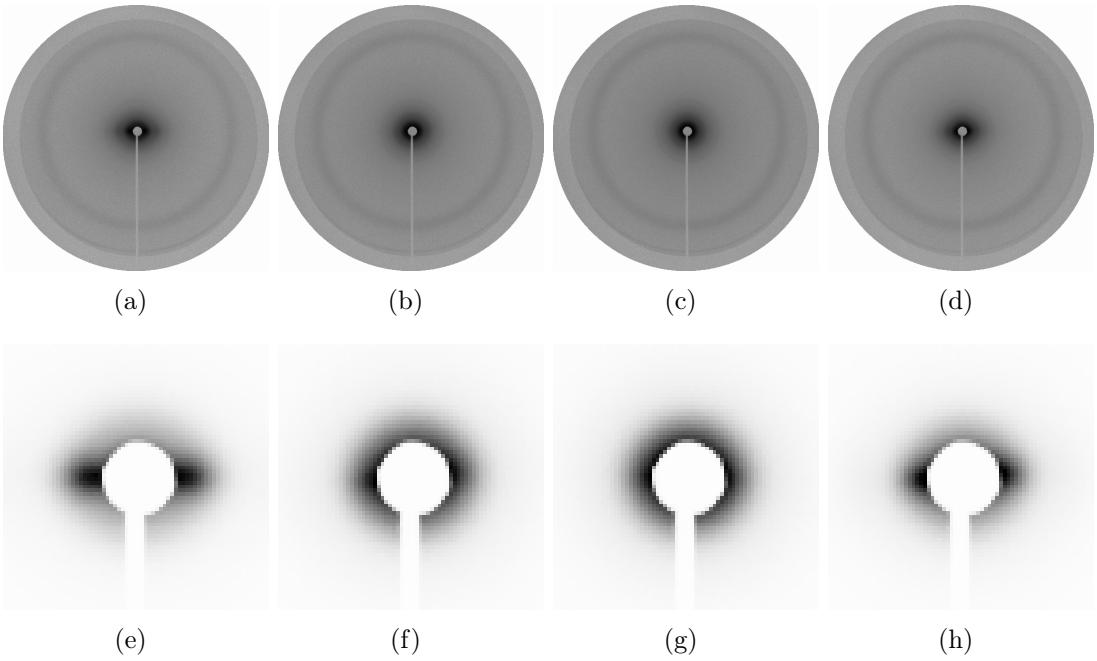

Fig. 5.32.: 2D SAXS pattern of native sample slices. (a) Outer surface, (b) first and (c) second bulk slice, (d) inner surface. Figures (e) to (h) represent small sections around the direct beam for better visualisation.

comparison between surface and bulk samples. While both surface slices show a strong ellipsoidal signal in the equatorial plane of the two-dimensional scattering image, this orientation dependency is only weakly pronounced in the case of the two bulk slices. This is emphasised by integrating the 2D SAXS patterns in horizontal and vertical plane as shown in fig. 5.33. Obviously, the ellipsoidal signal gives rise to distinct shoulders in the one-dimensional pattern along the horizontal direction. This relation is even more emphasised in a representation Iq^2 vs. q^2 as depicted in the bottom diagram of fig. 5.33.

XRD measurements performed by Al-Raheil and Okaz showed that the long axis of PE lamella is oriented parallel to the crystallographic b-axis [17]. Thus, referring to the texture analysis of the discussed XRD experiments and corresponding to the

two-phase model presented in section 3.4.2 and the presented superstructures in 2.2.4, the peaks arising in the one-dimensional scattering pattern in horizontal direction could be associated to the long axis of the lamellar structure of PE.

Following these considerations, direction dependent analysis of two-dimensional SAXS spectra can reveal the long period of the crystalline polymer structure along the b-axis, i.e. the sum of thicknesses of the crystalline and amorphous layer.

For the determination of the longspacings and crystallinities this orientation dependency is not regarded, since the crystallinity should be determined for the entire sample and not only for one direction. This enables a better comparability with values obtained in XRD experiments. After determination of the long period and thus the crystallinity, surface and bulk samples will be compared and SAXS patterns of native and aged samples will be discussed.

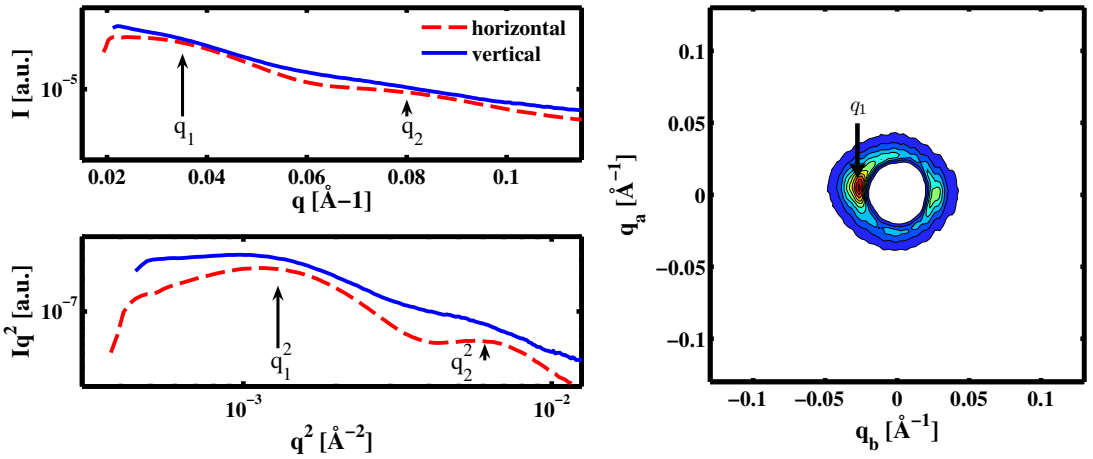

Fig. 5.33.: (a) Integrations in the horizontal and vertical plane of the scattering pattern in an I vs. q and Iq^2 vs. q representation. (b) Representation of the 2D pattern for low q values.

In the following, the quantitative determination of the lamellar structure will be discussed. Fig. 5.34(a) shows a typical background corrected one-dimensional SAXS pattern of a PE sample after full integration of the two-dimensional pattern. A distinct shoulder at q about $0.08\,\text{Å}^{-1}$ can be seen as well as the even less pronounced change in slope for $q \approx 0.03\,\text{Å}^{-1}$. A double logarithmic plot $q^2 \cdot I$ vs. q^2 is depicted in 5.34(b) and reveals a shoulder at $q_2^2 \approx 0.0014\,\text{Å}^{-2}$ and a peak for $q_1^2 \approx 0.0061\,\text{Å}^{-2}$. This corresponds

to positions $q_2 \approx 0.03\,\text{Å}^{-1}$ and $q_1 \approx 0.08\,\text{Å}^{-1}$. These maxima are so-called (first and second order) correlation peaks and yield a good approximation to the average spacing between two adjacent layer, consisting of an amorphous and a crystalline phase (see section 3.1.4). The correlation peaks can be related to the layer thickness or long period d_{ac} by the common equation $d_{ac} = \frac{2\pi}{q_c}$, whereas the second order correlation peak yields half of the layer spacing.

The following values have thus been estimated for the positions of the shoulders and the corresponding layer thicknesses:

q_1 [Å^{-1}]	L_1 [Å]	q_2 [Å^{-1}]	L_2 [Å]
0.03	209.44	0.06	78.5

Tab. 5.5.: Estimated values for correlation peaks and corresponding layer thicknesses.

A detailed analysis of the scattering pattern by calculating the correlation function yields more precise values for the longspacing of the layer system.

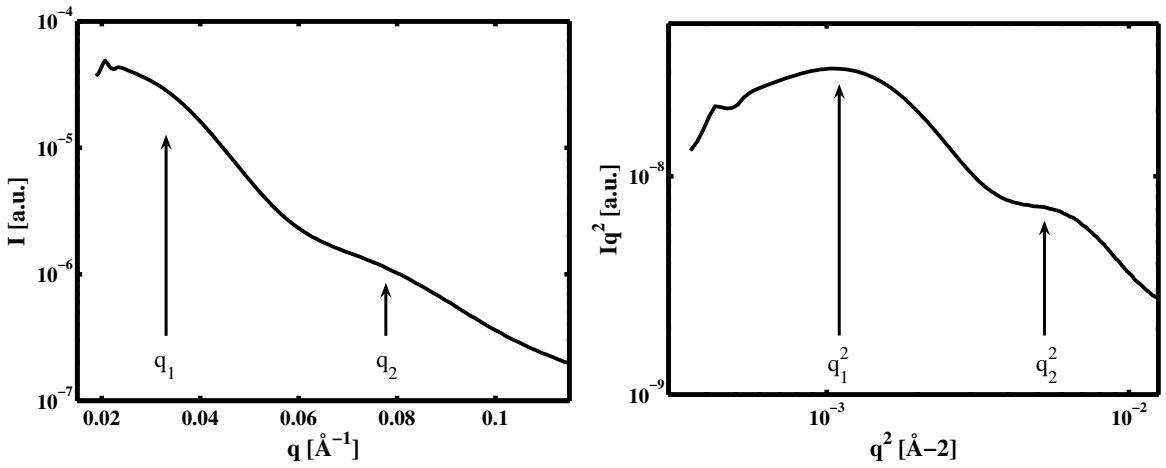

(a) (b)

Fig. 5.34.: (a) Exemplary background corrected one-dimensional SAXS pattern for a native sample slice, measured at DELTA. (b) Same data as in (a), but as $I \cdot q^2$-plot for better visualisation.

The quantitative analysis of small angle scattering data is divided into several parts. Depending on the place of data acquisition (DELTA or Helsinki), the two-dimensional spectra are treated in different ways. SAXS data acquired in experiments at DELTA are handled in the same way as the diffraction data. Firstly, the 2D-spectrum is integrated

with and without intensity conservation for the consideration of the distinct number of pixels per q-value. Then the normally integrated spectrum is normalised to the spectrum integrated with intensity conservation. This one-dimensional, normalised spectrum is used for the further data analysis. In the case of data measured in Helsinki the two-dimensional scattering pattern is integrated by the help of a MATLAB routine developed by the group of Ritva Serimaa. No further treatment is carried out before the background correction.

This background correction is performed by a subtraction of the (normalised) background scan after scaling in that way, that intensity before and after the Kapton peak at around $0.4\,\text{Å}^{-1}$ becomes zero. An exemplarily background subtraction is shown in fig. 5.35(a).

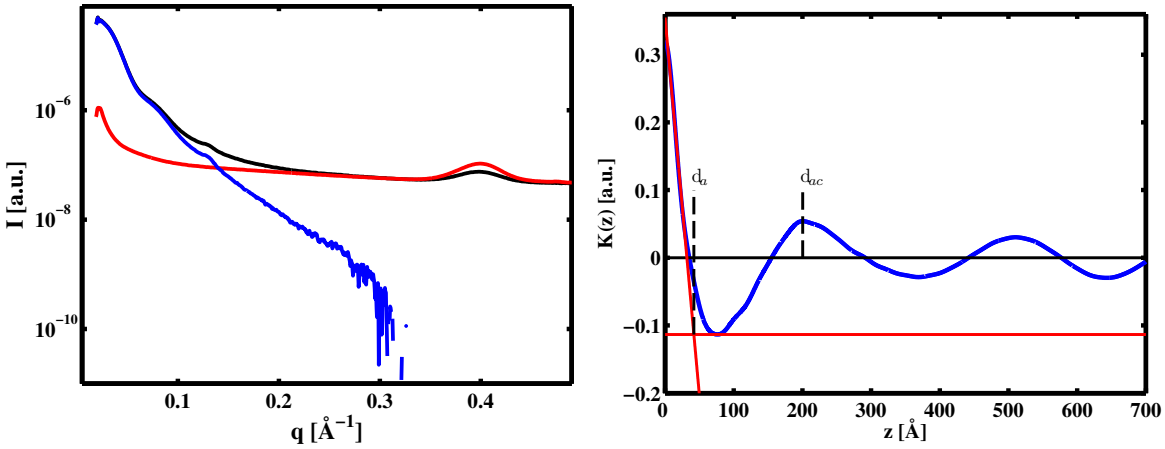

Fig. 5.35.: (a) Exemplary background corrected data set and (b) correlation function $K(z)$. The self-correlation triangle, consisting of baseline and straight line fitted to the low z-range, is drawn, as is also the position of the maximum which determines the entire lamellar thickness d_{ac}.

In the following, the small angle scattering data is analysed as discussed in sec. 3.4. For the Fourier transform of the data an interpolation of the with q^2 weighted scattering intensity Iq^2 for $0\,\text{Å}^{-1}$ and high q-values to zero-values of intensity is necessary. At low angles the weighting by the q^2 values leads to vanishing intensity, for high q-values the scattering intensity becomes zero. After that the Fourier transformation is accomplished via numerical integration. The resulting correlation function $K(z)$, depicted in fig. 5.35(b), yields the interesting parameters of lamellar thicknesses and crystallinity.

The position of the first local maximum yields the thickness d_{ac} of the entire lamella, consisting of a crystalline and an amorphous layer. It amounts to 200.50 Å. The value of $K(z)$ in the minimum yields the baseline $-B$, which is -0.1134. A straight line, fitted to the correlation function curve in the range between 0.8 and 2.77 Å, and the baseline build the self-correlation triangle. The intersection of baseline and straight line yields the amorphous layer thickness [1]. The difference of lamellar thickness d_{ac} and amorphous layer thickness d_a yields the thickness d_c of the crystalline layer, which amounts to 158.5Å and is in good accordance to results obtained by XRD. The sample's crystallinity can be deduced by calculating the ratio of d_c and d_{ac}. For the sample R3D1 the crystallinity has a value of 79.1%.

The following tabular summarises the values obtained for the exemplary sample slice R3D1:

d_{ac} [Å]	d_a [Å]	d_c [Å]	χ [%]
200.5	42.0	158.5	79.1

Tab. 5.6.: Layer thicknesses and crystallinity deduced from correlation function calculation for sample slice R3D1.

5.3.1. Summary of the results obtained in SAXS experiments

Qualitative analysis of two-dimensional SAXS patterns revealed equatorial streaks strongly visible for both surface slices and less pronounced for the bulk.

These inhomogeneous intensity distribution is supposed to be related to a lamellar layer structure, whose long axis is parallel to the b-axis of the pipe and chain direction parallel to the radius. Taking the crystal structure deduced from texture analysis of two-dimensional XRD patterns into account, the following chain and lamellar arrangement is supposed. In slice 1 and 4 a certain amount of lamellae is oriented with lateral surface parallel to the pipe wall surface. Furthermore, the lamellar long axis and thus the crystallographic b-axis are oriented tangential, while the chains point in radial direction.

[1] Due to the results discussed in section 5.1.3, the crystallinity χ_c is supposed to be larger than 50 %. Thus, the intersection of baseline and straight line fitted to the low z-part of the correlation function $K(z)$ determines the amorphous amorphous layer thickness d_a. For a crystallinity below 50 %, the intersection gives the crystalline layer thickness d_c [82].

Thus, when analysing direction dependent intensities in vertical direction, the dimension of the lamellae in b-direction is probed. In the bulk, no preferential orientation of lamellae could be stated. Accordingly, thicknesses and crystallinities obtained for the bulk slices are averaged values over all possible lamellar orientations.

Crystallinities obtained by analysing the correlation functions deduced from fully integrated scattering patterns showed only small deviations over the cross-section of the pipe wall, supposing that SAXS measurements are not really sensitive to amorphous material, that is not organised in the layers structure. The deduced crystalline thicknesses, averaged over all possible orientations and thus a measure for the lateral dimension of the lamellae in all direcionts, show on the other hand a distinct minimum at the outer surface and considerably higher values in the bulk and at the outer surface.

5.4. Comparison of complementary scattering data

Since several techniques and experimental setups have been used to investigate the crystallinity of PE samples, the results of the diffraction experiments accomplished at DELTA should be compared with SAXS results gained at the laboratory x-ray source in Helsinki and again at DELTA for the pipe samples R3 and R2. The corresponding crystallinities χ of the native pipe R3 and the aged pipe R2 are depicted in fig. 5.36(a) as a function of the sample slice. X-ray results are represented by blue squares, SAXS crystallinities determined from experiments at DELTA by green diamonds and the corresponding Helsinki crystallinities are represented by red circles, whereas markers for the native pipe are filled and for the aged pipe empty.

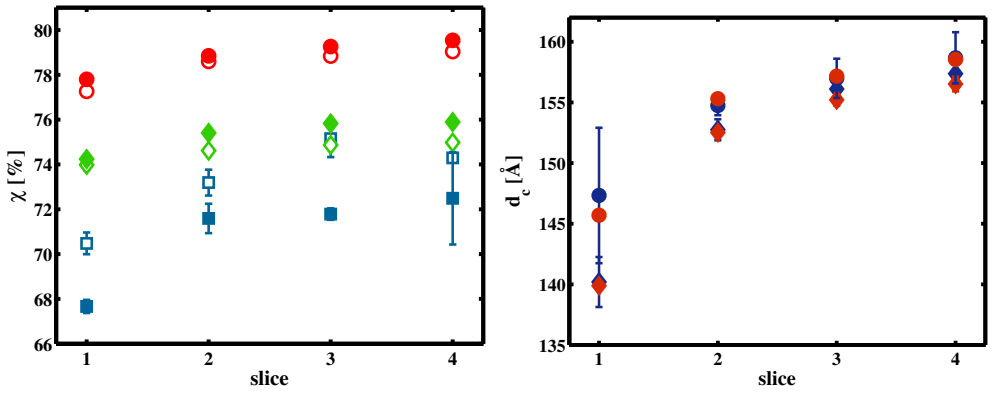

(a) (b)

Fig. 5.36.: Comparison of (a) crystallinities determined by x-ray diffraction (■), SAXS at DELTA (♦) and in Helsinki (●) for the native pipe R3 (filled markers) and the aged pipe R2 (empty markers). (b) Comparison of crystallite sizes obtained by SAXS at DELTA (native: ♦, aged: ♦) and in Helsinki (native: ●, aged: ●).

According to that, both SAXS experiments yielded considerably higher crystallinities than crystallinities obtained by XRD measurements, what it is good accordance to Vonk and Pijpers [90]. It could also be stated that crystallinities determined by calculation of correlation functions from SAXS intensities show only small variations over the cross-section of the pipe wall, in contrast to XRD crystallinities, that are strongly correlated to the position within the pipe wall. Crystallinities revealed by these experiments show strong differences between the and the inner surface.

The differences might be associated to the different quantities probed in XRD and SAXS experiments. While in XRD measurements density deviations of the entire sample are examined independent of orientations, in SAXS experiments only dimensions of superstructures or spacings between them are probed. If a considerable amount of amorphous material is not located in the lamellar layer structure along the observation direction, SAXS is insensitive to this contribution, resulting in underestimated amorphous fractions. In contrast, when texture is observed in XRD patterns, integral intensities are only shifting to the pronounced peak, but not vanishing. Thus, no information is lost by averaging of XRD intensities.

Lamellar thicknesses d_c as depicted in fig. 5.36(b) show the same trend as crystallite sizes L_{200} determined by XRD and are on average of same order. SAXS is thus indeed a suitable tool to determine the lateral expansion of the lamellar structure.

6. Summary and outlook

Different x-ray scattering techniques have been applied in order to investigate the ageing behaviour and molecular structure of several 35 years old HDPE gas pipes, which have been operated by the gas supplier RWE under streets or pavements. The manufacturers of these generation of PE pipes predicted a lifetime of 50 years, which is going to expire in the not too distant future. The pipes are characterised among other things by the ratio of crystalline and amorphous domains, which is defined as the crystallinity of the semicrystalline material.

Pipes used for years have been studied and were compared to others, that have been purposefully exposed to high pressures and temperatures in internal pressure creeping tests. These tests are a common method, the purpose of which is the simulation of the ageing behaviour of pipes under well defined conditions to estimate the remaining lifetime.

This artificial ageing process induces structure modifications, which should be verified via x-ray diffraction experiments. XRD and SAXS have been successfully applied to determine the crystallinity, which is strongly connected to several macroscopic material properties, parameters of the orthorhombic crystal structure like crystallite sizes and lattice parameters and expansion coefficients. Thin slices have been prepared in order to analyse the influence of the position within the pipe wall on these properties. Position dependent measurements could therefore reveal a strong correlation to the position within the pipe wall. With few exceptions the examined pipes showed a lower crystallinity at the outer surface and a 3-5% higher amount of crystalline material at the inner wall surface. This crystallinity difference is connected with a higher brittleness of the material at the inner surface and thus material failure becomes more probable.

The inspection of two-dimensional XRD patterns showed textured Debye-Scherrer rings especially at both lateral surfaces, from which the preferred crystallite orientation within the pipe wall could be deduced. The crystallite orientation following from texture analysis is in accordance to other authors and was found to be enhanced at the inner surface of artificially aged pipes. Preferred orientation is accompanied by directions within the crystalline structure, that are more vulnerable to anisotropic forces. These observations – preferred orientation and higher crystallinity at the inner wall surface – could be affirmed by internal pressure creeping tests, in which a crack initialisation at the inner surface and a propagation along the long axis of the pipe could be found. Thus, textured and highly crystalline inner surfaces of aged pipes are identified as weak points of the structural integrity of pipe walls.

Crystallinity and texture differences between outer and inner wall could be satisfactorily explained by analysing the manufacturing process, which is supposed to be responsible for a crystallinity gradient over the cross-section of the pipe wall and direction dependent growth of crystallites.

The comparison of crystallinities determined for native and aged pipes showed a slightly higher amount of crystalline material for the artificially aged samples, but still lowest amounts of crystalline material at the inner surface. This finding is supposed to result from general occurrent post-crystallisation processes. Furthermore, an increasing crystallinity in the course of time should be caused by the consumption of anti-ageing additives and plasticisers in ageing processes and erosion of these additives by the streaming gas.

In addition to x-ray scattering experiments depending on the position within the pipe wall x-ray diffraction studies of annealed PE samples were conducted. Decreasing crystallinities with rising temperature could be observed in in-situ annealing experiments. At temperatures above $\sim$100 °C the transformation into a fully amorphous material is complete. This is consistent with the temperature correlation of the crystallinity in PE model systems as discussed in literature [88, 49, 18]. The temperature dependent lattice parameters b and a and the associated crystallite size in $\{200\}$ direction indicate an expansion of the crystallites in a-direction. Thus, the decomposition of the crystallites is supposed to take place along the [200] lattice planes.

In order to reveal the microscopic structure of PE pipes, x-ray tomography experiments have been conducted with macroscopically unharmed and cracked samples. These measurements could not reveal detectable differences between both samples or precursors for material failure like micro cracks. Thus it could be concluded that ageing processes take place on smaller length scales, which are not accessible for tomography.

Comparison of results obtained by XRD and SAXS revealed that SAXS seems to overestimate in general the amount of crystalline material within the sample. Furthermore, the distinct variations of the crystallinity investigated by XRD are nearly invisible in the SAXS results. Thus, XRD is supposed to be a better tool for sample characterisation than SAXS.

The techniques applied in the scope of this work could indeed reveal position depending differences and structural modifications caused by ageing. Unfortunately it was not possible to identify in detail, which effects induced these modifications. Therefore, in future experiments one single parameter influencing the ageing behaviour should be modified and the effects onto the material should be investigated. The interpretation of the results might lead to an improvement of e.g. the production process or the kind of anti-ageing additives and their quantity.

In order to conduct these investigations with higher statistics, better systematics and precision, the successfully applied XRD setup had to be modified in that way that standardised experiments with high efficiency could be performed. Furthermore, thinner sample slices would increase the increment in position dependent experiments.

A. Appendix A

A.1. Three-dimensional imaging of PE samples – Tomography experiments

A.1.1. Introduction

In order to analyse polyethylene materials on larger length scales possible with diffraction techniques, x-ray tomography has proven to be a suitable method to gain information [34]. 1971 by Hounsfield and Cormack developed as powerful diagnostic instrument, x-ray tomography is today applied as non-destructive analysis method for example in process control in aerospace industries [12]. The main advantage of computer tomography with respect to conventional radiography is the acquisition of 2D images of a 3D object without distortions. A three-dimensional representation of the object is constructed from a series of this two-dimensional images.

Medical scanners are constructed to analyse materials with atomic number $Z < 20$ or densities lower than $2\,\mathrm{g/cm^3}$. With hydrocarbon chains as main constituent PE materials are thus well suited to be characterised with x-ray computer tomography. Modern tomographs are able to detect density deviations of around 3 $\mathrm{mg/cm^3}$ [69].

Polyethylene pipes show crack initiation under stresses like point load. In order to identify precursors for crack formation not only on nanometre length scales, macroscopic unharmed samples have been scanned via computer tomography as well as a sample with clearly visible crack.

A.1.2. Basic principles

The measured quantity is the space resolved materials absorption coefficient μ. It is represented by the so-called Hounsfield unit (H), also called CT number. The CT number of a material with linear attenuation μ_x is defined as

$$CT_{\text{number}} = 1000 \cdot \frac{\mu_x - \mu_{\text{H}_2\text{0}}^{73\ \text{K}}}{\mu_{\text{H}_2\text{0}}^{73\ \text{K}}}, \tag{A.1}$$

$$= 5263 \cdot \mu_x - 1000. \tag{A.2}$$

Thus for water at 73 K follows a CT number of 0 H, while dense bone leads to a CT number of 3095 H. With $\text{CT}_{number} = -1000$ H the Hounsfield scala includes 4096 values, that can be assigned to each element of the three-dimensional object image.

The measurement of the CT number takes place with an essentially three-component system, consisting of an x-ray source, a varying number of detectors and a computer (see fig. A.1).

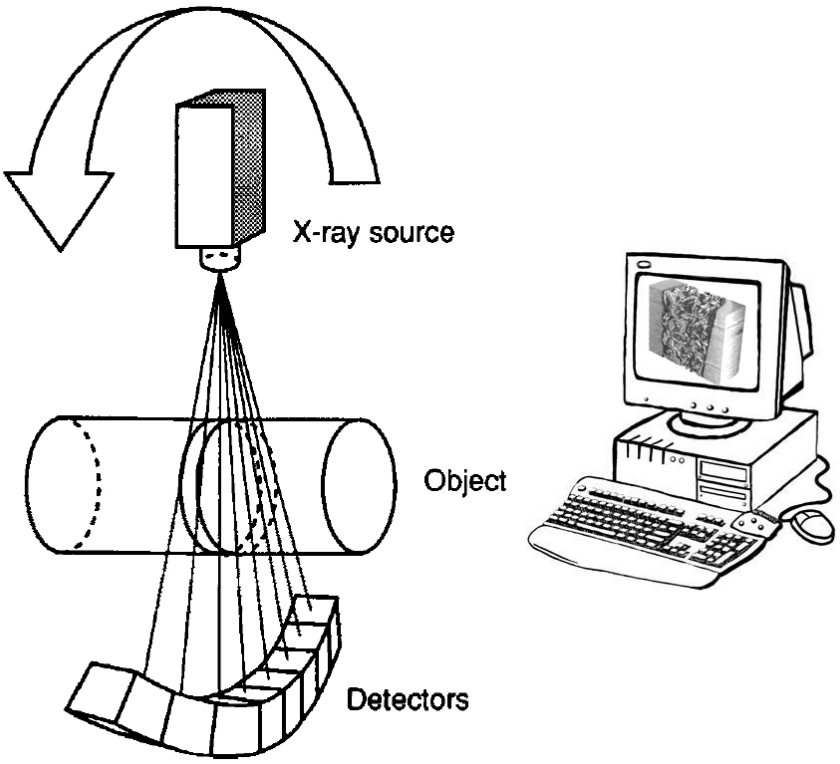

Fig. A.1.: Three component system for x-ray computer tomography. From [40].

While scanning the object, source and detectors circle around the sample. At every position of source and detectors with respect to the object the absorption of the radiation is measured for each volume element in a sample slice. The tomography image is afterwards reconstructed from the intensity measurements. Detailed information concerning the reconstruction algorithms can be found in [26].

The 2D image typically consists of a large number pixels (512×512). The CT number of each pixel represents the absorption of the corresponding volume element, the so-called voxel in the current scanned sample slice.

The spatial resolution of tomography experiments is not within the size of a single pixel, but with 1,5× pixel size a bit above.

A.1.3. Experimental setup at the computer tomograph at Helsinki

The Department of Physics of the University of Helsinki is equipped with an x-ray microtomography laboratory. Samples of up to 20 mm diameter can be scanned with sub-µm resolution. The maximal possible sample diameter is 120 mm. Fig. A.2 shows the tomography setup for the conducted experiments.

On right side the x-ray source can be seen that radiates x-rays with an energy up to 180 keV. In the centre of rotation, ∼2 cm departed from the source, the rod-like sample is introduced into a rotatable sample holder. Another ∼25 cm away the detector system is placed, by which the intensity is measured. A PC is connected to the tomograph for data storage and subsequent calculation and reconstruction of the three-dimensional image of the sample.

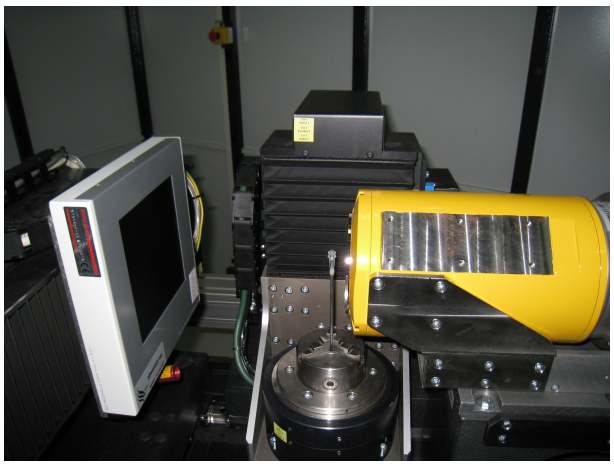

(a)

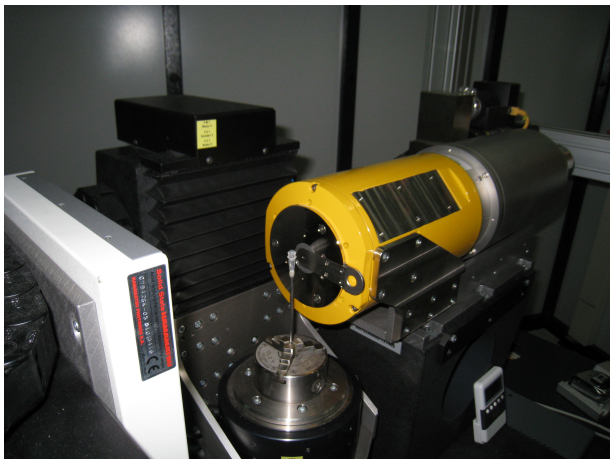

(b)

Fig. A.2.: X-ray tomography setup. The x-ray beam, emanating from the yellow tube on the right hand, hits the sample. The attenuated beam intensity is measured with the two-dimensional detector on the left hand.

A.1.4. Sample preparation and data acquisition

In order to find possible macroscopic cracks in PE samples several samples have been prepared. Corresponding to the required dimensions the rod prepared from a macroscopically unharmed sample had a length of 15 mm and an base area of $2\times2\,\mathrm{mm}^2$. A second sample, prepared from a pipe part with macroscopic crack, was a bit broader (5 mm) in order to stabilise the labile sample slice.

A.1.5. Results

After data acquisition the software calculated the CT number of every voxel in the sample. This procedure took, together with data acquisition, a few hours. The results will be presented in the next two subsection.

Sample with macroscopic crack

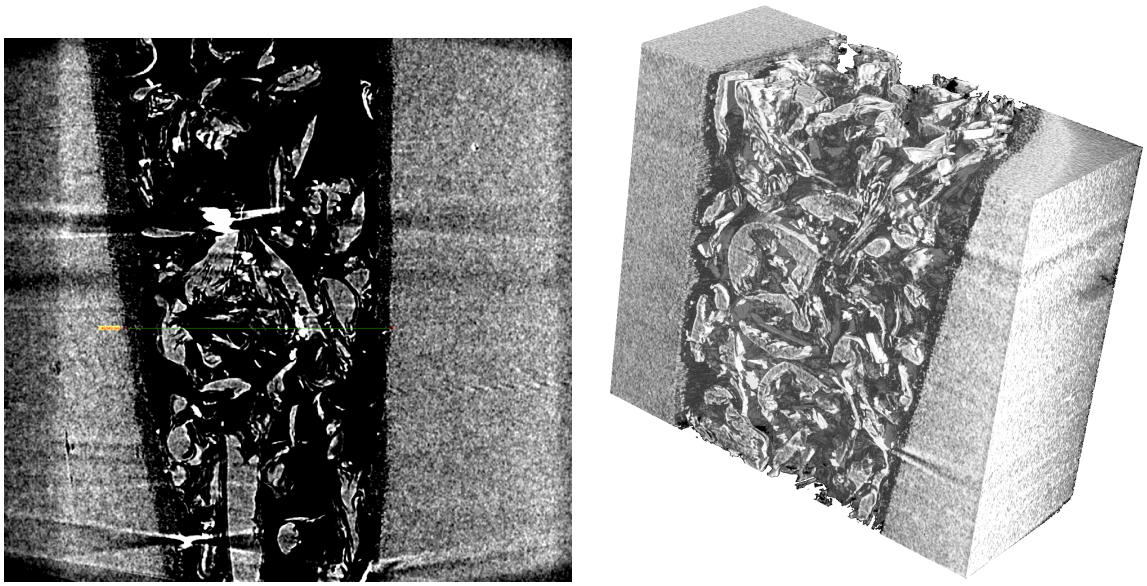

(a) 2D tomography image. (b) 3D tomography image.

Fig. A.3.: Reconstructed tomography images of a PE sample with macroscopic crack. Both images show the splinters resulting from the sample preparation with the help of a saw. In the sample area next to the actual crack no micro cracks are visible.

The reconstruction of the 2D absorption coefficients to a 3D image yielded the three-dimensional structure of the crack sample depicted in fig. A.3. The splinters, originating from the sample preparation, are clearly visible in the image. Besides these damages of the sample structures, no micro cracks can be seen.

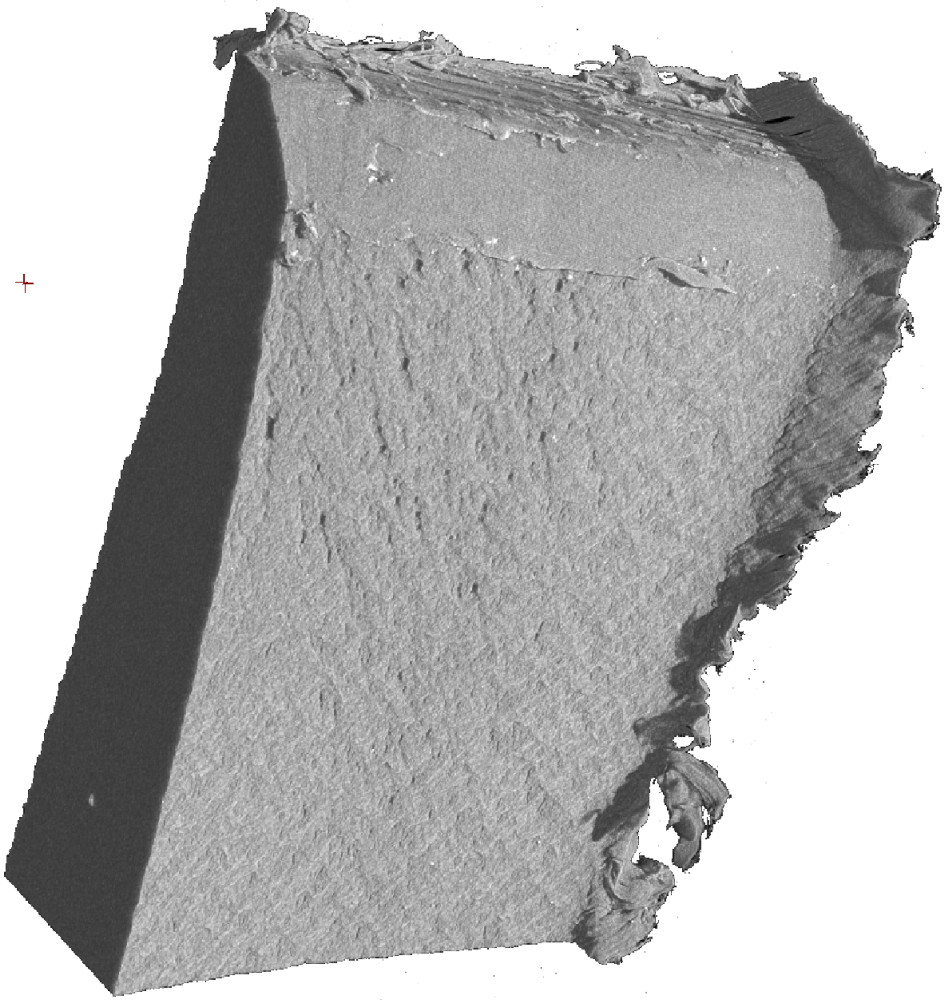

Fig. A.4.: Reconstructed tomography images of a PE sample (bulk slice) without macroscopic crack. The image shows a homogenously density distribution within the entire sample and no indicators for cracks on this length scale.

Intact sample

The reconstructed 3D image of the intact structure is shown in fig. A.4. There are no hints of macroscopic or even microscopic cracks. The entire sample has a homogenous density distribution and shows no precursors of material failure.

A.1.6. Conclusion

X-ray computer tomography experiments have been carried out for a damaged and a macroscopically unharmed sample. Both three-dimensional reconstructed images showed no evidence of micro cracks. Thus it could be concluded that ageing processes take place on smaller length scales.

Bibliography

[1] Website. www.ruppweb.org/Xray/tutorial/spcgrp_tut.htm.

[2] Website. www.aliai.lu/rt/rt19962/rt19962a.htm.

[3] Website. de.wikipedia.org/wiki/Glas.

[4] Website. gertrude-old.case.edu/276/materials/145/14.htm.

[5] Website. www.marresearch.com/products.mar345.html.

[6] Website. hasylab.desy.de/facilities/doris_iii/beamlines/bw5.

[7] Website. www.bruker-axs.de/uploads/tx_linkselectorforpdfpool/HI-STAR_Area_Detector_B86-E00002_03.pdf.

[8] Website. www.esrf.eu/computing/scientific/FIT2D/.

[9] Website. meyweb.physik.uni-giessen.de/1_Lehre/Praktikum/F-Praktikum/VERS13.htm.

[10] Website. www.3d-plastic.eu/shop_3d-plastic/images/PE.pdf.

[11] Website. www.kern-gmbh.de/cgi-bin/riweta.cgi?nr=1411&lng=1&popup=1.

[12] Website. www.ndt.net/article/dgzfp-rt-2007/Inhalt/v02.pdf.

[13] Polymer Physics-Vorlesung, Chapter 7, The University of Suwon. Website.

[14] *Ullmann's Encyclopedia of Industrial Chemistry.* John Wiley & Sons, Inc., 2010.

[15] S. Affolter. *Thermische Einsatzgrenzen von Kunststoffen in Verarbeitung und Anwendung.* Springer VDI Verlag, 2000.

[16] S. Aggarwal und G. Tilley. Determination of Crystallinity in Polyethylene by X-Ray Diffractometer. In *J. Pol. Sci.*, **18**, 1955.

[17] I. Al-Raheil und A. M.Okaz. Chain-Folding in Polyethylene Lamellar Structure. In *Pol. Intern.*, **28**, S. 261–263, 1992.

[18] T. Albrecht und G. Strobl. Temperature-Dependent Crystalline-Amorphous Structures in Linear Polyethylene: Surface Melting and the Thickness of the Amorphous Layers. In *Macromol.*, **28**, S. 5827–5833, 1995.

[19] J. Als-Nielsen und D. McMorrow. *Elements of Modern X-Xay Physics.* John Wiley & Sons, Ltd, 2001.

[20] S. Arrhenius. Über die Reaktionsgeschwindigkeit bei der Inversion von Rohrzucker durch Säuren. In *Zeitschrift für physikalische Chemie*, **4**, S. 226–248, 1989.

[21] N. Ashcroft und D. Mermin. *Solid State Physics.* Holt, Rinehart and Winston, New York, 1976.

[22] H. Beerbaum. *Ermittlung strukturbezogener bruchmechanischer Werkstoffkenn größen an Polyethylen-Werkstoffen.* Dissertation, Martin-Luther-Universität Halle-Wittenberg, 1999.

[23] R. Bonart und R. Hosemann. In *Kolloid Z. Z. Polym.*, **16**, S. 186, 1962.

[24] C. Bunn und T. Alcock. The Texture of Polyethylene. In *Trans. Faraday Soc.*, **41**, S. 317, 1945.

[25] C. W. Bunn. The crystal structure of long-chain normal paraffin hydrocarbons. The "shape" of the <CH2 group. In *Trans. Faraday Soc.*, **35**, S. 482–491, 1939.

[26] T. Buzug. *Einführung in die Computertomographie: Mathematisch-physikalische Grundlagen der Bildrekonstruktion.* Springer-Verlag Berlin Heidelberg, 2004.

[27] R. Caminiti, P. Ballirano, und M. Carbone. Polyethylene Structure as a Function of Temperature: An EDXD Investigation. In *Journal of Macromolecular Science, Part B: Physics*, **45**, 2006.

[28] R. Caminiti, L. Pandolfi, und P. Ballirano. Structure of Polyethylene from X-Ray Powder Diffraction: Influence of the Amorphous Fraction on Data Analysis. In *Journal of Macromolecular Science, Part B*, **39** (4), 2000.

[29] G. Davis, R. Eby, und G. Martin. Variations of the Unit-Cell Dimensions of Polyethylene: Effect of Crystallization Conditions, Annealing, and Deformation. In *J. Appl. Phys.*, **39** (11), S. 4973–4981, 1968.

[30] P. Debye. Zerstreuung von Röntgenstrahlen. In *Ann Physik*, **351** (6), 1915.

[31] H. Dominghaus. *Die Kunststoffe und ihre Eigenschaften.* Springer VDI Verlag, 6. Auflage, 2005.

[32] O. Feroughi. *Temperaturinduzierte Phasenseparation in SiO.* Diplomarbeit, Technische Universität Dortmund University, 2009.

[33] E. Fischer, H. Goddar, und G. Schmidt. Röntgenkleinwinkeluntersuchungen zur Struktur der fehlgeordneten Bereiche in verstrecktem Polyäthylen, Teil II: Messungen an kontrastierten Proben. In *Makromol. Chem.*, **2834** (119), S. 170, 1968.

[34] X. Fu, J. Huang, E. Thian, S. Best, und W. Bonfield. Three-Dimensional Characterization of the Microstructure of Bioglass/Polyethylene Composite by X-Ray Microtomography. In *Key Engineering Materials*, **330-332**, S. 503–506, 2007.

[35] R. Gächter und H. Müller. *Taschenbuch der Kunststoff-Additive.* Hanser Fachbuchverlag, 1990.

[36] U. Gedde und M. Ifwarson. Molecular Structure and Morphology of Crosslinked Polyethylene in an Aged Hot-Water Pipe. In *Polymer Engeneering and Science*, **30** (4), S. 202–210, 1990.

[37] H. Gräfen. *Lexikon Werkstofftechnik*. VDI-Verlag, Düsseldorf, 1991.

[38] D. Grahl. Utilisation of PE pipes in the gas supply. Private communication.

[39] A. Guinier. *X-Ray Diffraction In Crystals, Imperfect Crystals and Amorphous Bodies*. W. H. Freeman and Company, 1963.

[40] S. P. H. Lavebratt, E. Östman und B. Stenberg. Application of Computed X-Ray Tomography Scanning in the Study of Thermo-Oxidative Degradation of Thick-Walled Filled Natural Rubber Vulcanizates. In *Journal of Applied Polymer Science*, **44**, S. 83 – 94, 1992.

[41] J. Hessel. 50 Jahre Rohre aus Polyethylen – Eine ingenieurtechnische Betrachtung. In *3R internat.*, **45** (3,4), S. 128–133, 2006.

[42] D. Holmes und R. Palmer. The orientation of the crystalline and amorphous regions in polyethylene film. In *J. Polym. Sc.*, **31** (123), S. 345–358, 1958.

[43] R. Hosemann und S. Bagchi. *Direct Analysis of Diffraction by Matter*. North-Holland Publishing Co.: Amsterdam, 1962.

[44] T. Huang, H. Toraya, T. Blanton, und Y. Wu. A X-ray powder diffraction analysis of silver behenate, a possible low-angle diffraction standard. In *Journal of Applied Crystallography*, **26** (2), S. 180–184, 1993.

[45] P. van Hutten und A. Pennings. The nature of the lamellar overgrowth in polyethylene shish-kebab fibres as revealed by small angle x-ray scattering and electron microscopy. In *J. Mat. Sc.*, **17**, S. 3525–3540, 1982.

[46] J. Jackson. *Classical Electrodynamics*. John Wiley & Sons, 1999.

[47] R. James. *The Optical Principles of the Diffraction of X-Rays*. Cornell University Press, Ithaca, New York, 1965.

[48] K. Jansen. *Säureeinfluss auf die photochemische Alterung von UV-stabilisierten Polyethylenfolien*. Dissertation, Freie Universität Berlin, 2003.

[49] M. Kakudo und R. Ullmann. Polyethylene Crystallinity from X-Ray Studies. In *J. Pol. Sci.*, **65**, 1960.

[50] G. Kerch und L. Irgen. Thermal Expansion of Oriented Polyethylene. In *Mechanics of Composite Materials*, **11** (3), S. 468–470, 1975.

[51] C. Kittel. *Introduction to Solid State Physics*. John Wiley & Sons, Ltd, 1976.

[52] H. Klug und L. Alexander. *X-Ray Diffraction Procedures*. John Wiley & Sons Inc., New York, 1959.

[53] H. Klug und L. Alexander. *X-Ray Diffraction Procedures*. John Wiley & Sons Inc., New York, 1959.

[54] M. Krämer. *Struktur und Dynamik von Gold-Clustern auf dünnen Polymer-Filmen: Untersuchungen mit kohärenter Röntgenstrahlung*. Diplomarbeit, Technische Universität Dortmund University, 2003.

[55] E. Krenzer und W. Ruland. Temperature dependence of lattice distortions in polyethylene. In *Colloid & Polymer Sci.*, **259**, 1981.

[56] S. Krimm. X-Ray Studies of Crystalline and Amorphous Order in High Polymers. Band 57, S. 22–25. 26th National Colloid Symposium, 1953.

[57] C. Krywka. *Ein Aufbau für Röntgenkleinwinkelstreuung an Protein-Lösungen an der Synchrotronstrahlungsquelle DELTA*. Dissertation, Technische Universität Dortmund University, 2008.

[58] C. Krywka, M. Paulus, C. Sternemann, M. Volmer, A. Remhof, G. Nowak, A. Nefedov, B. Pöter, M. Spiegel, und M. Tolan. The new diffractometer for surface x-ray diffraction at beamline BL9 of DELTA. In *J. Synchrotron Rad.*, **13**, S. 8, 2006.

[59] C. Krywka, C. Sternemann, M. Paulus, N. Javid, R. Winter, A. Al-Sawalmih, S. Yi, D. Raabe, und M. Tolan. The small-angle and wide-angle X-ray scattering set-up at beamline BL9 of DELTA. In *J. Synchrotron Rad.*, **14**, S. 244, 2007.

[60] C. Krywka, C. Sternemann, M. Paulus, M. Tolan, C. Royer, , und R. Winter. Effect of osmolytes on pressure-induced unfolding of proteins: A high-pressure SAXS study. In *Chem. Phys. Chem.*, **9**, S. 2809, 2008.

[61] L. Larrondo und R. S. J. Manley. Electrostatic fiber spinning from polymer melts. I. Experimental observations on fiber formation and properties. In *J. Polym. Sci. Polym. Phys. Ed.*, **19** (6), S. 909–920, 1981.

[62] N. Lelli, A. Landuzzi, und K. Tan. Breakthrough stabilization and 'functionalization' solutions for polyolefin films. In *Int Symp Weather*, **4**, S. 58–69, 2000.

[63] P. Lindenmeyer und S. Lustig. Crystallite Orientation in Extruded Polyethylene Film. In *J. Appl. Polym. Sc.*, **9** (1), S. 227–240, 1965.

[64] G. Menges, H. Haberstroh, W. Michaeli, und E. Schmachtenberg. *Werkstoffkunde Kunststoffe*. Carl Hanser Verlag München, Wien, 5 Auflage, 2002.

[65] J. Otegui, J. Vega, S. Martin, V. Cruz, A. Flores, C. Domingo, und J. Marinez-Salazar. The unit cell expansion of branched polyethylene as detected by Raman spectroscopy: an experimental and simulation approach. In *J. Mater. Sci.*, **45**, 2007.

[66] S. Ottani, E. Ferracini, A. Ferrero, V. Malta, und R. Porter. SAXS Investigations on Uniaxially Drawn Fibers Obtained from Polyethylene Reactor Powder. In *Macromolecules*, **29**, S. 3292, 1996.

[67] A. Pennings, J. M. A. A. van der Mark, und A. M. Kiel. Hydrodynamically induced crystallization of polymers from solution, III. Morphology. In *Kolloid Z. Z. Polym.*, **237** (2), S. 336–358, 1982.

[68] N. Peppas, A. Argade, und S. Bhargava. Preparation and properties of poly(ethylene oxide) star polymers. In *J. Appl. Pol. Sc.*, **87** (2), S. 322–327, 2003.

[69] S. Persson. How computed X-ray tomography can be used to study crosslink density in non-filled peroxide cured polyisoprene rubber. In *Polymer*, **29** (5), S. 802 – 807, 1988.

[70] A. Peterlin. Drawing and extrusion of semi-crystalline polymers. In *Colloid & Polymer Science*, **265**, S. 357, 1987.

[71] J. Rabek. *Photodegradation of Polymers.* Springer Verlag, 1996.

[72] S. Rabiej und A. Wlochowicz. SAXS and WAXS Investigations of the Crystallinity in Polymers. In *Die Angewandte Makromolekulare Chemie*, **175** (2920), S. 81–97, 1990.

[73] K. Richard und G. Diedrich. Rohre aus Niederdruckpolyäthylen – Eigenschaften und Erprobung in Labor und Praxis. In *Kunststoffe*, **45** (2), S. 183–190, 1956.

[74] P. Rizzo, F. Baione, G. Guerra, L. Martinotto, und E. Albizzati. Polyethylene Unit Cell and Crystallinity Variations as a Consequence of Different Cross-Linking Processes. In *Macromol.*, **34**, 2001.

[75] S. Sasaki, H. Masunaga, H. Tajiri, K. Inoue, H. Okuda, H. Noma, K. Honda, A. Takahara, und M. Takata. In situ investigations of annealing effect on lamellar stacking structure of polyethylene thin films by synchrotron gracing-incidence small-angle and wide-angle X-ray scattering. In *J. Appl. Cryst.*, **40**, S. 642–644, 2007.

[76] K. Schauer und W. Wilke. Wide-angle X-ray scattering studies on polyethylene at low temperatures. In *Polymer Bulletin*, **34**, S. 477–483, 1995.

[77] M. Schroer. *Röntgenkleinwinkelstreuung an dem Protein Staphylokokken Nuklease und dessen Mutanten.* Diplomarbeit, Technische Universität Dortmund University, 2008.

[78] U. Schulte und J. Hessel. Remaining service life of plastic pipes after 41 years in service. In *3R internat.*, **9**, S. 1–5, 2006.

[79] N. Severin. *Molecular Dynamics Simulations of Polymers and Micelles at Interfaces.* Dissertation, Humboldt-Universität zu Berlin, 1999.

[80] D. Snetivy, H. Yang, und G. Vansco. Imaging of Different Crystal Planes in Oriented Polyethylene by Atomic Force Microscopy. In *J. Mater. Chem.*, **2** (8), S. 981–952, 1992.

[81] M. Stranz. On the extrusion of PE pipes. Private communication.

[82] G. Strobl. *The Physics of Polymers*. Springer, 2007.

[83] P. Swan. Polyethylene Unit Cell Variations with Temperature. In *J. Polym. Sc.*, **56**, S. 403–407, 1962.

[84] K. Tashiro, I. Tanaka, T. Oohara, N. Niimura, S. Fujiwara, und T. Kamae. Extraction of Hydrogen-Atom Positions in Polyethylene Crystal Lattice from Wide-Angle Neutron Diffraction Data Collected by a Two-Dimensional Imaging Plate System: Comparison with the X-ray and Electron Diffraction Results. In *Macromolecules*, **37** (11), S. 4109–4117, 2004.

[85] N. Taylor, G. F. Fanta, W. M. Doane, und C. R. Russell. Swelling and rheology of saponified starch-*g*-polyacrylonitrile copolymers. Effect of starch granule pretreatment and grafted chain length. In *J. Appl. Pol. Sc.*, **22** (5), S. 1343–1357, 1978.

[86] M. Tolan. *X-Ray Scattering from Soft-Matter Thin Films*. Springer-Verlag Berlin Heidelberg New York, 1999.

[87] R. Tudesco. Thermische Einsatzgrenzen von Kunststoffen in Verarbeitung und Anwendung. Springer VDI Verlag, 2000.

[88] K. Ueno, K. Seki, K. Sugita, und H. Inokuchi. Nature of temperature dependence of conduction bands in polyethylene. In *Phys. Rev. B*, **43** (3), S. 2384–2390, 1991.

[89] A. Vaughan und D. Bassett. *Comphrehensive Polymer Science*, Band 2. Pergamon Press, 1989.

[90] C. Vonk und A. Pijpers. An X-Ray Diffraction Study of Nonlinear Polyethylene. I. Room-Temperature Observations. In *J. Pol. Sc.: Pol. Phys. Ed.*, **23**, S. 2517–2537, 1985.

[91] E. Walenta, A. Janke, D. Hofmann, D. Fanter, und D. Geiss. Zur übermolekularen Struktur von Blasfolien aus Polyethylen niederer Dichte. In *Acta Polymerica*, **37** (9), S. 357, 1986.

[92] R. Weiss und C. Desper. Structure of polyethylene. In *Phylosophical Magazine*, **30** (2), 1974.

[93] R. Wycoff. *Crystal Structures*. New York, London, Sydney: Interscience Publishers, 1963.

[94] K. Ziegler, E. Holzkamp, H. Breil, und H. Martin. Das Mülheimer Normaldruck-Polyäthylen-Verfahren. In *Ang. Ch.*, **19/20**, S. 541–636, 1955.

Danksagung

Viele Menschen haben zum Gelingen meiner Doktorarbeit beigetragen. Diesen Menschen und allen, die ich sträflicherweise in dieser Aufzählung vergessen sollte, möchte ich herzlich dafür danken.

Zu allererst möchte ich Herrn Prof. Dr. Metin Tolan für die Möglichkeit danken, auch meine Dissertation in seiner Arbeitsgruppe anfertigen zu dürfen. Vielen Dank auch für das interessante Thema, das weitreichender war als von uns beiden zunächst angenommen.

RWE danke ich für die Finanzierung meiner Arbeit und Herrn Dirk Grahl für die wertvollen Informationen über Rohre und Alterung.

Herrn Dr. Peter Funke danke ich für die Vermittlung dieser Kooperation.

Weiterhin möchte ich insbesondere meinen beiden Betreuern Dr. Christian Sternemann und Dr. Michael Paulus für die exzellente Betreuung nicht nur während der Promotionszeit, sondern insbesondere in der letzten Phase des Zusammenschreibens, für die umfangreichen Diskussionen und das Korrekturlesen danken. Die Messzeiten bei DELTA hätten ohne Eure Betreuung der Beamline und das Übernehmen von Schichten auch nie so reibungslos funktioniert.

Dem gesamten Lehrstuhl E1a gilt mein Dank für die freundliche Atmosphäre und das produktive Arbeitsklima. Vielen Dank für die vielen Diskussionen, die nicht nur meine Arbeit bereichert haben. Insbesondere bei meinen „Zellengenossen" Omid Feroughi, Lars Böwer und Steffen Bieder möchte ich für das stressfreie „Zusammenleben", viele Diskussionen über alles Mögliche, Dart-Duelle auf hohem Niveau und die Unterstützung bei Messzeiten danken. Steffen und seiner Freundin danke ich ebenso für's Korrekturlesen. Allen anderen, die mehr als nur einen kurzen Blick auf einzelne Kapitel und die Auswertung geworfen haben, gilt ebenso mein Dank.

Den DELTAnern möchte ich für die freundliche Beherbergung während der vergangenen fünfeinhalb Jahre danken und natürlich auch dafür, daß sie überhaupt Licht in die Hütte gebracht haben. Gerrit Schünemann gilt sicher nicht nur mein Dank für die Einrichtung der Grundversorgung. Mancher Tag wäre ohne den Kiosk noch hungriger zu Ende gegangen.

Dirk Schemionek vom Präplab und Peter Kortmann sowie Thomas Dybiona für die Unterstützung bei den ausführlichen Schnitzereien meiner Proben wie auch Wolfgang Brembt beim mehr als kurzfristigen Basteln meines Steckers an der Heizzelle möchte ich ebenfalls danken.

Prof. Dr. Ritva Serimaa, Kira Pirkkalainen und allen anderen Mitgliedern von Prof. Serimaas Lehrstuhl danke ich nicht nur für die Unterstützung während meiner Messzeit in Finnland, sondern ebenfalls für die fruchtbare Diskussion meiner Daten danach. Martin von Zimmermann möchte ich für die Betreuung während meiner Messzeit am Hasylab danken.

Bei den Mitarbeitern Andreas Regeling, Dr. Michael Stranz und Mario Paaßen der Firma egeplast möchte ich mich für die Werksführung und die vielen Informationen geben, die sie mir auch im Nachgang noch zur Verfügung gestellt haben. Vielen Dank auch für die geduldige Beantwortung meiner Fragen.

Robert Fendt danke ich für die fortwährende Unterstützung nicht nur in technischen Fragen (Matlab und LaTeXsind mehr als doof), sondern auch in moralischer Sicht. Zudem warst Du mir beim finalen Korrigieren meiner Arbeit mehr als einmal behilflich.

Meiner Freundin Jessica Bubenzer möchte ich dafür danken, daßsie es trotz vieler privater und beruflicher Verpflichtungen auf sich genommen hat, sich erneut durch meine Schreiberei zu quälen.

Meiner Handballmannschaft und dem damit verbundenen Training beim TuS 03 Hagen wie auch meiner Tanzgruppe bei der Sportunion Annen möchte ich danken für die mehr als nötige Ablenkung für Körper und Geist, die mich nicht nur in letzter Zeit vor dem Durchdrehen bewahrt haben.

Der konaktiva Dortmund und seinem Team möchte ich für die wunderbare Möglichkeit danken, mich nicht nur bei der Organisation der Messe einzubringen, sondern neben

dem Erlernen nützlicher Fähigkeiten auch tolle Menschen mit viel Engagement kennen zu lernen. Danke für die tolle Zeit!

Daniela Lietz möchte ich für die fortwährende Unterstützung und Freundschaft danken. Vieles wäre ohne Dich nicht möglich gewesen.

Jetzt kann ich fast nur noch meiner Familie danken. Ohne Euch und Eure Unterstützung wären mein gesamtes Studium und letztlich auch meine Doktorarbeit nicht möglich gewesen. Ihr wart immer für mich da und gebt mir auch immer noch Obdach und ein warmes Essen, wann immer ich bei Euch auftauche. Danke.

Zuguterletzt möchte ich mich bei meinem Freund Benjamin bedanken. Dank Dir und Deiner Unterstützung konnte ich nicht nur die letzten Monate überstehen, sondern Du hast mich immer wieder aufgebaut, wenn mal wieder eine Krise anstand. Danke ist dafür eigentlich ein zu schwaches Wort.

Eidesstattliche Erklärung

Hiermit erkläre ich an Eides Statt, dass die vorliegende Dissertation – abgesehen von der Beratung durch meine wissenschaftlichen Lehrer – nach Inhalt und Form meine eigene Arbeit ist. Sie wurde weder ganz noch in Teilen an anderer Stelle im Rahmen eines Prüfungsverfahrens vorgelegt.
Dortmund, den 28. November 2010

(Saskia Schmacke)